OXYGEN DIFFUSION STUDIES IN MIXED IONIC ELECTRONIC CONDUCTING COMPOUNDS

A Dissertation

Presented to

the Faculty of the Department of Chemistry

University of Houston

In Partial Fulfillment

of the Requirements for the Degree

Doctor of Philosophy

By

Dmitry Rupasov

August 2014

OXYGEN DIFFUSION STUDIES IN MIXED IONIC ELECTRONIC CONDUCTING COMPOUNDS

_____

Dmitry Rupasov

APPROVED:

_____

Dr. Allan J. Jacobson, Chairman

_____

Dr. Arnold M. Guloy

_____

Dr. Steven Baldelli

_____

Dr. Haleh Ardebili

_____

Dr. James K. Meen

_____

Dean, College of Natural Sciences and Mathematics

Dedicated to the loving memory of my mother

Acknowledgements

Firstly, I would like to express the deepest appreciation to my research advisor Dr. Allan J. Jacobson for his help and guidance, and most importantly, support during my PhD research. I would also like to thank all members of Dr. Jacobson's group; in particular, Tatyana Makarenko for her generous assistance with TGA and dilatometry measurements, Dr. Boris Makarenko for help with SIMS experiments, Ellen Lee for her continuous care and support, and my labmates Julie, Sam, Bee, Marlon and Sang Ho for friendly environment and healthy sense of humor.

I am very much grateful to Dr. John A. Kilner for accepting me as a visitor student at Imperial College London. While being a member of the Fuel Cells group I met a lot of support with my experiments from all members of the group. Particularly, I would like to thank Dr. Andrey Berenov for his invaluable help and patience with IEDP/SIMS and AC Impedance experiments, Dr. Alexander Chroneos and Dr. David Parfitt for inviting me to the world of molecular dynamics.

I would like to give my thanks to my colleagues from Moscow State University; particularly, to Dr. Evgeny V. Antipov and Dr. Sergey Ya. Istomin for guidance and general discussion, and to my friend Dr. Oleg A. Drozhzhin for helpful comments and support in and outside of research field.

I would like to thank my teachers for the knowledge, which they generously shared with me, and the members of my committee for their valuable comments and feedback on my work.

I gratefully appreciate the support shown by all members of my family. I thankful to my parents, Pavel and Alevtina, for their love, encouragement and care throughout my life.

Finally, and most importantly, I endlessly thankful to my wonderful wife, Guzel, for her unconditional love to me and strong belief in my ability to succeed. Her support helped me to overcome all difficulties in my research work. I also thank our son, Tim, for showing me how joyful can be curiosity.

OXYGEN DIFFUSION STUDIES IN MIXED IONIC ELECTRONIC CONDUCTING COMPOUNDS

An Abstract of a Dissertation

Presented to

the Faculty of the Department of Chemistry

University of Houston

In Partial Fulfillment

of the Requirements for the Degree

Doctor of Philosophy

By

Dmitry Rupasov

August 2014

Abstract

Cobalt-based oxides with perovskite-related structures are important candidate cathode materials for the next generation solid oxide fuel cells (SOFCs) because of their good catalytic properties and high values of electronic and ionic conductivity. The aim of the work described in the thesis is to investigate oxygen transport in $Sr_3YCo_4O_{10.5}$ (SYC, the so-called 314 phase) and double perovskites $LnBaCoFeO_{5+\delta}$ (Ln = La, Pr, Sm and Gd) with combination of theoretical and experimental methods.

The oxygen transport properties of $Sr_3YCo_4O_{10.5}$ were studied by three different techniques. Molecular dynamics simulations (MD) predicted an isotropic character of oxygen diffusion with an activation energy of 1.56 eV in the temperature range of 1000 – 1400 K. Values of tracer oxygen diffusion, D^*, and the surface exchange coefficient, k^*, were measured as a function of temperature (500 – 900 °C) with isotope exchange depth profiling combined with secondary ion mass spectrometry (IEDP/SIMS). Chemical oxygen diffusion coefficients, D_{chem}, and chemical surface exchange rates, k_{chem}, were obtained from electrical conductivity relaxation experiments (ECR). Good agreement of the results obtained by different techniques was confirmed after application of thermodynamic factors to the ECR data. Electrochemical performance of symmetrical cells with $Ce_{0.9}Gd_{0.1}O_{1.95}$ (GDC) as electrolyte (SYC/GDC/SYC) in the temperature range 620 – 770 °C was evaluated.

Double perovskites $LnBaCoFeO_{5+\delta}$ (Ln = La, Pr, Sm and Gd) were studied by combination of ECR, thermogravimetric analysis (TGA) and dilatometry. It was found that size of rare earth element (REE) has strong influence on electrochemical and mechanical

properties of the samples. In case of La and Pr-containing compounds, fast degradation of the surface kinetics during ECR experiments at high oxygen partial pressure was associated with surface segregation. ECR measurements at low pO_2 switches were performed for La, Pr and Gd-containing samples to avoid large deviation from chemical equilibrium during experiments. For $SmBaCoFeO_{5+\delta}$ it was found that a linear model for the exchange kinetics works in a larger $pO_2^{(1)}/pO_2^{(2)}$ interval.

The effect of A-cation ordering in $LaBaCoFeO_{5+\delta}$ on oxygen transport properties was investigated. Oxygen diffusion was found to be slower in ordered structure, due to the influence of ordering in A-cation sublattice on anion ordering.

Table of contents

List of figures

List of tables

List of symbols and abbreviations

ALS	Adler-Lane-Steele
ASR	Area specific resistance
CIP	Cold isostatic press
ECR	Electrical conductivity relaxation
EIS	Electrochemical impedance spectroscopy
FIB	Focused ion beam
GDC	Gadolinium-doped ceria
IEDP	Isotope exchange depth profiling
IT-SOFC	Intermediate temperature solid oxide fuel cell
MD	Molecular dynamics
MIEC	Mixed electronic and ionic conductor
OPM	Oxygen permeable membrane
REE	Rare earth element
SEM	Scanning electron microscopy
SIMS	Secondary ion mass spectrometry
SOFC	Solid oxide fuel cell
TEC	Thermal expansion coefficient
TGA	Thermogravimetric analysis
UHV-SIMS	Ultra high vacuum SIMS
XRD	X-ray diffraction

SYC	$Sr_3YCo_4O_{10.5}$
YSZ	Yttria stabilized zirconia
α	Thermal expansion coefficient
α_m	The positive root of the transcendental equation $\alpha_m tan\alpha_m = C$
A	The surface are of the sample
a_i	Activity of species i
A_{ij}, ρ_{ij}, C_{ij}	Parameters of interionic interaction
C	$\frac{l}{l_d}$, a measure of importance of the surface exchange reaction contribution
c_i	Concentration of species i
D_a	The ambipolar diffusion coefficient
$\widetilde{D}_i$, D_{chem}	Chemical diffusion coefficient of species i
D_i^*	Tracer diffusion coefficient of species i
D_i	Self-diffusion coefficient of species i
e'	Electron
E_L	Ionic crystal lattice energy
E_A	Activation energy
erfc	Complementary error function
f	The Haven ratio
F	The Faraday constant
g(t)	The relative conductivity in ECR experiment

Γ_i	Thermodynamic factor of species *i*
h	$\frac{k^*}{D^*}$
$h^{\cdot}$	Electron hole
j_i	Flux of species *i*
k^Q	The empirical surface exchange coefficient in electrical experiments
k^*	The empirical surface exchange coefficient in isotope exchange experiments
k_{chem}	The chemical surface exchange coefficient
l	Half thickness
l_d	The characteristic length
m_O	Atomic mass of oxygen
μ_i	Chemical potential of species *i*
$\tilde{\mu}_i$	Electrochemical potential of species *i*
N_a	Avogadro's number
${}^iO$	Oxygen isotope (*i* = 16, 18)
P_{O_2}	The oxygen partial pressure
$P_{O_2}^{(1)}$	The initial oxygen partial pressure
$P_{O_2}^{(2)}$	The final oxygen partial pressure
R	The gas constant
R_{chem}	Characteristic resistance
R_i	Any process that leads to the formation or removal of species *i*

r_i	Ionic radius of ion *i*
r_{ij}	Interionic distance
σ_i	Conductivity of species *i*
t	Goldschmidt tolerance factor
t_{chem}	Characteristic time constant
t_i	Transport number of species *i*
u_i	Mean drift velocity per unit field of species *i*
V_m	Molar volume
$V_O^{\cdot\cdot}$	Oxygen vacancy
ω	Frequency of AC signal
x	Distance
x_n	Electronegativity of atom *n*
z_i	Charge of species *i*

Chapter 1. Introduction

1.1. Objective

The objective of this research is to investigate oxygen diffusion properties in mixed ionic-electronic compounds (MIEC) by different methods: electrical conductivity relaxation (ECR), isotope exchange depth profiling (IEDP) and molecular dynamic simulations (MD). It includes:

1. Study of oxygen diffusion transport in the perovskite-related compound $Sr_3YCo_4O_{10.5}$ with ECR, IEDP and MD and a comparison of the results.
2. ECR study of double perovskites $LnBaCoFeO_{5+\delta}$ (Ln = La, Pr, Gd and Sm).
3. Determination of the thermal expansion coefficients (TEC) by dilatometry.

1.2. Scope of the thesis

Chapter 1 focuses on the general background for oxygen transport in mixed ionic-electronic compounds. The application of MIEC oxides, diffusional transport, surface exchange reactions and defect chemistry are described in brief. The principles of the oxygen diffusion process described using a binary compound as an example.

Chapter 2 summarizes the theoretical background and analysis of the electrical conductivity relaxation (ECR) and isotope exchange depth profiling (IEDP) experiments with a linear surface exchange model. Sample requirements for ECR and IEDP experiments are discussed.

Chapter 3 describes the investigation of the oxygen diffusion in the perovskite-related compound $Sr_3YCo_4O_{10.5}$ with two *ex situ* methods (ECR and IEDP) and with one

computational method (MD). Determination of the thermodynamic factor, which represents the dependence of the oxygen content of the compound on the oxygen partial pressure in the surroundings and temperature by thermogravimetric analysis (TGA) and iodometric titration is included. Oxygen diffusion coefficients obtained by all three methods are compared. Electrochemical performance of symmetrical cells $Sr_3YCo_4O_{10.5}$ / $Ce_{0.9}Gd_{0.1}O_{1.95}$ / $Sr_3YCo_4O_{10.5}$ is investigated by AC Impedance spectroscopy.

In Chapter 4, an ECR study of double perovskites $LnBaCoFeO_{5+\delta}$ (Ln = La, Pr, Gd and Sm) is described. Thermodynamic factors for all four compounds were determined by thermogravimetric analysis (TGA). Syntheses and characterization of $LaBaCoFeO_{5+\delta}$, compounds crystalizing in cubic and tetragonal space groups, are described. The dependence of oxygen diffusion coefficients and surface exchange rates on crystal structure and ionic size of the rare earth element (REE) is studied.

Chapter 5 is focused on investigation of thermal expansion of perovskite-related compound $Sr_3YCo_4O_{10.5}$ and double perovskites $LnBaCoFeO_{5+\delta}$ (Ln = La, Pr, Gd and Sm). The behavior of the thermal expansion coefficients (TECs) is discussed.

1.3. Background

Mixed ionic-electronic compounds with perovskite structure (ABO_3), such as acceptor-doped systems $LaCoO_3$ and $LaFeO_3$ [1], are of great interest due to the possibility of their use in applications that require separation of oxygen from air or other oxygen-containing gas mixtures in variety of devices: oxygen separation membranes, electrodes of solid oxide fuel cells (SOFCs) and catalytic reactors [2-4].

The present research is focused on further understanding and determination of oxygen transport properties in these oxides.

In recent years, techniques such as isotope exchange depth profiling combined with secondary ion mass spectrometry (IEDP/SIMS) [5-6], oxygen permeation experiments [7-12], mass or electrical relaxation experiments and AC Impedance spectroscopy [13] have been used to study the fundamentals of the oxygen transport properties in variety of different perovskite and perovskite-related mixed ionic-electronic oxides. In particular, bulk diffusion coefficients and surface exchange rates have been investigated using these techniques, and relationship between materials properties and performance has been studied. In this work, three of these techniques, isotope exchange depth profiling combined with secondary ion mass spectrometry, electrical conductivity relaxation and molecular dynamic simulations have been used to study several MIEC oxides. The techniques will be described in details in following chapters. Here, the general background for oxygen transport in MIEC oxides will be introduced. The defect chemistry, surface exchange reactions and diffusional transport concepts in MIEC will be described.

1.4. Defect chemistry

Perovskites are a large group of compounds with closely related crystal structures, which have taken their name from the natural mineral $CaTiO_3$. The general formula is ABX_3, in which A and B are cations, and X is usually oxygen or fluorine. The oxide perovskites (ABO_3) have a wide variety of electrical and magnetic properties, which make them interesting for different applications such as reforming of natural gas, solid oxide fuel cells (SOFCs), oxygen permeable membranes (OPM), oxidation catalysis, oxygen sensors

and others.

The point defect chemistry of ABO_3 perovskites explains the origins of the ionic and electronic conductivities, which, generally, are independent in crystalline materials [14]. The ionic one is mainly related to the crystal structure, which should provide a continuous pathway for ions movement, while the electronic conductivity is determined by the electronic bandgap, and depends more on the individual properties of the ions in the compound.

The ideal perovskite structure can be described as consisting of corner-sharing BO_6 octahedra with the large A-cation occupying the body center, 12-coordinated by oxygen atoms position. The cubic perovskite structure is illustrated in Figure 1.1.

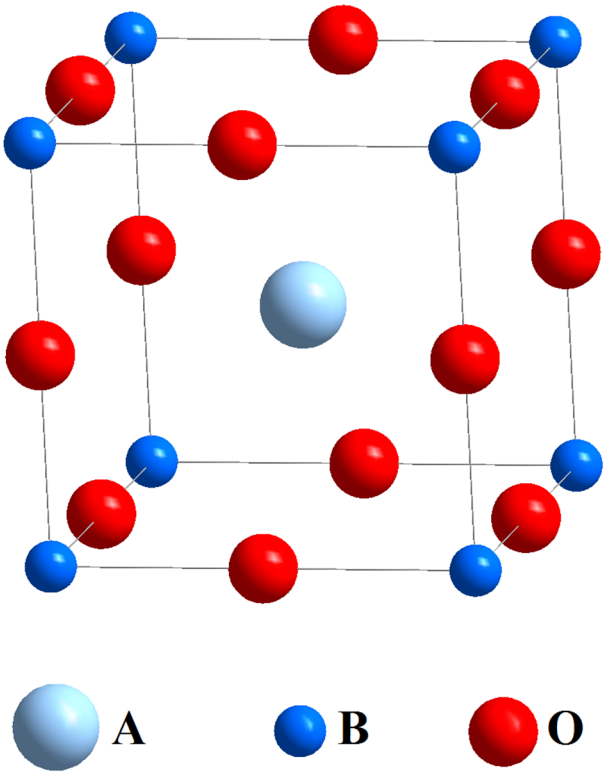

Figure 1.1. Ideal perovskite structure.

Rotation or tilting of the BO_6 octahedra, or displacement of the cations, will give rise to a lower symmetry typically corresponding to tetragonal, orthorhombic or rhombohedral structures. The unit cell volume will also increase. The possibility for a ternary oxide to crystallize in the perovskite structure can be predicted using the Goldschmidt tolerance factor (*t*) [15]

$$t = \frac{r_A + r_O}{\sqrt{2}(r_B + r_O)} \qquad \text{(Equation 1.1)}$$

where r_i denotes the ionic radius of the given ion.

Geometrically, values of tolerance factor close to one ($t = 1$) is required for an ideal cubic perovskite structure, comprising only a few oxides. For *t* slightly less than 1, the BO_6 octahedra is rotated about the (111) axis, giving rise to a rhombohedral unit cell. For smaller *t*, the octahedra tilt about (001) and (110), resulting in the orthorhombic structure [16]. Generally, the ABO_3 perovskite structure is stable between $0.75 < t < 1.06$ [17]. For the other values of *t*, formation of nonperovskite structures will be favorable. Due to the fact that a wide range of tolerance factor allows formation of perovskite structures, a significant fraction of dopant, usually a divalent cation (D), can be introduced into the A site. That leads to another important parameter for the crystal symmetry – nonstoichiometry arising from cation deficiency or oxygen deficiency. Oxygen deficiency will lead to formation of oxygen vacancies ($V_O^{\cdot\cdot}$) in the structure, that are effectively positive with respect to the lattice. Cation deficiency may occur, for example, when the B cation is a multivalent transition metal, and may lead to the formation of electronic defects, such as electron holes. The electron holes can be trapped at the cation or can migrate freely through the structure. These two kinds of defects are the basis for ionic, $V_O^{\cdot\cdot}$, and electronic, $h^{\cdot}$,

conductivities.

Considering partial substitution of La in $LaFeO_3$ by Sr, the charge neutrality criteria can be expressed by Kröger-Vink notation as

$$[e'] + [Sr'_{La}] = 2[V_O^{\cdot\cdot}] + [h^{\cdot}] \qquad \text{(Equation 1.2)}$$

where the electron, e', comes from the disproportionation of the Fe cations,

$$2Fe_{Fe}^{\times} = Fe_{Fe}^{\cdot} + Fe'_{Fe} \qquad \text{(Equation 1.3)}$$

By Kröger-Vink notation, M_S^C means species M, that can be atom, vacancy, interstitial, electron or electron hole, located at S lattice site with the C electronic charge. One positive excess charge is indicated by a dot ($\cdot$), one negative excess charge is by a prime ($'$), and neutral is by a cross ($\times$).

The electron holes ($h^{\cdot}$) can be formed by acceptor doping and disproportionation reaction. Electronic conductivity is usually explained by a polaron mechanism with a thermally activated mobility [18]. The hopping mechanism can be written schematically [19]:

$$B^{n+} - O^{2-} - B^{(n-1)+} \rightarrow B^{(n-1)+} - O^{-} - B^{(n-1)+} \rightarrow B^{(n-1)+} - O^{2-} - B^{n+}$$

The hopping is possible due to the overlap between the filled 2p orbitals of oxygen and neighboring empty or partially filled d-orbitals of the transition metal B.

In materials for oxygen delivery application, the electronic component of conductivity is usually predominant [20], and the oxygen ion conductivity is usually comparable to that of the well-known ionic conductors, such as yttria stabilized zirconia (YSZ) and gadolinium-doped ceria (GDC).

1.5. Oxygen transport in mixed ionic and electronic oxides

The process of oxygen transport in mixed ionic and electronic oxides occurs in two steps: diffusion of oxygen atoms in the bulk of the material and surface exchange at the surface of the material between oxygen atoms in the surrounding gas and in the solid.

1.5.1. Bulk oxygen diffusion

In this chapter the concept of oxygen diffusion is briefly explained, starting with the diffusion of a single type of charge carrier and moving to consideration of multiple types of charge carriers. Chemical diffusion in a binary oxide is also discussed. Charge carriers are considered as disordered at isothermal conditions and rapid surface exchange is assumed.

1.5.1.1. Fickian transport and diffusion coefficients

Diffusion is the process of concentration equilibration in non-equilibrium system. According to Fick's first law [21], the flux j_i, considered as the flow of species i per unit area perpendicular to the flow and per unit time, is proportional to the gradient of its concentration, c_i,

$$j_i = -D_i \frac{\partial c_i}{\partial x} \qquad \text{(Equation 1.4)}$$

where D_i is the self-diffusion coefficient and c_i is the concentration of species i in the compound. For simplification, a one-dimensional case and an isotropic material are considered. Conserved mass in the system can be expressed as

$$\frac{\partial c_i}{\partial t} = -\frac{\partial j_i}{\partial x} + R_i \qquad \text{(Equation 1.5)}$$

where R_i is any process that leads to the formation or removal of species *i*, for instance, recombination of elements or chemical reaction in the bulk of the material [22]. In the systems studied in this thesis, due to the absence of such reactions, R_i is considered to be zero. Combination of Eqs. (1.4) and (1.5) becomes Fick's second law:

$$\frac{\partial c_i}{\partial t} = \frac{\partial}{\partial x}\left(D_i \frac{\partial c_i}{\partial x}\right) \qquad \text{(Equation 1.6)}$$

To find how the diffusion coefficient is related to the thermal movement of the species, we will consider an example of diffusion from a plane source. If initially, at $t = 0$, all the substance M is on the plane at $x = 0$, then the concentration distribution at certain time t ($t > 0$) can be written as the solution of Eqs. (1.4) and (1.6) [23].

$$c_i(x,t) = \frac{M}{2\sqrt{\pi D_i t}} exp\left(-\frac{x^2}{4D_i t}\right) \qquad \text{(Equation 1.7)}$$

The diffusion is symmetrical relatively to the origin ($x = 0$), so the average position of the diffused substance is zero at any time, but the mean square distance increases as following:

$$\bar{x}^2 = \int x^2 \frac{1}{2\sqrt{\pi D_i t}} exp\left(-\frac{x^2}{4D_i t}\right) dx = 2Dt \qquad \text{(Equation 1.8)}$$

At an atomistic level, diffusion can be considered as a phenomenon associated with the Brownian motion of atoms or ions via defects (the motion of pollen grains on the surface of water is a typical example) [24]. The simplified case is the hopping of the atom or ion with a fixed jumping frequency v and fixed jumping distance r_i. After the n^{th} jump in the time *t*, its location $\bar{R}$ will be

$$\bar{R} = \sum_{i=1}^{n} \bar{r}_i \qquad \text{(Equation 1.9)}$$

so the mean square distance $\bar{R}^2$ from the origin will be

$$\bar{R}^2 = (\sum_{i=1}^{n} \bar{r}_i)^2 = nr^2 \left(1 + \frac{2}{n} < cos\theta_{i,i+j} >\right) \qquad \text{(Equation 1.10)}$$

where $\theta_{i,i+j}$ is the angle between the i^{th} and $(i+j)^{th}$ jumps, $\frac{1}{n} < cos\theta_{i,i+j} >$ is the average of $cos\theta_{i,i+j}$. Following the equal probability of forward and backward jumps (Markovian process), $< cos\theta_{i,i+j} >$ should be equal to zero, and Eq. 1.10 will transform to

$$\bar{R}^2 = nr^2 \qquad \text{(Equation 1.11)}$$

and because $n = tv$, we have

$$\bar{R}^2 = vr^2t \qquad \text{(Equation 1.12)}$$

And from Eqs. (1.8) and (1.12), we obtain

$$D_i = \frac{1}{2}vr^2 \qquad \text{(Equation 1.13)}$$

To obtain oxygen self-diffusion coefficients in a thermal equilibrium state, tracers, such as ^{18}O, are usually used to label the movement of a certain ion (oxygen). The diffusion coefficients obtained in such experiments are tracer diffusion coefficients D^*, and are related to self-diffusion as

$$D_i^* = fD_i \qquad \text{(Equation 1.14)}$$

where f is the Haven ratio and its value, in general, is smaller than unity due to the slightly higher probability of the tracer jumps in the backward direction. Also its value depends on the crystal structure of the compound and the diffusion mechanism. For perovskites ABO_3, where oxygen transport via oxygen vacancies is predominant, its value is about 0.69 and usually approximated to 1 [25]. So Eq. (1.14) transforms to

$$D_i^* \approx D_i \qquad \text{(Equation 1.15)}$$

1.5.1.2. Electrochemical potential

Diffusion in the bulk material can be considered as chemical potential gradient of species *i* [26, 27]. The flux j_i will be expressed as,

$$j_i = -\frac{c_i D_i}{RT}\frac{\partial \mu_i}{\partial x} \qquad \text{(Equation 1.16)}$$

where μ_i is the chemical potential of the species *i* and related to the activity, a_i, as

$$\mu_i = \mu_i^0 + RT\ln a_i \qquad \text{(Equation 1.17)}$$

μ_i^0 is the reference chemical potential. Transformed Eqs. (1.16)

$$j_i = -\frac{c_i D_i}{RT}\frac{\partial \mu_i}{\partial c_i}\frac{\partial c_i}{\partial x} \qquad \text{(Equation 1.18)}$$

and (1.17)

$$\frac{\partial \mu_i}{\partial c_i} = RT\frac{\partial \ln a_i}{\partial c_i} \qquad \text{(Equation 1.19)}$$

With Eqs. (1.18) and (1.19) we can obtain

$$j_i = -D_i\frac{\partial \ln a_i}{\partial \ln c_i}\frac{\partial c_i}{\partial x} \qquad \text{(Equation 1.20)}$$

which is equivalent to Fick's first law, Eq. (1.4), if we rewrite it as follows

$$j_i = -\widetilde{D}_i\frac{\partial c_i}{\partial x} \qquad \text{(Equation 1.21)}$$

where $\widetilde{D}_i$ represents the chemical diffusion coefficient of species *i*. The relation between diffusion and chemical diffusion can be expressed as following:

$$\widetilde{D}_i = D_i\Gamma_i \qquad \text{(Equation 1.22)}$$

$$\Gamma_i = \frac{\partial \ln a_i}{\partial \ln c_i} \qquad \text{(Equation 1.23)}$$

It means, that besides the statistical contribution to diffusion, there is a chemical driving force, because of variation of free energy with concentration of species *i*,

represented by Γ_i. Γ_i is called thermodynamic factor and was introduced by Darken in 1948 [22]. In an ideal solid solution, concentration of species *i* is equal to its activity, $a_i = c_i$, then Eq. (1.20) will reduce to Fick's first law, Eq. (1.4).

Besides concentration gradient, mobile species can migrate under other forces, such as an electric field. The only force applied in the electric field is $\frac{\partial \emptyset}{\partial x}$ and the flux of the species *i* will be

$$j_i = -c_i u_i \frac{\partial \emptyset}{\partial x} \qquad \text{(Equation 1.24)}$$

where u_i is the mean drift velocity per unit field of species *i*, and is related to the conductivity σ_i as [24]

$$\sigma_i = c_i |z_i| F u_i \qquad \text{(Equation 1.25)}$$

where F is the Faraday constant and z_i is the charge on species *i*.

Hence,

$$j_i = -\frac{\sigma_i}{z_i^2 F^2} \frac{\partial z_i F \emptyset}{\partial x} \qquad \text{(Equation 1.26)}$$

which is a form of Ohm's law. With the Nernst-Einstein relation for mobility and diffusion [28]:

$$D_i = \frac{\sigma_i RT}{z_i^2 F^2 c_i} \qquad \text{(Equation 1.27)}$$

Eq. (1.26) can be rewritten as

$$j_i = -\frac{c_i D_i}{RT} \frac{\partial z_i F \emptyset}{\partial x} \qquad \text{(Equation 1.28)}$$

The general equation for the flux of species *i* can be transformed using combination of Eqs. (1.16) and (1.28) to

$$j_i = -\frac{c_i D_i}{RT} \frac{\partial \tilde{\mu}_i}{\partial x} \qquad \text{(Equation 1.29)}$$

and

$$\tilde{\mu}_i = \mu_i + z_i F\emptyset \qquad \text{(Equation 1.30)}$$

where $\tilde{\mu}_i$ is the electrochemical potential of species *i*.

Particles may also move due to the gradients in the electrochemical potentials of other species, leading to cross-terms in the flux equation. In principle, the presence of cross-terms will occur whenever a component, whose chemical potential may vary independently of that of species *i*, is present [22]. So, the flux equation may be generalized:

$$j_i = -\frac{c_i D_i}{RT}\frac{\partial(\tilde{\mu}_i + \sum_j \alpha_{ij}\tilde{\mu}_j)}{\partial x} \qquad \text{(Equation 1.31)}$$

where α_{ij} are the coefficients showing the influence of $\frac{\partial \tilde{\mu}_j}{\partial x}$ on *i*. $\tilde{\mu}_j$ is independent of $\tilde{\mu}_i$, it is not coupled through the Gibbs-Duhem relation. And in most of the cases, coupling may be neglected in comparison to the influence of $\tilde{\mu}_i$ [29].

1.5.2. Chemical diffusion in a binary system

In this chapter, charge flow in mixed conductors will be discussed [14]. In a mixed conductor in the solid state, an electronic contribution always accompanies ionic conduction. Situations where no net external current is applied will be considered. Then the internal current will be zero:

$$\sum_i j_i = 0 \qquad \text{(Equation 1.32)}$$

where j_i is the current density of the species *i*.

With the current density j_i rewritten as

$$j_i = -\frac{\sigma_i}{z_i F}\frac{\partial \tilde{\mu}_i}{\partial x} \qquad \text{(Equation 1.33)}$$

Eq. (1.32) will transform to

$$\sum_i \left(\frac{t_i}{z_i}\right) \frac{\partial \tilde{\mu}_i}{\partial x} = 0 \qquad \text{(Equation 1.34)}$$

where t_i is the transport number of species *i*

$$t_i = \frac{\sigma_i}{\sum_j \sigma_j} \qquad \text{(Equation 1.35)}$$

For simplified case, we will consider only the two fastest species

$$\frac{t_1}{z_1} \frac{\partial \tilde{\mu}_1}{\partial x} = -\frac{t_2}{z_2} \frac{\partial \tilde{\mu}_2}{\partial x} \qquad \text{(Equation 1.36)}$$

And finally,

$$j_1 = -\left(\frac{z_1 c_1 D_1 t_2}{RT}\right) \frac{\partial \left(\frac{\tilde{\mu}_1}{z_1} - \frac{\tilde{\mu}_2}{z_2}\right)}{\partial x} \qquad \text{(Equation 1.37)}$$

The driving force is a concentration gradient of a neutral species [14]. It is necessary to note that only quantities of chemical potential for neutral components are considered as 'real' thermodynamic quantities in the sense that they really can be added to the system. For charged particles, such as ions and electronic holes, chemical potentials are thermodynamically undefined since they must be added in pairs of opposite charges to keep electroneutrality. Nevertheless, they have great value for considerations based on a physical model [14].

Now, a single-phase binary system, $MO_{1-\delta}$, where the metal sublattice is not mobile and O^{2-} and e' are mobile charge carriers, will be considered. A source of neutral oxygen is required, and the mass transport for it can be expressed with single particle equation:

$$j_O = -\widetilde{D}_O \frac{\partial c_O}{\partial x} \qquad \text{(Equation 1.38)}$$

according to Eq. (1.21). $\widetilde{D}_O$ is the chemical diffusion coefficient of the neutral oxygen. And corresponding to it, we can rewrite Eqs. (1.22) and (1.23) as

$$\widetilde{D}_O = D_O \frac{\partial \ln a_O}{\partial \ln c_O} \quad \text{(Equation 1.39)}$$

$$\Gamma_O = \frac{\partial \ln a_O}{\partial \ln c_O} \quad \text{(Equation 1.40)}$$

Using Wagner's treatment, which assumes that a local chemical equilibrium is obtained between the charged species

$$O^{2-} - 2e' = O \quad \text{(Equation 1.41)}$$

we will express the chemical diffusion coefficient $\widetilde{D}_O$ using empirically obtainable parameters. But, due to the unknown internal electrical field, we have

$$\tilde{\mu}_{O^{2-}} - 2\tilde{\mu}_{e'} = \mu_O \quad \text{(Equation 1.42)}$$

with the following equations [30]

$$c_O = c_{O^{2-}} \quad \text{(Equation 1.43)}$$

$$\partial c_O = \partial c_{O^{2-}} = -\frac{1}{2}\partial c_{e'} \quad \text{(Equation 1.44)}$$

Transforming Eq. (1.37), where O^{2-} are species 1 and electrons are species 2, we obtain

$$j_O = -\left(\frac{c_{O^{2-}} D_{O^{2-}} t_{e'}}{RT}\right)\frac{\partial \mu_O}{\partial x} \quad \text{(Equation 1.45)}$$

and then

$$D_O = t_{e'} D_{O^{2-}} \Gamma_O \quad \text{(Equation 1.46)}$$

With the assumption that neutral oxygen in the solid is in equilibrium with the oxygen in the ambient, $O = \frac{1}{2}O_2$, we have

$$\mu_O = \frac{1}{2}\mu_{O_2} \quad \text{(Equation 1.47)}$$

$$\mu_O^0 + RT\ln a_O = \frac{1}{2}\left(\mu_{O_2}^0 + RT\ln\frac{p_{O_2}}{p^0}\right) \quad \text{(Equation 1.48)}$$

Hence,

$$\Gamma_O = \frac{1}{2}\frac{\partial\left(\frac{\ln p_{O_2}}{p^0}\right)}{\partial \ln c_O} \qquad \text{(Equation 1.49)}$$

where, Γ_O is the thermodynamic factor, which corresponds to oxygen concentration in the material at different conditions, such as temperature and oxygen partial pressure in the surroundings. It is usually determined from thermogravimetric or coulometric measurements, where the oxygen concentration in a material at different oxygen partial pressures can be obtained [31].

Taking into account that in materials studied in this thesis, electronic conductivity is dominant, we have

$$\widetilde{D}_O \approx D_{O^{2-}}\Gamma_O \qquad \text{(Equation 1.50)}$$

Another assumption of 'quasi-neutrality' is usually used in the ambipolar theory, which assumes that in the absence of an electric field both charge carriers obey Fick's first law [14]. It says that an attractive electrostatic field is formed by a slight readjustment of the charge balance and that two species have an ambipolar diffusion coefficient, D_a. This charge readjustment is such that the following equation holds,

$$z_1 \frac{\partial c_1}{\partial x} + z_2 \frac{\partial c_2}{\partial x} = 0 \qquad \text{(Equation 1.51)}$$

By combining Eqs. (1.37) and (1.51), D_a can be obtained as

$$D_a = D_1 t_2 + D_2 t_1 \qquad \text{(Equation 1.52)}$$

where D_a is a weighted mean of individual diffusivities. And for the binary system,

$$D_a = D_{O^{2-}} t_{e^-} + D_{e'} t_{O^{2-}} \qquad \text{(Equation 1.53)}$$

This treatment is similar to Wagner's treatment, where with Eqs. (1.43) and (1.52) and with following relation [32]

$$j_O = j_{O^{2-}} = -\frac{1}{2} j_{e'} \qquad \text{(Equation 1.54)}$$

Eq. (1.38) will produce

$$j_{O^{2-}} = -\widetilde{D}_O \frac{\partial c_{O^{2-}}}{\partial x} \qquad \text{(Equation 1.55)}$$

$$j_{e^-} = -\widetilde{D}_O \frac{\partial c_{e'}}{\partial x} \qquad \text{(Equation 1.56)}$$

And an expression, similar to 'quasi-neutral' condition, Eq. (1.51), can be produced. With Eq. (1.27) for oxygen ion species,

$$D_{O^{2-}} = \frac{\sigma_{O^{2-}} RT}{4F^2 c_{O^{2-}}} \qquad \text{(Equation 1.57)}$$

So, $\widetilde{D}_O$ in Eq. (1.46) can be written as

$$\widetilde{D}_O = \frac{1}{4F^2} \frac{\sigma_{e'} \sigma_{O^{2-}}}{\sigma_{e'} + \sigma_{O^{2-}}} \frac{\partial \mu_O}{\partial c_{O^{2-}}} \qquad \text{(Equation 1.58)}$$

And using Eqs. (1.43), (1.44) and (1.54), Eq. (1.58) can be rewritten as

$$\widetilde{D}_O = \frac{RT}{4F^2} \frac{\sigma_{e'} \sigma_{O^{2-}}}{\sigma_{e'} + \sigma_{O^{2-}}} \left(\frac{\Gamma_{O^{2-}}}{c_{O^{2-}}} + \frac{4\Gamma_{e'}}{c_{e'}} \right) \qquad \text{(Equation 1.59)}$$

This equation connects chemical diffusion to self-diffusion coefficients of oxygen ions, of electrons and their thermodynamic factors. It can be rewritten as

$$\widetilde{D}_O = D_{O^{2-}} t_{e'} \Gamma_{O^{2-}} + D_{e'} t_{O^{2-}} \Gamma_{e'} \qquad \text{(Equation 1.60)}$$

For diluted defects [33], when

$$\Gamma_{O^{2-}} \equiv \frac{\partial \ln a_{O^{2-}}}{\partial \ln c_{O^{2-}}} \approx \Gamma_{e'} \equiv \frac{\partial \ln a_{e'}}{\partial \ln c_{e'}} \approx 1 \qquad \text{(Equation 1.61)}$$

$\widetilde{D}_O$ becomes an equivalent of D_a

$$\widetilde{D}_O = D_{O^{2-}} t_{O^{2-}} + D_{e'} t_{e'} \qquad \text{(Equation 1.62)}$$

A theoretical description for a binary system (oxygen ions and electrons) was considered without taking into account the oxygen transport mechanism. A similar situation as in the motion of electrons and backward motion of electron holes occurs in the crystal lattice, where oxygen ions diffuse through fully ionized oxygen vacancies $V_O^{\cdot\cdot}$. In this case, conductivity of oxygen ions will be the same as the conductivity of oxygen vacancies. Hence,

$$\sigma_{V_O^{\cdot\cdot}} = \sigma_{O^{2-}} \qquad \text{(Equation 1.63)}$$

Using Eq. (1.27), Eq. (1.63) transforms to:

$$D_{O^{2-}} c_{O^{2-}} = D_{V_O^{\cdot\cdot}} c_{V_O^{\cdot\cdot}} \qquad \text{(Equation 1.64)}$$

As in Eq. (1.46), chemical diffusion relates to oxygen vacancies as

$$\widetilde{D}_O = t_{e'} D_{V_O^{\cdot\cdot}} \Gamma_V \qquad \text{(Equation 1.65)}$$

Similarly to Eq. (1.49) for the thermodynamic factor for oxygen ions,

$$\Gamma_V = -\frac{1}{2} \frac{\partial \ln p_{O_2}}{\partial \ln c_{V_O^{\cdot\cdot}}} \qquad \text{(Equation 1.66)}$$

An equation for thermodynamic factor for oxygen vacancies can be derived.

1.5.3. Surface exchange mechanism

The mechanism of surface exchange reaction at the gas-solid interface, in comparison with diffusion mechanism, is much more complicated. It may involve charge transfer, adsorption and dissociation of oxygen molecules, surface diffusion, incorporation of oxygen at the surface layer with the following reduction, and reverse steps for the reoxidation of oxygen ions [31]. The combination of these steps often occurs.

Several possible mechanisms of surface exchange reaction have been proposed [35-37]. For example, Boukamp *et al*. reported the following mechanism:

$O_2(\text{gas}) \rightarrow O_2(\text{pore})$ (diffusion into pore)

$O_2(\text{gas}) + S_{ad} \rightarrow O_2(\text{adsorbed})$ (adsorption)

$O_2(\text{ad}) + e' \rightarrow O_2'(\text{ad})$ (charge transfer)

$O_2'(\text{ad}) + S_{ad} + e' \rightarrow 2O'(\text{ad})$ (dissociation)

$O'(\text{ad}) + V_O^{\cdot\cdot} + e' \rightarrow O_O^{\times} + S_{ad}$ (charge transfer and incorporation)

With the localization of electronic defects on the transition metal on the perovskite B-site, the dominant conduction mechanism is small polaron hopping in most MIEC oxides.

To obtain information about surface exchange process, attempts to identify and quantify the oxygen species and defects located on the surface of the MIEC oxides using *in situ* analytical instruments have been made. However, most of the analytical tools are applied only to systems under vacuum, what is far from the conditions at which mixed ionic electronic oxides are used [38].

It has to be noted that, depending on used experimental technique, three different surface exchange rate constants can be determined: k^Q from electrical experiments, k_{chem} from chemical experiments, and k^* from isotope exchange experiments. A theoretical relationships between these surface exchange rates have been studied by Maier [38] on mixed ionic and electronic conductor with large electronic conductivity and electronic carrier species. Following dependencies were found:

$$k^Q \approx k^* \qquad \text{(Equation 1.67)}$$

$$k_{chem} = k^* \Gamma_O \qquad \text{(Equation 1.68)}$$

Eq. (1.68) is the analogue of the Eq. (1.50) for relationship between oxygen self-diffusion and chemical oxygen diffusion.

Another model of the surface exchange reaction has been suggested in our group in 2000. This model simplifies the mechanism by summarizing all intermediate steps into one reaction:

$$\frac{1}{2} O_2 + V_O^{\cdot\cdot} \leftrightarrow O_O^{\times} + 2h^{\cdot} \qquad \text{(Equation 1.69)}$$

As a result, the equation of chemical surface exchange was obtained:

$$k_{chem} = k_f \left(\frac{p}{p_0}\right)^{0.5} \left[1 + c_{ve} \left(\frac{1}{c_{ie}} + \frac{4}{c_{he}}\right)\right] \qquad \text{(Equation 1.70)}$$

where k_f is the forward reaction rate, Eq. (1.69), and contains both a constant of proportionality between the surface vacancy concentration and bulk vacancy concentration, and width of the surface region. p is the oxygen gas pressure, while p_0 is the pressure of 1 atm. c_{ve}, c_{ie} and c_{he} are molar concentrations of oxygen vacancies, oxygen ions and electron holes at equilibrium, respectively. It is necessary to note that equilibrium values of concentrations are related to the oxygen partial pressure and temperature in the surroundings. Relationships between the three surface exchange constants, k^Q, k_{chem} and k^*, are the same as in Eqs. (1.67) and (1.68).

1.6. References

1. Gellings, P. J.; Bouwmeester, H. J. M. Ion and mixed conducting oxides as catalysts. *Catalysis Today* **1992**, *12*, 1-101.

2. Islam, M. S. Ionic transport in ABO_3 perovskite oxides: A computer modelling tour. *J. Mater. Chem.* **2000**, *10*, 1027-1038.

3. Riess, I. *The CRC handbook of solid state electrochemistry*. Gellings, P. J.; Bouwmeester, H. J. M., Eds.; CRC press: Boca Raton, 1997; pp 223-231.

4. Kartha, S.; Grimes, P. Fuel cells: Energy conversion for the next century. *Physics Today* **1994**, November, 54-61.

5. De Souza, R. A.; Kilner, J. A. Oxygen transport in $La_{1-x}Sr_xMn_{1-y}Co_yO_{3\pm\delta}$ perovskites: Part I. Oxygen tracer diffusion. *Solid State Ionics* **1998**, *106*, 175-187.

6. De Souza, R. A.; Kilner, J. A. Oxygen transport in $La_{1-x}Sr_xMn_{1-y}Co_yO_{3\pm\delta}$ perovskites: Part II. Oxygen surface exchange. *Solid State Ionics* **1999**, *126*, 153-161.

7. Lee, T. H.; Yang, Y. L.; Jacobson, A. J.; Abeles, B.; Milner, S. Oxygen permeation in $SrCoFeO_{3-\delta}$ membranes with porous electrodes. *Solid State Ionics* **1997**, *100*, 87-94.

8. Lee, T. H.; Yang, Y. L.; Jacobson, A. J.; Abeles, B.; Zhou, M. Oxygen permeation in dense $SrCo_{0.8}Fe_{0.2}O_{3-\delta}$ membranes: Surface exchange kinetics versus bulk diffusion. *Solid State Ionics* **1997**, *100*, 77-85.

9. Kim, S.; Yang, Y. L.; Jacobson, A. J.; Abeles, B. Diffusion and surface exchange coefficients in mixed ionic electronic conducting oxides from the pressure dependence of oxygen permeation. *Solid Sate Ionics* **1998**, *106*, 189-195.

10. Kim, S.; Yang, Y. L.; Christoffersen, R.; Jacobson, A. J. Determination of oxygen permeation kinetics in a ceramic membrane based on the composition $SrFeCo_{0.5}O_{3.25-\delta}$. *Solid State Ionics* **1998**, *109*, 187-196.

11. Kim, S.; Yang, Y. L.; Jacobson, A. J.; Abeles, B. Oxygen surface exchange in mixed ionic electronic conductor membranes. *Solid Sate Ionics* **1999**, *121*, 31-36.

12. Kim, S.; Yang, Y. L.; Christoffersen, R.; Jacobson, A. J. Oxygen permeation, electrical conductivity and stability of the perovskite oxide $La_{0.2}Sr_{0.8}Cu_{0.4}Co_{0.6}O_{3-x}$. *Solid State Ionics* **1997**, *104*, 57-62.

13. Adler, S. B. Mechanism and kinetics of oxygen reduction on porous $La_{1-x}Sr_xCoO_{3-\delta}$ electrodes. *Solid State Ionics* **1998**, *111*, 125-134.

14. Heyne, L. Electrochemistry of mixed ionic-electronic conductors. Solid Electrolytes. In *Topics in Applied Physics*; Geller, S., Ed.; Springer: Berlin, 1997; Vol. 21; pp 169-221.

15. Goldschmidt, V. M. Die gesetze der krystallochemie. *Die naturwissenschaften* **1926**, *21*, 477-485.

16. Goldschmidt, V. M. The laws of chemical crystallography. *Geochemische verteilungsgesetze der elemente* **1927**, *VII-VIII*, 28-33.

17. Maier, J. Mass transport in the presence of internal defect reactions – concept of conservative ensembles: I, Chemical diffusion in pure compounds. *J. Am. Ceram. Soc*. **1993**, *76*, 1212-1217.

18. Anderson, H. U. Review of p-type doped perovskite materials for SOFC and other applications. *Solid State Ionics* **1992**, *52*, 33-41.

19. Zener, C. Interaction between the d-shells in the transition metals. II. Ferromagnetic compounds of manganese with perovskite structure. *Phys. Rev.* **1952**, *82*, 403-405.

20. Teraoka, Y.; Zhang, H. M.; Okamoto, K.; Yamazoe, N. Mixed ionic-electronic conductivity of $La_{1-x}Sr_xCo_{1-y}Fe_yO_{3-\delta}$ perovskite-type oxides. *Mater. Res. Bull.* **1988**, *23*, 51-58.

21. Schmalzried, H. *Chemical kinetics of solids*; VCH: Weinheim, 1995; p 61.

22. Raistrick, I. D.; Macdonald, J. R.; Franceschetti, D. R. *Impedance spectroscopy – emphasizing solid materials and systems*; Macdonald, J. R., Ed.; John Wiley & Sons: New York, 1987; p 27.

23. Crank, J. *The mathematics of diffusion*; Clarendon Press: Oxford, 1975; p 12.

24. Kudo, T.; Fueki, K. *Solid state ionics*; Kodansha/VCH: Weinheim, 1990; p 47.

25. De Souza, R. A.; Kilner, J. A. Oxygen transport in $La_{1-x}Sr_xMn_{1-y}Co_yO_{3\pm\delta}$ perovskites: Part I. Oxygen tracer diffusion. *Solid State Ionics* **1998**, *106*, 175-187.

26. Einstein, A. Über die von der molekularkinetischen theorie der wärme geforderte bewegung von in ruhenden flüssigkeiten suspendierten teilchen. *Annalen der Physik* **1905**, *17*, 549-560.

27. Hartley, G. S. Diffusion and distribution in a solvent of graded composition. *Trans. Faraday Soc.* **1931**, *27*, 10-29.

28. Maier, J. Defect chemistry: Composition, transport, and reactions in the solid state; Part II: Kinetics. *Angew. Chem. Int. Ed. Engl*. **1993**, *32*, 528-542.

29. Weppner, W. *Solid State Electrochemistry*; Bruce, P.G., Ed.; Cambridge University Press: Cambridge, 1995; p 199.

30. Maier, J. Mass transport in the presence of internal defect reactions — concept of conservative ensembles: II, evaluation of electrochemical transport measurements. *J. Am. Ceram. Soc*. **1993**, *76*, 1218-1222.

31. Bouwmeester, H. J. M.; Burggraaf, A. J. *The CRC handbook of solid state electrochemistry*; Gellings, P. J.; Bouwmeester, H. J. M., Eds.; CRC press: Boca Raton, 1997; p 481.

32. Maier, J. Mass transport in the presence of internal defect reactions — concept of conservative ensembles: III, trapping effect of dopants on chemical diffusion. *J. Am. Ceram. Soc*. **1993**, *76*, 1223-1227.

33. Maier, J. Mass transport in the presence of internal defect reactions—concept of conservative ensembles: IV, tracer diffusion and intercorrelation with chemical diffusion and ion conductivity. *J. Am. Ceram. Soc*. **1993**, *76*, 1228-1232.

34. Schmalzried, H. *Chemical Kinetics of Solids*; VCH: Weinheim, 1995; p 2.

35. Boukamp, B. A.; van Hassel, B. A.; Vinke, I. C.; de Vries, K. J.; Burggraaf, A. J. The oxygen transfer process on solid oxide/noble metal electrodes, studied with impedance spectroscopy, dc polarization and isotope exchange. *Electrochimica Acta* **1993**, *38*, 1817-1825.

36. Mizusaki, J.; Amano, K.; Yamauchi, S.; Fueki, K. Electrode reaction at Pt, $O_{2(g)}$/stabilized zirconia interfaces. Part I: Theoretical consideration of reaction model. *Solid State Ionics* **1987**, *22*, 313-322.

37. Adler, S. B.; Lane, J. A.; Steele, B. C. H. Electrode kinetics of porous mixed-conducting oxygen electrodes. *J. Electrochem. Soc*. **1996**, *143*, 3554-3564.

38. Maier, J. On the correlation of macroscopic and microscopic rate constants in solid state chemistry. *Solid State Ionics* **1998**, *112*, 197-228.

39. Kim, S.; Wang, S.; Chen, X.; Yang, Y. L.; Wu, N.; Ignatiev, A.; Jacobson, A. J.; Abeles, B. Oxygen surface exchange in mixed ionic electronic conductors: Application to $La_{0.5}Sr_{0.5}Fe_{0.8}Ga_{0.2}O_{3-\delta}$. *J. Electrochem. Soc*. **2000**, *147*, 2398-2406.

Chapter 2. Theoretical background of the techniques used to study oxygen transport

In this chapter, the theoretical background of the different techniques used to investigate oxygen diffusion is summarized. Analysis of electrical conductivity relaxation (ECR) and isotope exchange depth profiling (IEDP) experiments are described. In the last part, the application of molecular dynamic simulations (MD) to study oxygen transport in perovskites and perovskite-related compounds is summarized.

2.1. Electrical conductivity relaxation (ECR)

2.1.1. Introduction

Relaxation experiments are widely used in studying kinetic processes. The change in a specific property of the system to a new state can be observed after the system experiences a change in its physical or chemical environment. Any property that reflects the oxygen concentration, such as conductivity, volume, weight, and optical properties, can be used to study the oxygen transport in the system [1]. Relaxation experiments on mixed ionic and electronic oxides can be easily carried out by rapid changing of the oxygen partial pressure in the surroundings while holding the sample at a constant temperature, using the relation between the oxygen concentration and the oxygen partial pressure.

One of the most direct techniques to measure the change in oxygen content in the compound is by using the thermogravimetric analysis (TGA) method. Morin *et al.* published the results of gravimetric relaxation experiments on $La_{0.5}Sr_{0.5}CoO_{3-\delta}$ [2]. However, such thermogravimetric experiments are subject to gas-flow fluctuations, which

are especially significant at the early stage of the relaxation process. Short-time data are necessary to separate surface and bulk processes and, consequently, it is difficult to obtain reliable results by this technique. Electrical conductivity relaxation experiments are almost not affected by such fluctuations in gas flows and other minor physical vibrations. In addition, conductivity measurements are extremely sensitive to the defects presence [3-5]. Therefore, ECR is the most commonly used relaxation method [5, 6-19].

As described in Chapter 1, the oxygen transport in a dense mixed ionic and electronic oxide can be considered as a two step process that involves surface exchange and bulk diffusion. The mathematical solutions of the mass transport equations under various conditions are well established using a linear surface exchange model [20]. They are widely used in analysis of ECR data by establishing the relationship between electrical conductivity of the sample and the oxygen concentration in it. In this part of the chapter, these solutions and their theoretical basis are described.

Electrical conductivity relaxation experiments require no oxygen concentration variation along the conductivity measurement direction during the ECR process. Therefore, one dimension of the sample is reserved for the conductivity measurement in contrast to gravimetric measurements, where the mass change is measured for the whole sample. Moreover, unlike gravimetric experiments, the electrical conductivity relaxation method requires samples with specific geometry.

2.1.2. Theoretical background

Starting with a one-dimensional example of the mathematical description of the oxygen concentration change with time during an ECR experiment for a MIEC oxide, we will subsequently describe a three-dimensional case. For the one-dimensional example we will consider a plane sheet, where thickness is significantly smaller in comparison with its width and length. In this case, the number of oxygen atoms entering through the edges can be considered to be negligible compared with the number of oxygen atoms entering through the plane faces.

The oxygen concentration and the oxygen flux depend on both position and time. For a plane sheet with thickness *2l* and two parallel faces located at $x = \pm l$ (Figure 2.1), according to Wagner's theory, described in Chapter 1, and to the mass conservation law, we can write:

$$j_{O^{2-}}(x,t) = -\widetilde{D}_O \frac{\partial c_{O^{2-}}(x,t)}{\partial x} \qquad \text{(Equation 2.1)}$$

$$\frac{\partial c_{O^{2-}}(x,t)}{\partial t} = -\frac{\partial j_{O^{2-}}(x,t)}{\partial x} \qquad \text{(Equation 2.2)}$$

where $\widetilde{D}_O$ is the chemical diffusion coefficient.

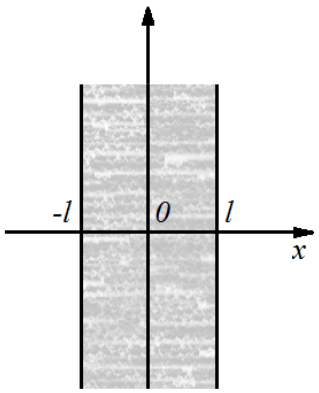

Figure 2.1. Schematic representation of the one-dimensional sample.

It is necessary to mention that Eqs. (2.1) and (2.2) are the basis for both electrical conductivity relaxation and isotope exchange depth profiling experiments, with the only difference being that, in the case of IEDP experiments, $\widetilde{D}_O$ will be substituted with D^*, representing the tracer diffusion coefficient.

For relaxation experiments the initial condition is

$$c_{O^{2-}}(x, 0) = c_{O^{2-}}^{(1)} \qquad \text{(Equation 2.3)}$$

where $c_{O^{2-}}^{(1)}$ is the oxygen ion concentration in the bulk solid sample in equilibrium with the initial oxygen partial pressure in the surroundings, $pO_2^{(1)}$.

Then the boundary condition due to the symmetry of the sample along *x* axis is

$$\left.\frac{\partial c_{O^{2-}}}{\partial x}\right|_{x=0} = 0 \qquad \text{(Equation 2.4)}$$

The boundary conditions on the two surfaces of the sample depends on the relative rates of bulk diffusion and surface exchange.

If the surface exchange reaction is so fast that the surface of the sample instantly reaches equilibrium with the new oxygen partial pressure in the surroundings, then oxygen transport is limited by the bulk diffusion. For the diffusion-limited case, the boundary conditions at $x = \pm l$ can be written as:

$$c_{O^{2-}}(\pm l, t) = c_{O^{2-}}^{(2)} \qquad \text{(Equation 2.5)}$$

where $c_{O^{2-}}^{(2)}$ is the oxygen ion concentration in the bulk solid sample in equilibrium with the final oxygen partial pressure in the surroundings, $pO_2^{(2)}$.

The analytical solution of the mass change in this case can be obtained from Eqs. (2.1) – (2.5) and was described by Franke *et al.* [20]:

$$\frac{M_t}{M_\infty} = 1 - \sum_{n=0}^{\infty} \frac{8}{(2n+1)^2\pi^2} exp\left[-\frac{(2n+1)^2\pi^2\tilde{D}_O t}{4l^2}\right] \qquad \text{(Equation 2.6)}$$

where M_t is the total amount of oxygen that has entered the sample up to time *t*, M_∞ is the amount of oxygen that has entered the sample up to an infinite time, so $\frac{M_t}{M_\infty}$ represents the fractional change of the total mass of oxygen.

The values of M_t and M_∞ can be calculated as:

$$M_t = Am_O \int_{-l}^{l} (c_{O^{2-}}(x,t) - c_{O^{2-}}^{(1)})dx =$$

$$= 2lAm_O(c_{O^{2-}}(t) - c_{O^{2-}}^{(1)}) \qquad \text{(Equation 2.7)}$$

$$M_\infty = 2lAm_O(c_{O^{2-}}^{(2)} - c_{O^{2-}}^{(1)}) \qquad \text{(Equation 2.8)}$$

respectively, where *A* is the surface area of the sample and m_O is the atomic mass of oxygen. $c_{O^{2-}}(t)$ represents the average concentration of oxygen at time *t*. Diffusion-limited transport has been usually assumed in the analyses of electrical conductivity relaxation experiments [5].

An increase in the number of materials with high values of diffusion coefficients and progress in thin film deposition of ceramics has led to the recognition that the oxygen transport in many materials is not only controlled by bulk diffusion, but also by the surface exchange between material and gas in the surroundings [20-24].

Following the assumption of linear reaction kinetics for the mixed controlled transport, the boundary conditions at $x = \pm l$ are [25, 26]:

$$k_{chem}(c_{O^{2-}} - c_{O^{2-}}^{(2)}) = -\tilde{D}_O \left.\frac{\partial c_{O^{2-}}}{\partial x}\right|_{x=\pm l} \qquad \text{(Equation 2.9)}$$

where k_{chem} represents the chemical surface exchange coefficient (unit: cm/s).

To avoid significant changes in physical and chemical properties of the sample, it is necessary to have the magnitude of the pO_2 change reasonable small.

The analytical solution of Eqs. (2.1) – (2.4) with the boundary condition provided by Eq. (2.9) is

$$\frac{M_t}{M_\infty} = 1 - \sum_{m=1}^{\infty} \frac{2C^2 \exp(-\frac{\alpha_m^2 \tilde{D}_O t}{l^2})}{\alpha_m^2(\alpha_m^2 + C^2 + C)} \qquad \text{(Equation 2.10)}$$

where C is a measure of importance of the surface exchange reaction contribution, and can be found as the ratio of the half thickness of the sample to a characteristic thickness, l_d,

$$C = \frac{l}{l_d} \qquad \text{(Equation 2.11)}$$

$$l_d = \frac{\tilde{D}_O}{k_{chem}} \qquad \text{(Equation 2.12)}$$

Since both, $\widetilde{D}_O$ and k_{chem}, may vary with the microstructure and surface properties of each individual sample, and with temperature and oxygen partial pressure in the surroundings, the parameter l_d does not represent an intrinsic material property [27].

The coefficient α_m is the positive root of the transcendental equation

$$\alpha_m tan\alpha_m = C \qquad \text{(Equation 2.13)}$$

In case of oxygen transport controlled by bulk diffusion, the value of C is much larger than unity, and Eq. (2.10) transforms to Eq. (2.6).

For transport limited by surface exchange reaction, the value of C is very small, and Eq. (2.10) becomes

$$\frac{M_t}{M_\infty} = 1 - \exp\left(-\frac{t}{\tau}\right) \qquad \text{(Equation 2.14)}$$

and the value of the surface exchange coefficient can be written as

$$k_{chem} = \frac{l}{\tau} \qquad \text{(Equation 2.15)}$$

There is no oxygen concentration distribution along the *x* axis, so we can directly rewrite the mass conservation law as:

$$\frac{\partial c_{O^{2-}}(x,t)}{\partial t} = -\left(2\frac{A}{V}\right) k_{chem}\left(c_{O^{2-}} - c_{O^{2-}}^{(2)}\right) \qquad \text{(Equation 2.16)}$$

Integration of Eq. (2.16) gives the same expression as Eqs. (2.14) and (2.15).

From the one-dimensional case, respective equations for the three-dimensional case can be obtained.

When we use a bar sample with finite dimensions, the oxygen transport will be along all three directions. The fractional change $\frac{M_t}{M_\infty}$ can be obtained from the solution for the one-dimensional case, Eq. (2.10) [19]. And for a bar sample with dimensions $2l_1 \times 2l_2 \times 2l_3$, we can rewrite Eq. (2.10) as:

$$\frac{M_t}{M_\infty} = 1 - \sum_{m=1}^{\infty}\sum_{n=1}^{\infty}\sum_{q=1}^{\infty} \frac{2C_1^2 \exp\left(-\frac{\alpha_{1m}^2 \tilde{D}_O t}{l_1^2}\right)}{\alpha_{1m}^2(\alpha_{1m}^2 + C_1^2 + C_1)} \times \frac{2C_2^2 \exp\left(-\frac{\alpha_{2n}^2 \tilde{D}_O t}{l_2^2}\right)}{\alpha_{2n}^2(\alpha_{2n}^2 + C_2^2 + C_2)} \times \frac{2C_3^2 \exp\left(-\frac{\alpha_{3q}^2 \tilde{D}_O t}{l_3^2}\right)}{\alpha_{3q}^2(\alpha_{3q}^2 + C_3^2 + C_3)} \qquad \text{(Equation 2.17)}$$

where C_1, C_2 and C_3 are the dimensionless parameters defined as in Eq. (2.11) for the corresponding dimensions, α_{1m}, α_{2n} and α_{3q} are the positive roots of corresponding transcendental equations, respectively. In two-dimensional case, where one dimension is much larger than two others, l_1, $l_2 << l_3$, Eq. (2.17) reduces to,

$$\frac{M_t}{M_\infty} = 1 - \sum_{m=1}^{\infty}\sum_{n=1}^{\infty} \frac{2C_1^2 \exp\left(-\frac{\alpha_{1m}^2 \tilde{D}_O t}{l_1^2}\right)}{\alpha_{1m}^2(\alpha_{1m}^2 + C_1^2 + C_1)} \times \frac{2C_2^2 \exp(-\frac{\alpha_{2n}^2 \tilde{D}_O t}{l_2^2})}{\alpha_{2n}^2(\alpha_{2n}^2 + C_2^2 + C_2)}$$

(Equation 2.18)

In the surface-limited transport case, Eq. (2.14) still applies, so the Eq. (2.15) transforms to:

$$k_{chem} = \frac{\left(l_1^{-1} + l_2^{-1} + l_3^{-1}\right)^{-1}}{\tau} \quad \text{(Equation 2.19)}$$

for the three-dimensional surface limited transport case and

$$k_{chem} = \frac{\left(l_1^{-1} + l_2^{-1}\right)^{-1}}{\tau} \quad \text{(Equation 2.20)}$$

for two-dimensional surface limited transport case.

The relationship between sample conductivity and oxygen content in it is established via the requirement of local charge neutrality [1]. Considering the case of the acceptor doped perovskite oxide, $A_{1-x}D_xBO_{3-\delta}$, where D is a divalent dopant (so the compound becomes oxygen deficient, and oxygen vacancies are formed), and B is a transitional metal, the requirement of local charge neutrality can be written as:

$$[e'] + [D_A'] = 2[V_O^{\cdot\cdot}] + [h^{\cdot}] \quad \text{(Equation 2.21)}$$

where e' and $h^{\cdot}$ are the electron and electron hole, respectively, D_A' is the defect formed by D ion occupying an A lattice site, and $V_O^{\cdot\cdot}$ is a fully charged oxygen vacancy.

Considering the region where only one electronic species dominates, for example, an exclusive *p*-type region, which is common for mixed ionic and electronic oxides, and according to Eq. (1.25), the electron holes conductivity is:

$$\sigma_h(x,t) = [h^{\cdot}](x,t) F u_h(x,t) \quad \text{(Equation 2.22)}$$

where u_h is mobility of the charge carrier.

The conductivity $\sigma(t)$ on a macroscopic scale is measured along the direction perpendicular to the oxygen flux. In the case of a one-dimensional sample, cutting the sample perpendicular to the *x* axis into an infinite number of parallel layers will show uniform oxygen ion concentration and, as a result, uniform local conductivity $\sigma_h(x,t)$. The equivalent circuit can be expressed as a parallel connection of an infinite number of resistors with a conductivity $\sigma(t)$ [5].

$$\sigma(t) = \frac{1}{2l}\int_{-l}^{l} \sigma_h(x,t)dx \qquad \text{(Equation 2.23)}$$

For a small oxygen partial pressure changes in the surroundings, the mobility of the charge carrier, u_h, can be approximated as a constant [19]. By combination of Eqs. (2.22) and (2.23) the macroscopic electron hole conductivity can be rewritten as:

$$\sigma(t) = \frac{Fu_h}{2l}\int_{-l}^{l} [h^{\cdot}](x,t)dx \qquad \text{(Equation 2.24)}$$

In the case of an exclusive *p*-type conductivity, using requirement for local charge neutrality, Eq. (2.21), we can obtain

$$\frac{[h^{\cdot}](x,t)-[h^{\cdot}]^{(1)}}{[h^{\cdot}]^{(2)}-[h^{\cdot}]^{(1)}} = \frac{[V_O^{\cdot\cdot}(x,t)]-\left[V_O^{\cdot\cdot(1)}\right]}{\left[V_O^{\cdot\cdot(2)}\right]-\left[V_O^{\cdot\cdot(1)}\right]} \qquad \text{(Equation 2.25)}$$

where the superscripts (1) and (2) corresponds to initial and final states.

Using the conservation law for oxygen [5]

$$[O_O^{\times}] + [V_O^{\cdot\cdot}] = 3\frac{N_a}{V_m} \qquad \text{(Equation 2.26)}$$

where N_a is Avogadro's number and V_m is the molar volume, and by combining Eqs. (2.7), (2.8), (2.21), (2.24) and (2.25), we can write the relation between the mass transport and conductivity change as:

$$\frac{M_t}{M_\infty} = \frac{c_{O^{2-}}(t) - c_{O^{2-}}^{(1)}}{c_{O^{2-}}^{(2)} - c_{O^{2-}}^{(1)}} = \frac{\sigma(t) - \sigma^{(1)}}{\sigma^{(2)} - \sigma^{(1)}} = g(t) \qquad \text{(Equation 2.27)}$$

where $\sigma^{(1)}$ and $\sigma^{(2)}$ are the values of electrical conductivity at initial and final states, respectively, $g(t)$ is the relative conductivity.

Eq. (2.27) also applies in the case of an exclusive *n*-type conductivity, and the requirement of $V_O^{\cdot\cdot}$ to be the fully charged point defect is not necessary, but used only to simplify mathematical equations.

2.1.3. Sample geometry requirements

In the case of oxygen transport being limited in all three dimensions by surface exchange reaction, the oxygen concentration will be uniform inside the whole sample. Electrical conductivity relaxation data can be analyzed directly with a three-dimensional transport equation. To fulfill the uniform-conductivity requirement, the length of the sample in the conductivity measurement direction should be infinite, what limits the shape of the sample to either a plate (one-dimension) or a bar (two-dimensions).

The influence of the geometry of the sample on the electrical conductivity relaxation data was studied by Wang [28]. Model calculations showed that a two-dimensional sample geometry (a bar) gives better sensitivity than a one-dimensional sample geometry (a thin plate). Taking into account the following relationships:

$$C = \frac{l}{\tilde{D}_O} k_{chem} \qquad \text{(Equation 2.28)}$$

$$k_{chem} = k_0 \cdot pO_2^n \qquad \text{(Equation 2.29)}$$

where k_0 is a constant and n represents exchange reaction mechanism, it was found that when the length of the sample is 10 times larger than its thickness, the error caused by the limited length can be neglected in the range of $0.25 \leq n \leq 0.75$ and $0.1 \leq C \leq 25$, with C being equal to the half the ratio of the thickness of the sample to its characteristic length (l_d, Eq. (2.12)). At these conditions the parameters $\widetilde{D}_O$ and k_{chem}, representing chemical oxygen diffusion and chemical surface exchange rate coefficients, respectively, can be obtained simultaneously.

2.2. Isotope exchange depth profiling

2.2.1. Introduction

A second method used to investigate oxygen transport is isotope exchange depth profiling (IEDP). The combination of IEDP with secondary ion mass spectrometry (SIMS) is the only direct method of measuring of oxygen kinetics in a material. Successful studies of oxygen diffusion with IEDP have been reported for single crystals [29-32], thin films [33] and heterostructural layers [34, 35].

During an isotope exchange depth profiling experiment, tracer atoms, usually, long living radioactive isotope tracers, are introduced into the sample. The most common way of introduction of tracer atoms is annealing in the atmosphere of radioactive isotope under controlled conditions. The measurement of the diffusion profile within the sample can be done by a variety of methods; the most usually used is sectioning the sample perpendicular to the isotope exchange direction and measuring the activity of the slices.

^{18}O is the most often used isotope tracer in oxygen diffusion studies with IEDP method. Its natural abundance is about 0.21% and it can be available for experiments in highly enriched form.

In contrast to the electrical conductivity relaxation technique, isotope exchange depth profiling allows measurement of oxygen diffusion coefficients in both electron-conducting and dielectric materials [36, 37] over a wide range of temperature, and in case of single crystals, along different crystallographic directions [38]. The ECR can only be used on mixed ionic electronic conductors and the anisotropic character of oxygen diffusion cannot be studied. However, IEDP/SIMS requires the use of expensive ^{18}O, and secondary ion mass spectrometry is a destructive method of analysis, due to the sputtering of the ions from the surface of the sample.

2.2.2. Theoretical background

Due to the fact that in IEDP experiments concentrations of tracer atoms are measured directly, the samples must be of sufficient size, so that the diffusion fronts from all the surfaces of the sample do not meet in the center. In this case, a solution to the diffusion equations can be used corresponding to diffusion in a semi-infinite medium with following assumptions:

1. At any time the rate of exchange is directly proportional to the difference between the actual concentration in the surface, c_s, and the concentration c_g, which would be in equilibrium with the vapor pressure in the atmosphere remote from the surface.

2. c_g is a constant during the exchange experiment.

3. The exchange experiment time and the sample dimensions are chosen such that the case of diffusion in a semi-infinite medium can be applied.

Then the boundary condition at the surface can be written as:

$$-D^* \frac{\partial c}{\partial x}\Big|_{x=0} = k^*(c_g - c_s) \qquad \text{(Equation 2.30)}$$

where D^* is the oxygen tracer diffusion coefficient and k^* is the tracer surface exchange rate.

Note, we are discussing tracer parameters, which are different from the chemical parameters obtained during electrical conductivity relaxation experiment. The switch of oxygen partial pressure during the ECR experiment is an external driving force pushing the sample to absorb or release oxygen, while during IEDP experiments the oxygen partial pressure in the surrounding is fixed.

If the concentration in a semi-infinite medium is initially c_{bg} throughout, and the surface exchange is determined by Eq. (2.30), then the solution is

$$c'(x,t) = \frac{c(x,t)-c_{bg}}{c_g-c_{bg}} = erfc\left[\frac{x}{2\sqrt{D^*t}}\right] -$$

$$-\left[exp\left(\frac{k^*x}{D^*}+\frac{k^{*2}t}{D^*}\right) \times erfc\left(\frac{x}{2\sqrt{D^*t}}+k^*\sqrt{\frac{t}{D^*}}\right)\right] \qquad \text{(Equation 2.31)}$$

where $c(x, t)$ is the ratio of concentration of ^{18}O to the total concentration of (^{18}O+^{16}O) in the material as measured by SIMS, x is the distance from the surface of the sample and t is the time of the isotope exchange, c_{bg} is the natural isotopic background of ^{18}O (0.21%), c_g is the isotope fraction of ^{18}O in the gas during the ^{18}O exchange.

Eq. (2.31) can be rewritten:

$$c'(x,t) = \frac{c(x,t)-c_{bg}}{c_g-c_{bg}} = erfc\left[\frac{x}{2\sqrt{D^*t}}\right] -$$

$$-\left[exp(hx + h^2D^*t) \times erfc\left(\frac{x}{2\sqrt{D^*t}} + h\sqrt{D^*t}\right)\right] \qquad \text{(Equation 2.32)}$$

where $h = \frac{k^*}{D^*}$.

For materials with an electronic transference number close to unity, the parameter h (cm^{-1}) in Eq. (2.32) is related to the characteristic thickness, l_d (cm), at which the oxygen surface exchange and diffusion through the material are equally important. Using Eq. (1.15) the relation between h and l_d can be written as:

$$l_d = \frac{D_O}{k} = \frac{fD^*}{k^*} \approx \frac{1}{h} \qquad \text{(Equation 2.33)}$$

where D_O is oxygen self-diffusion and f is the Haven ratio (Chapter 1.5.1.1).

2.3. Molecular dynamics

2.3.1. Introduction

With the increasing number of oxygen diffusion studies in perovskites, it became clear that investigation of diffusional transport mechanisms and defect chemistry is very important in understanding of macroscopic transport properties and in prediction of transport properties in perovskite materials. However, most diffusion experiments do not provide enough information to understand the atomistic mechanisms responsible for oxygen transport.

With the increasing computational power, computer modelling methods have become a recognized and well established tool for the investigation of defect chemistry. These techniques have been successfully applied to structural and defect studies at the microscopic level [39, 40].

Different simulation techniques are used for investigation of oxygen transport in bulk materials. Atomistic simulations use a static lattice configuration, and the lowest energy of the crystal lattice is determined during the experiment by energy minimization. These simulations are based on the interatomic potential model, which describes the total energy of the system as a function of the atomic coordinates. For oxide materials, the Born model is usually used which divides the total energy in long-range Coulombic (interactions), short-range Buckingham (repulsions) and van der Waals (attractions) parts:

$$\varphi_{ij}(r_{ij}) = A_{ij} \exp\left(-\frac{r_{ij}}{\rho_{ij}}\right) - \left(\frac{C_{ij}}{r_{ij}^6}\right) \qquad \text{(Equation 2.34)}$$

where r_{ij} is interionic distance, and parameters A_{ij}, ρ_{ij} and C_{ij} are parameters of the interactions.

The most important feature of these calculations is the treatment of the lattice relaxation about a point defect, so the crystal lattice is divided into two parts. Ions in a spherical inner part surrounding the defect are relaxed explicitly. In this case, local relaxation is well modelled and the system is not considered as a rigid lattice. This method is covered by the GULP simulation code [41].

The second approach in simulations is the molecular dynamic technique (MD). This is the dynamic simulations of the ensemble of the particles based on the Newton's equations of motion and provides a detailed information about the positions of the ions in the system and their velocities as a function of time. Information about the migration of the ions are extracted from the time-dependent mean square displacements (MSD):

$$\langle r_i^2(t)\rangle = \frac{1}{N}\sum_{i=1}^{N}[r_i(t) - r_i(0)]^2 \qquad \text{(Equation 2.35)}$$

where N is the total number of particles in the system, $r_i(t)$ is the position of ion i at time t, and $r_i(0)$ is its initial position.

This method provides a description of the migration of point defects in the system between equilibrium states, but works well only with fast diffusion processes due to the large amount of calculations that are required. MD calculations are usually conducted using DL_POLY code [42].

The last computational technique discussed here is based on the quantum mechanical (QM) or first-principles methods and attempt to solve Schrödinger equation for the system with some approximations. The QM method provides additional information on the electronic structure that cannot be obtained by atomistic simulations. However, this technique remains computationally expensive and has not been applied widely to study ionic transport in oxides.

2.3.2. Molecular dynamics background

Similar to static atomistic simulations, molecular dynamics simulations use Born-type description of the ionic crystal lattice:

$$E_L = \sum_{j>i} \sum \left[\frac{q_i q_j}{4\pi\varepsilon_0 r_{ij}} A_{ij} \exp\left(-\frac{r_{ij}}{\rho_{ij}}\right) - \left(\frac{C_{ij}}{r_{ij}^6}\right) \right] \qquad \text{(Equation 2.36)}$$

where r_{ij} is interionic distance, and parameters A_{ij}, ρ_{ij} and C_{ij} are parameters of interactions, q_i and q_j are charges of the ions i and j, respectively, and ε_0 is the permittivity of free space.

The calculated lattice energy is used to check how interaction parameters (A_{ij}, ρ_{ij}, and C_{ij}) fit the studied system by comparison of calculated properties (for example, unit-cell volume) with the experimental data (XRD studies).

Initial parameters, such as ions positions in the system, are usually obtained from X-ray powder diffraction (XRD) or neutron diffraction experiments.

Following Eq. (2.35) the oxygen self-diffusion coefficient can be obtained from the slopes of mean square displacements for specific temperature:

$$\langle |r_i(t) - r_i(0)|^2 \rangle = 6D_O t + B \qquad \text{(Equation 2.37)}$$

where D_O is oxygen self-diffusion, $|r_i(t) - r_i(0)|$ is the displacement of the ion *i* from its initial position and *B* is atomic displacement parameter attributed to thermal vibrations.

The main advantage of MD over other techniques is that transport properties of ions can be obtained by direct observation of ion trajectories. It also allows the investigation of the anisotropic character of diffusion in the system, which can also be studied by IEDP, but only on single crystals.

2.4. References

1. Riess, I. *The CRC Handbook of Solid Sate Electrochemistry*; Gellings, P. J.; Bouwmeester, H. J. M., Eds.; CRC press: Boca Raton, 1997; pp 223-231.

2. Morin, F.; Trudel, G. Oxygen diffusivity in strontium substituted lanthanum cobaltite. *Electrochem. Soc. Symp. Proc.* **1997**, *18*, 805-806.

3. Maier, J. Defect chemistry: Composition, transport, and reactions in the solid state; Part II: Kinetics. *Angew. Chem. Int. Ed. Engl*. **1993**, *32*, 528-542.

4. Elshof, J. E.; Lankhorst, M. H. R.; Bouwmeester, H. J. M. Oxygen exchange and diffusion coefficients of strontium-doped lanthanum ferrites by electrical conductivity relaxation. *J. Electrochem. Soc.* **1997**, *144*, 1060-1067.

5. Yasuda, I.; Hikita, T. Precise determination of the chemical diffusion coefficient of calcium-doped lanthanum chromites by means of electrical conductivity relaxation. *J. Electrochem. Soc.* **1994**, *141*, 1268-1273.

6. Song, C.-R.; Yoo, H.-I. Chemical diffusivity of $BaTiO_{3-\delta}$: I. Experimental determination. *Solid State Ionics* **1999**, *120*, 141-153.

7. Yasuda, I.; Hishinuma, M. Electrical conductivity and chemical diffusion coefficient of Sr-doped lanthanum chromites. *Solid State Ionics* **1995**, *80*, 141-150.

8. Yasuda, I.; Hishinuma, M. Chemical diffusion in polycrystalline calcium-doped lanthanum chromites. *J. Solid State Chem*. **1995**, *115*, 152-157.

9. Radecka, M.; Sobas, P.; Rekas, M. Ambipolar diffusion in TiO_2. *Solid State Ionics* **1999**, *119*, 55-60.

10. Price, J. B.; Wagner, J. B., Jr. Determination of the chemical diffusion coefficients in single crystals of CoO and NiO. *Z. Phys. Chem. Neue Folge* **1966**, *49*, 257-270.

11. Walters, L. C.; Grace, R. E. Diffusion of point defects in strontium titanate. *J. Phys. Chem. Solids* **1967**, *28*, 245-248.

12. Childs, P. E.; Laub, L. W.; Wagner, J. B. Jr., Chemical diffusion in nonstoichiometric compounds. *Proc. Br. Ceram. Soc.* **1971**, *19*, 29-53.

13. Kitazawa, K.; Coble, R. L. Chemical diffusion in polycrystalline Al_2O_3 as determined from electrical conductivity measurements. *J. Am. Ceram. Soc*. **1974**, *57*, 250-253.

14. Wernicke, R. The kinetics of equilibrium restoration in barium titanate ceramics. *Philips Res. Repts*. **1976**, *31*, 526-543.

15. Farhi, R.; Petot-Ervas, G. Electrical conductivity and chemical diffusion coefficient measurements in single crystalline nickel oxide at high temperatures. *J. Phys. Chem. Solids* **1978**, *39*, 1169-1173.

16. Morin, F.; Dieckmann, R. The determination of chemical diffusivity in cobaltous oxide by means of electrical conductivity. *Z. Phys. Chem. Neue Folge* **1982**, *129*, 219-223.

17. Yu, C. J.; Sparlin, D. M.; Anderson, H. U. Oxidation kinetics of polycrystalline $LaCrO_3$. *J. Am. Ceram. Soc*. **1987**, *70*, C189-192.

18. Park, J.; Kostic, P.; Singh, J. P. Electrical conductivity and chemical diffusion in sintered $YBa_2Cu_3O_y$. *Mater. Lett.* **1988**, *6*, 393-397.

19. Yasuda, I.; Hishinuma, M. Electrical conductivity and chemical diffusion coefficient of strontium-doped lanthanum manganites. *J. Solid State Chem.* **1996**, *123*, 382-390.

20. Franke, P.; Dieckmann, R. Nonstoichiometric compounds, advances in ceramics. In *American Ceramic Society*; Catlow, C. R. A.; Mackrodt, W. C., Eds.); Weaterville, OH, 1987; Vol. 23; p 27.

21. Kruidhof, H.; Bouwmeester, H. J. M.; Doom, R. H. E.; Burggraaf, A. J. Influence of order-disorder transitions on oxygen permeability through selected nonstoichiometric perovskite-type oxides. *Solid State Ionics* **1993**, *63-65*, 816-822.

22. Maier, J. On the correlation of macroscopic and microscopic rate constants in solid state chemistry. *Solid State Ionics* **1998**, *112*, 197-228.

23. Kim, S.; Yang, Y. L.; Jacobson, A. J.; Abeles, B. Diffusion and surface exchange coefficients in mixed ionic electronic conducting oxides from the pressure dependence of oxygen permeation. *Solid Sate Ionics* **1998**, *106*, 189-195.

24. De Souza, R. A.; Kilner, J. A. Oxygen transport in $La_{1-x}Sr_xMn_{1-y}Co_yO_{3\pm\delta}$ perovskites: Part I. Oxygen tracer diffusion. *Solid State Ionics* **1998**, *106*, 175-187.

25. Lankhorst, M. H. R.; Bouwmeester, H. J. M. Determination of oxygen nonstoichiometry and diffusivity in mixed conducting oxides by oxygen coulometric titration: I. Chemical diffusion in $La_{0.8}Sr_{0.2}CoO_{3-\delta}$. *J. Electrochem. Soc.* **1997**, *144*, 1261-1267.

26. Sunde, S.; Nisancioglu, K.; Giir, T. M. Critical analysis of potentiostatic step data for oxygen transport in electronically conducting perovskites. *J. Electrochem. Soc*. **1996**, *143*, 3497-3504.

27. Bouwmeester, H. J. M.; Burggraaf, A. J. *The CRC handbook of solid state electrochemistry*; Gellings, P. J.; Bouwmeester, H. J. M., Eds.; CRC press: Boca Raton, 1997; p 504.

28. Wang., S. Oxygen transport in mixed conducting perovskite oxides. PhD. Dissertation, University of Houston, 2000.

29. Opila, E.; Tuller, H. L.; Wuensch, B. J.; Maier, J. Oxygen tracer diffusion in $La_{2-x}Sr_xCuO_{4-y}$ single crystals. *J. Am. Ceram. Soc.* **1993**, *76*, 2363-2369.

30. Bassat, J. M.; Odier, P.; Villesuzanne, A.; Marin, C.; Pouchard, M. Anisotropic ionic transport properties in $La_2NiO_{4+\delta}$ single crystals. *Solid State Ionics* **2004**, *167*, 341-347.

31. Ruiz-Trejo E.; Sirman, J. D.; Baikov, Y. M.; Kilner, J. A. Oxygen ion diffusivity, surface exchange and ionic conductivity in single crystal Gadolinia doped Ceria. *Solid State Ionics* **1998**, *113*, 565-569.

32. Manning P. S.; Sirman, J. D.; DeSouza, R. A.; Kilner, J. A. The kinetics of oxygen transport in 9.5 mol % single crystal yttria stabilised zirconia. *Solid State Ionics* **1997**, *100*, 1-10.

33. Burriel M.; Garcia, G.; Santiso, J.; Kilner, J. A.; Chater, R. J.; Skinner, S. J. Anisotropic oxygen diffusion properties in epitaxial thin films of $La_2NiO_{4+\delta}$. *J. Mater. Chem.* **2008**, *18*, 416-422.

34. Sase M.; Hermes, F.; Yashiro, K.; Sato, K.; Mizusaki, J.; Kawada, T.; Sakai, N.; Yokokawa, H. Enhancement of oxygen surface exchange at the hetero-interface of $(La,Sr)CoO_3$ / $(La,Sr)_2CoO_4$ with PLD-layered films *J. Electrochem. Soc.* **2008**, *155*, B793-797.

35. Sase M.; Yashiro, K.; Sato, K.; Mizusaki, J.; Kawada, T.; Sakai, N.; Yamaji, K.; Horita, T.; Yokokawa, H. Enhancement of oxygen exchange at the hetero interface of $(La,Sr)CoO_3$ / $(La,Sr)_2CoO_4$ in composite ceramics. *Solid State Ionics* **2008**, *178*, 1843-1853.

36. Rupasov, D. P.; Berenov, A. V.; Kilner, J. A.; Istomin, S. Ya.; Antipov, E. V. Oxygen diffusion in $Sr_{0.75}Y_{0.25}CoO_{2.62}$. *Solid State Ionics* **2011**, *197*, 18-24.

37. Manning, P.; Sirman, J.; Kilner, J. Oxygen self-diffusion and surface exchange studies of oxide electrolytes having the fluorite structure. *Solid State Ionics* **1996**, *125*, 125-132.

38. Bredikhin, S. I.; Emel'chenko, G. A.; Shechtman, V. Sh.; Zhokhov, A. A.; Carter, S.; Chater, R. J.; Kilner J. A.; Steele, B. C. H. Anisotropy of oxygen self-diffusion in $YBa_2Cu_3O_{7-\delta}$ single crystals. *Physica C* **1991**, *179*, 286-290.

39. Catlow, C. R. A. Computer modelling in inorganic crystallography. In *Solid State Chemistry: Techniques*; Cheetham, A. K., Day, P., Eds.; Clarendon Press: Oxford, 1987.

40. Catlow, C. R. A.; Ackermann, L.; Bell, R. G.; Cora, F.; Gay, D. H.; Nygren, M. A.; Pereira, J. C.; Sastre, G.; Slater, B.; Sinclair, P. E. Computer modelling as a technique in solid state chemistry. *Faraday Discuss., R. Soc. Chem.* **1997**, *106*, 1-40.

41. Gale, J. D. GULP: A computer program for the symmetry-adapted simulation of solids. *J. Chem. Soc., Faraday Trans.* **1997**, *93*, 629-637.

42. Smith, W.; Forester, T.R. DL_poly_2.0: A general purpose parallel molecular dynamics simulation package. *J. Mol. Graphics* **1994**, *14*, 136-141.

Chapter 3. Oxygen diffusion in $Sr_3YCo_4O_{10.5}$

Chapters 3 is focused on the study of oxygen transport in perovskite-related compound $Sr_3YCo_4O_{10.5}$. Three different methods have been used: molecular dynamic simulations (Chapter 3a), isotope exchange depth profiling / secondary ion mass spectrometry (Chapter 3b) and electrical conductivity relaxation combined with thermogravimetric analysis (Chapter 3c). With the combination of all three techniques, oxygen self-diffusion, chemical oxygen diffusion and thermodynamic factors connecting these parameters have been obtained, as well as trajectories of oxygen diffusion in the crystal structure of $Sr_3YCo_4O_{10.5}$ have been predicted by molecular dynamic simulations. Results of these studies have been summarized in three papers:

Chapter 3a: Rupasov, D.; Chroneos, A.; Parfitt, D.; Kilner, J. A.; Grimes, R. W.; Istomin, S. Ya.; Antipov, E. V. Oxygen diffusion in $Sr_3YCo_4O_{10.5}$: A molecular dynamics study. *Phys. Rev. B* **2009**, *79*, 172102/1-172102/4.

Chapter 3b: Rupasov, D. P.; Berenov, A. V.; Kilner, J. A.; Istomin, S. Y.; Antipov, E. V. Oxygen diffusion in $Sr_3YCo_4O_{10.5}$. *Solid State Ionics* **2011**, *197*, 18-24.

Chapter 3c: Rupasov, D.; Makarenko, T.; Jacobson, A. J. Oxygen diffusion in $Sr_3YCo_4O_{10.5}$: An electrical conductivity relaxation and thermogravimetric analysis approach. *Submitted to Solid State Ionics,* **April 2014**. *Accepted,* **July 2014**.

Chapter 3a. Oxygen diffusion in $Sr_3YCo_4O_{10.5}$: A molecular dynamics study

3a.1. Abstract

Oxygen diffusion in $Sr_3YCo_4O_{10.5}$ is investigated using molecular dynamics simulations in conjunction with an established set of Born model potentials. We predict an activation energy of diffusion of 1.56 eV in the temperature range of 1000 – 1400 K. We observe extensive disordering of the oxygen ions over a subset of lattice sites. Furthermore, oxygen ion diffusion both in the *a*-*b* plane and along the *c* axis requires the same set of rate-limiting ion hops. It is predicted that oxygen transport in $Sr_3YCo_4O_{10.5}$ is therefore isotropic.

3a.2. Introduction

New solid-oxide fuel cell (SOFC) electrode materials must show improved performance at lower temperatures and resistance to degradation during operation. In that respect perovskite-related materials such as cobalt-based oxides are important candidate cathode materials for the next-generation SOFC because of their catalytic properties in addition to their high electronic and oxide conductivity. The structure and oxygen transport of the $Sr_{1-x}Ln_xCoO_{3-\delta}$ (Ln = rare-earth cations) complex cobalt oxides has been previously studied [1-8]. Cobalt oxides such as $Sr_{1-x}Y_xCoO_{3-\delta}$ are also potentially important as they can be used in dense membranes to separate oxygen from gas mixtures and because they exhibit a metal-insulator transition, a spin-state transition, and ferromagnetism [9-15].

A detailed knowledge of crystal structure and stoichiometry is essential in order to understand the mechanism of ionic diffusion. It was determined by Istomin *et al.*, using

synchrotron x-ray and neutron powder diffractions, that $Sr_{0.7}Y_{0.3}CoO_{2.62}$ exhibits the tetragonal symmetry (space group *I4/mmm*, No. 139) [14]. In this crystal structure the layers of CoO_6 octahedra alternate with oxygen-deficient layers that consist of O3, O4, and Co1 sites (Figure 3a.1.). Additionally, the O4 site was determined to have a partial occupancy of ¼ with only one of the four adjacent positions of O4 being occupied.

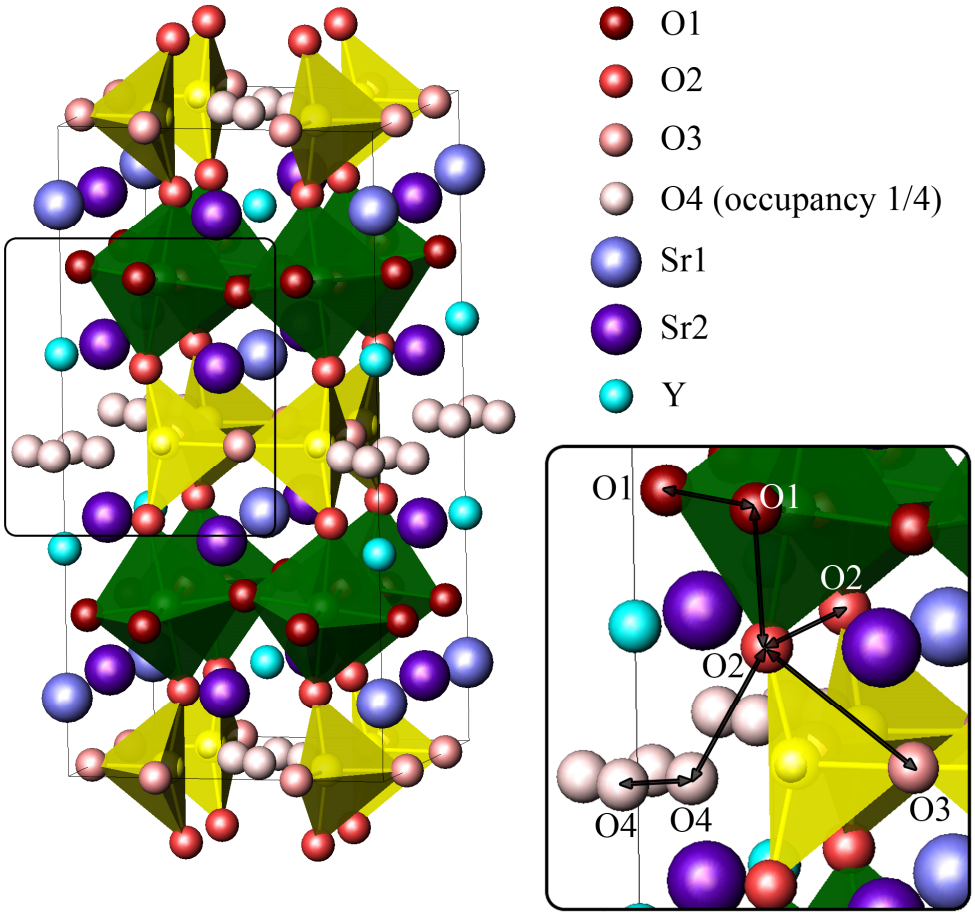

Figure 3a.1. In the crystal structure of $Sr_{0.7}Y_{0.3}CoO_{2.62}$ the $Co2O_6$ octahedra layers alternate with oxygen deficient layers that consist of O3, O4 (occupancy factor of ¼) and Co1 atoms.

Atomistic simulations can provide detailed information concerning the intrinsic disorder processes and diffusion mechanisms of inorganic materials [16-21]. The primary aim of the present study is to predict the oxygen-diffusion mechanism in $Sr_3YCo_4O_{10.5}$ (also known as the 314 phase) using classical molecular dynamics (MD) simulations.

3a.3. Experiment

MD simulations are essentially the iterative solution of Newton's equations of motion for an ensemble of particles. MD simulations require a potential-energy function that describes the forces between the ions. Here the classical Born-type description of the ionic crystal lattice is used [22]. In this, interactions between ions *i* and *j* are described by a long-range Coulombic (summed using Ewald's method [23]) and a short-range parametrized Buckingham pair potential, the latter summed to the cutoff value of 10.5 Å [24]. The lattice energy is given by

$$E_L = \sum_{j>i} \sum \left[\frac{q_i q_j}{4\pi\varepsilon_0 r_{ij}} A_{ij} \exp\left(-\frac{r_{ij}}{\rho_{ij}}\right) - \left(\frac{C_{ij}}{r_{ij}^6}\right) \right] \qquad \text{(Equation 3a.1)}$$

where r_{ij} is the interionic separation, q_i is the charge of ion *i*, ε_0 is the permittivity of free space, and A_{ij}, ρ_{ij}, and C_{ij} are the short-range parameters of the Buckingham pair potential (Table 3a.1). The short-range parameters used here were reported previously and their efficacy was established by comparing the predictions to experimental lattice properties [25-31]. For $Sr_3YCo_4O_{10.5}$ the predicted unit-cell volume is within 0.7% of the experimental volume [14].

Table 3a.1. Buckingham interionic potential parameters (Eq. (3a.1)).

Interaction	A_{ij} (eV)	ρ_{ij} (Å)	C_{ij} (eV·Å^6)	Reference
$O^{2-} - O^{2-}$	9547.96	0.2192	32.0	25
$Sr^{2+} - O^{2-}$	682.17	0.3945	0.0	26
$Y^{3+} - O^{2-}$	1766.40	0.33849	19.43	27
$Co^{3+} - O^{2-}$	1226.31	0.3087	0.0	28

The initial configurations for the present simulations are based on the structure of $Sr_3YCo_4O_{10.5}$ determined by Istomin *et al.* [14]. The infinite periodic crystal lattice is constructed from a supercell of 6 × 6 × 3 unit cells (containing 7992 ions), tessellated throughout space through the use of periodic boundary conditions, which are defined by the crystallographic lattice vectors. Newton's equations of motion were integrated using the velocity Verlet algorithm [32]. Ions were assigned a Gaussian distribution of velocities and with iterative velocity scaling, a stable temperature was achieved. The system was equilibrated for 5000 time steps (~ 5 ps) before carrying out the production runs that were used in the analysis. We used the variable time step option as implemented in the DL_POLY code for efficient sampling of the dynamic behavior [33, 34]. Typical time steps are on the order of 1 fs, and up to 250 000 time steps were used to investigate the diffusion processes in the temperature range of 500 – 1500 K. Simulations were run in the constant number of atoms-pressure-temperature (*NPT*) ensemble to predict the equilibrium lattice parameters and the constant number of atoms-volume-temperature (*NVT*) ensemble to

predict the diffusion properties. The temperature, and where necessary the pressure, was corrected with the use of the Nosé-Hoover thermostat [35, 36].

In the present MD simulations ionic transport was determined by monitoring the evolution of the mean-square displacement (MSD) of ions as a function of time for a range of defect temperatures. Extensive simulation times were used to consider a sufficient number of diffusion events for effective statistical sampling. The MSD of an ion *i* at a position $r_i(t)$ at time *t* with respect to its initial position $r_i(0)$ is defined by

$$\langle r_i^2(t)\rangle = \frac{1}{N}\sum_{i=1}^{N}[r_i(t) - r_i(0)]^2 \qquad \text{(Equation 3a.2)}$$

where *N* is the total number of ions in the system. All the cations considered (i.e., Sr, Y, and Co) oscillate around their equilibrium positions; above 900 K, however, oxygen ions demonstrate increasing MSD with time. This in turn indicates that oxygen self-diffusion is significant at high temperatures, whereas the cation self-diffusion is insignificant on the time scales considered.

3a.4. Results and discussion

The oxygen-diffusion coefficient D_O can be obtained directly from the slopes of MSD for a range of temperatures [37]

$$\langle |r_i(t) - r_i(0)|^2\rangle = 6D_O t + B \qquad \text{(Equation 3a.3)}$$

where $|r_i(t) - r_i(0)|$ is the displacement of an ion from its initial position and *B* is an atomic displacement parameter that can be attributed to thermal vibrations. Here we predict values for D_O over the range of temperatures 1000 – 1400 K and these are presented in the Arrhenius plot (Figure 3a.2).

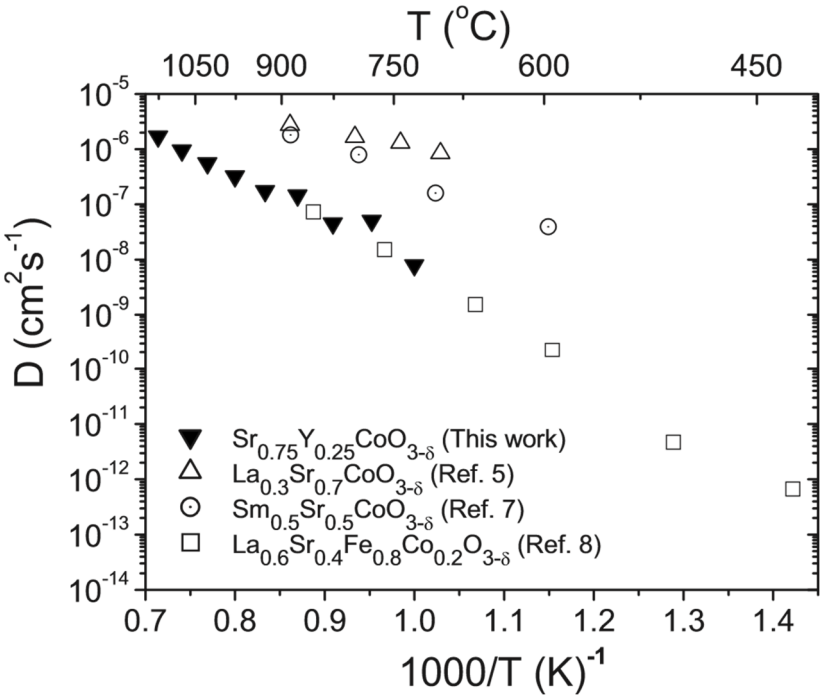

Figure 3a.2. Arrhenius plot of the calculated oxygen diffusivity in $Sr_3YCo_4O_{10.5}$. The present results are compared with the experimental results of van Doorn et al. [5], Fullarton et al. [7] and Benson et al. [8].

We find that over this temperature range, oxygen transport in $Sr_3YCo_4O_{10.5}$ can be described by the Arrhenius relation with an activation energy of 1.56 eV. At lower temperatures, we would expect a lower frequency of events that would necessitate simulation times that are beyond our computational resources. The energy required for an oxygen ion to migrate from an O4 site to an adjacent unoccupied O4 site is very small, about 0.1 eV. These events, however, do not lead to a net diffusion of the oxygen atoms.

Figure 3a.2 compares the present predicted values of oxygen-diffusion coefficient with previous experimental results from studies of related cobalt oxides such as $La_{0.3}Sr_{0.7}CoO_{3-\delta}$ (van Doorn *et al.* [5]), $Sm_{0.5}Sr_{0.5}CoO_{3-\delta}$ (Fullarton *et al.* [7]), and

$La_{0.6}Sr_{0.4}Fe_{0.8}Co_{0.2}O_{3-\delta}$ (Benson *et al.* [8]). Interestingly, in spite of their compositional differences, these observed diffusivities are in good agreement with the present predicted diffusivities.

A significant advantage of MD over other techniques is that it can reveal the transport mechanisms of atoms by the direct observation of ion trajectories and hence reveal any significant anisotropy. The calculated oxygen MSD in the *a* (or *b* as they are symmetrically equivalent) and *c* directions are surprisingly almost equal and therefore the transport of oxygen is predicted to be isotropic. Figures 3a.3(a) and 3a.3(b) represent an example of the oxygen-diffusion pathways on two (001) plane slices ($z = 0$ and $z = 0.25$) in $Sr_3YCo_4O_{10.5}$ at 1300 K.

At temperatures above 700 K, the oxygen ion at the O4 sites hops around the four equivalent sites (Figure 3a.3(a)), in excellent agreement with previous experimental neutron studies, as a result of the low activation energy for this process [14, 15]. At higher temperatures the thermal ellipsoid describing the O2 site becomes increasingly distorted along the [111] direction toward the neighboring partially occupied O4 sites (Figure 3a.3(c)). Additionally, at temperatures over 1000 K there is significant intermingling of the oxygen ions from O2 and O4 sites (Figure 3a.3(c)). Hopping analysis reveals the possibility of a distinct O5 site 0.35, 0.35 0.07 at high temperatures near O2 and this will be investigated further.

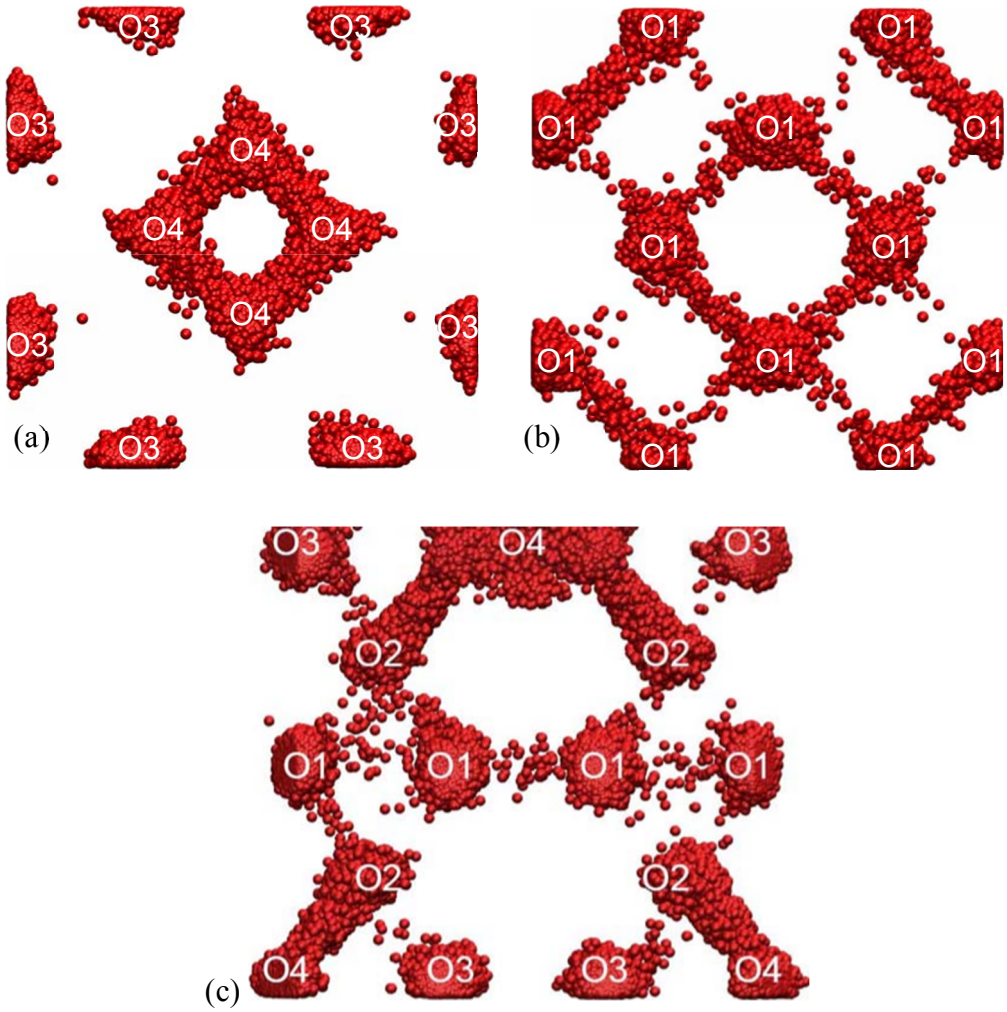

Figure 3a.3. Calculated oxygen density profiles in $Sr_3YCo_4O_{10.5}$ at 1300K along (a) the (001) plane at z = 0, (b) the (001) plane at z = 0.25 and (c) the (110) plane through the origin (half the unit cell), showing the diffusion pathways.

The disorder between the O2 and O4 sites does not provide the extended network of interconnected sites necessary for bulk oxygen diffusion. It does, however, provide a supply of oxygen vacancies at the O2 site. The dominant diffusion mechanism is the movement of these vacancies to the CoO1/O2 octahedra, which leads to migration in the

a-b plane through interconnected O1 sites at z = 0.25 and 0.75 (Figure 3.a3(b)) and migration along the *c* axis through the O2-O1-O2 pathway (inset in Figure 3a.1) and then into the highly disordered O4/O2 sites. As the barrier to exchange across the O4/O2 sites is very low, we suggest that transport along the *c* axis and in the *a-b* plane will be rate limited by the movement of oxygen vacancies around the Co-O1/O2 octahedra (note that analysis of oxygen-density profiles reveals that O2-O1 hops occur at almost the same rate as O1-O1 hops, leading to a migration probability and therefore diffusivity that is isotropic). Finally, it is predicted that the O3 ions do not effectively participate in the dominant oxygen-diffusion mechanism, although very limited exchange of O3 with O4 is observed at very high temperatures.

In the present study we have examined the migration of oxygen ions at elevated temperatures. The imposition of *NVT* conditions on the calculations is a necessary restriction but it does imply that the stoichiometry of the material does not change with temperature. This is an approximation, as in a thermogravimetric study of the related compound $Sr_{0.7}Y_{0.3}CoO_{2.62}$ it was observed that there is significant oxygen loss at around 673 K [14]. The introduction of oxygen vacancies is expected to lead to an increase in the diffusivity from the already significant levels calculated in this study, provided no extra defect interactions are introduced by the extra vacancies and the change in oxidation state of the Co cations.

3a.5. Conclusions

In summary, molecular dynamics simulations predict that oxygen transport in $Sr_3YCo_4O_{10.5}$ is isotropic with an activation energy of 1.56 eV in the temperature range of

1000 – 1400 K. The diffusion mechanism consists of O2 atoms moving to the partially occupied O4 sites creating vacancies at O2 sites. These vacancies move to the Co-O1/O2 octahedra (*a*-*b*-plane migration) and along the O2-O1-O2 pathway (*c*-axis migration). The effect of oxygen stoichiometry on the diffusion mechanism is currently under investigation.

3a.6. Acknowledgements

The authors thank Andrey Berenov for useful discussions. The work was supported by UKERC from NERC TSEC program under Grant No. NE/C513169/1. Computing resources were provided by the HPC facility of Imperial College London.

3a.7. References

1. Sunstrom, J.; Ramanujachary, K. V.; Greenblatt, M. The synthesis and properties of the chemically oxidized perovskite, $La_{1-x}Sr_xCoO_{3-\delta}$ ($0.5 \leq x \leq 0.9$). *J. Solid State Chem.* **1998**, *139*, 388-397.

2. Doorn, R. H. E.; Burggraaf, A. J. Structural aspects of the ionic conductivity of $La_{1-x}Sr_xCoO_{3-\delta}$. *Solid State Ionics* **2000**, *128*, 65-78.

3. Istomin, S. Ya.; Drozhzhin, O. A.; Svensson, G.; Antipov, E. V. Synthesis and characterization of $Sr_{1-x}Ln_xCoO_{3-\delta}$, Ln=Y, Sm–Tm, $0.1 \leqslant x \leqslant 0.5$. *Solid State Sci.* **2004**, *6*, 539-546.

4. Carter, S.; Selcuk, A.; Carter, R. J.; Kajda, J.; Kilner, J. A.; Steele, B. C. H. Oxygen transport in selected nonstoichiometric perovskite-structure oxides. *Solid State Ionics* **1992**, *53-56*, 597-605.

5. Doorn, R. H. E.; Fullarton, I. C.; De Souza, R. A.; Kilner, J. A.; Bouwmeester, H. J. M.; Burggraaf, A. J. Surface oxygen exchange of $La_{0.3}Sr_{0.7}CoO_{3-\delta}$. *Solid State Ionics* **1997**, *96*, 1-7.

6. Lane, J. A.; Benson, S. J.; Walter, D.; Kilner, J. A. Oxygen transport in $La_{0.6}Sr_{0.4}Co_{0.2}Fe_{0.8}O_{3-\delta}$. *Solid State Ionics* **1999**, *121*, 201-208.

7. Fullarton, I. C.; Kilner, J. A.; Steele, B. C. H.; Middleton, P. H. Characterization of oxygen ion transport in selected perovskite structured oxides by O^{18}/O^{16} isotopic exchange and dynamic secondary ion mass spectrometry. In *Proceedings of the 2rd International Symposium on Ionic and Mixed Conducting Ceramics*; The Electrochemical Society: Pennington, NJ, 1994; pp 9-24.

8. Benson, S. J.; Chater, R. J.; Kilner, J. A. Oxygen diffusion and surface exchange in the mixed conducting perovskite $La_{0.6}Sr_{0.4}Fe_{0.8}Co_{0.2}O_{3-d}$. In *Proceedings of the 3rd International Symposium on Ionic and Mixed Conducting Ceramics*; The Electrochemical Society: Pennington, NJ, 1997; pp 596-609.

9. Goossens, D. J.; Wilson, K. F.; James, M.; Studer, A. J.; Wang, X. L. Structural and magnetic properties of $Y_{0.33}Sr_{0.67}CoO_{2.79}$. *Phys. Rev. B* **2004**, *69*, 134411/1-134411/6.

10. Kobayashi, W.; Ishiwata, S.; Terasaki, I.; Takano, M.; Grigoraviciute, I.; Yamaguchi, H.; Karppinen, M. Room-temperature ferromagnetism in $Sr_{1-x}Y_xCoO_{3-\delta}$ ($0.2 \leqslant x \leqslant 0.25$). *Phys. Rev. B* **2005**, *72*, 104408/1-104408/5.

11. Antipov, E. V.; Abakumov, A. M.; Istomin, S. Ya. Target-aimed synthesis of anion-deficient perovskites. *Inorg. Chem.* **2008**, *47*, 8543-8552.

12. Kimura, S.; Maeda, Y.; Kashiwagi, T.; Yamaguchi, H.; Hagiwara, M.; Yoshida, S.; Terasaki, I.; Kindo, K. Field-induced spin-state transition in the perovskite cobalt oxide $Sr_{1-x}Y_xCoO_{3-\delta}$. *Phys. Rev. B* **2008**, *78*, 180403/1-180403/4.

13. Istomin, S. Ya.; Drozhzhin, O. A.; Napolsky, Ph. S.; Putilin, S. N.; Gippius, A. A.; Antipov, E. V. Thermal expansion behavior and high-temperature transport properties of $Sr_3YCo_{4-x}Fe_xO_{10.5+y}$, x = 0.0, 1.0, 2.0 and 3.0. *Solid State Ionics* **2008**, *179*, 1054-1057.

14. Istomin, S. Y.; Grins, J.; Svensson, G.; Drozhzhin, O. A.; Kozhevnikov, V. L.; Antipov, E. V.; Attfield, J. P. Crystal structure of the novel complex cobalt oxide $Sr_{0.7}Y_{0.3}CoO_{2.62}$. *Chem. Mater.* **2003**, *15*, 4012-4020.

15. Lindberg, F.; Drozhzhin, O. A.; Istomin, S. Y.; Svensson, G.; Kaynak, F. B.; Svedlindh, P.; Warnicke, P.; Wannberg, A.; Mellergard, A.; Antipov, E. V. Synthesis and characterization of $Sr_{0.75}Y_{0.25}Co_{1-x}M_xO_{2.625+\delta}$ (M = Ga, $0.125 \leqslant x \leqslant 0.500$ and M = Fe, $0.125 \leqslant x \leqslant 0.875$). *J. Solid State Chem.* **2006**, *179*, 1434-1444.

16. Parfitt, D. C.; Keen, D. A.; Hull, S.; Crichton, W. A.; Mezouar, M.; Wislon, M.; Madden, P. A. High-pressure forms of lithium sulphate: Structural determination and computer simulation. *Phys. Rev. B* **2005**, *72*, 054121/1-054121/7.

17. Cleave, A. R.; Kilner, J. A.; Skinner, S. J.; Murphy, S. T.; Grimes, R. W. Atomistic computer simulation of oxygen ion conduction mechanisms in La_2NiO_4. *Solid State Ionics* **2008**, *179*, 823-826.

18. Chroneos, A.; Grimes, R. W.; Uberuaga, B. P.; Bracht, H. Diffusion and defect reactions between donors, C, and vacancies in Ge. II. Atomistic calculations of related complexes. *Phys. Rev. B* **2008**, *77*, 235208/1-235208/7.

19. Posselt, M.; Gao, F.; Bracht, H. Correlation between self-diffusion in Si and the migration mechanisms of vacancies and self-interstitials: An atomistic study. *Phys. Rev. B* **2008**, *78*, 035208/1-035208/9.

20. Chroneos, A.; Bracht, H.; Jiang, C.; Uberuaga, B. P.; Grimes, R. W. Nonlinear stability of E centers in $Si_{1-x}Ge_x$: Electronic structure calculations. *Phys. Rev. B* **2008**, *78*, 195201/1-195201/7.

21. Chroneos, A.; Bracht, H.; Jiang, C.; Grimes, R. W.; Uberuaga, B. P. Vacancy-mediated dopant diffusion activation enthalpies for germanium. *Appl. Phys. Lett.* **2008**, *92*, 172103/1-172103/3.

22. Born M.; Mayer, J. E. Zur gittertheorie der ionenkristalle. *Z. Phys.* **1932**, *75*, 1-18.

23. Ewald, P. P. Die Berechnung optischer und elektrostatischer gitterpotentiale. *Ann Phys.* **1921**, *64*, 253-287.

24. Buckingham, R. A. The classical equation of state of gaseous helium, neon and argon. *Proc. Royal Soc. London Series A, Math. Phys. Sci.* **1938**, *168*, 264-283.

25. Grimes, R. W.; Binks, D. J.; Lidiard, A. B. The extent of zinc oxide solution in zinc chromate spinel. *Philos. Mag.* **1995**, *A72*, 651-654.

26. McCoy, M. A.; Grimes, R. W.; Lee, W. E. Phase stability and interfacial structures in the SrO–$SrTiO_3$ system. *Philos. Mag.* **1997**, *A75*, 833-846.

27. Grimes, R. W.; Busker, G.; McCoy, M. A.; Chroneos, A.; Kilner, J. A.; Chen, S. P. The effect of ion size on solution mechanism and defect cluster geometry. *Ber. Bunsen. Ges. Phys. Chem.* **1997**, *101*, 1204-1210.

28. Binks, D. J. Computational modelling of zinc oxide and related oxide ceramics. PhD. Dissertation, University of Surrey, 1994.

29. Busker, G.; Chroneos, A.; Grimes, R. W.; Chen, I. W. Solution mechanisms for dopant oxides in yttria. *J. Am. Ceram. Soc.* **1999**, *82*, 1553-1559.

30. Minervini, L.; Grimes, R. W.; Kilner, J. A.; Sickafus, K. E. Oxygen migration in $La_2NiO_{4+\delta}$. *J. Mater. Chem.* **2000**, *10*, 2349-2354.

31. Levy, M. R.; Stanek, C. R.; Chroneos, A.; Grimes, R. W. Defect chemistry of doped bixbyite oxides. *Solid State Sci.* **2007**, *9*, 588-593.

32. Swope, W. C.; Andersen, H. C.; Berens, P. H.; Wilson, K. R. A computer simulation method for the calculation of equilibrium constants for the formation of physical clusters of molecules: Application to small water clusters. *J. Chem. Phys.* **1982**, *76*, 637-649.

33. Smith, W.; Forester, T.R. DL_POLY_2.0: A general-purpose parallel molecular dynamics simulation package. *J. Mol. Graphics* **1996**, *14*, 136-141.

34. Smith, W.; Todorov, I. The DLPOLY 3.0 user manual, Daresbury Laboratory, UK, **2008**.

35. Nose, S. A unified formulation of the constant temperature molecular dynamics methods. *J. Chem. Phys.* **1984**, *81*, 511-517.

36. Hoover, W. G. Canonical dynamics: Equilibrium phase-space distributions. *Phys. Rev.* **1985**, *A31*, 1695-1697.

37. Gillan, M. J.; The simulation of superionic materials. *Physica* **1985**, *131B*, 157-174.

Chapter 3b. Oxygen diffusion in $Sr_3YCo_4O_{10.5}$: Isotope exchange depth profiling / secondary ion mass spectrometry approach

3b.1. Abstract

Oxygen tracer diffusion in polycrystalline samples of $Sr_3YCo_4O_{10.5}$ (SYC) was studied by isotope exchange depth profile and secondary ion mass spectrometry (IEDP/SIMS). The values of the tracer diffusion coefficient, D^*, and the surface exchange coefficient, k^*, were measured as a function of temperature (500 – 900 °C). We observed an Arrhenius behavior, $A = A_0 \exp(-\frac{E_A}{kT})$, with the activation energies of $E_A^D = 1.58 \pm 0.05$ eV and $E_A^k = 1.79 \pm 0.27$ eV for D^* and k^*, respectively. Electrochemical performance of symmetrical cells with $Ce_{0.9}Gd_{0.1}O_{1.95}$ (GDC) as electrolyte (SYC/GDC/SYC) in the temperature range 620 – 770 °C has been evaluated. An area-specific resistance (ASR) of 0.17 Ωcm^2 was measured at 720 °C.

3b.2. Introduction

The reduction of the operating temperature of intermediate-temperature solid oxide fuel cells (IT-SOFC) to lower temperatures (500 – 700 °C) significantly restricts the selection of cathode materials in terms of their electrical conductivity and oxygen transport. For example, the integration of $La_{1-x}Sr_xMnO_3$ perovskites as cathodes at intermediate temperatures leads to a dramatic increase in overpotential resistance thus reducing cell performance [1]. Two approaches have been suggested in order to improve cathode

performance at low temperatures. The first one is the utilization of composite cathodes consisting of two phases, one with high electronic conductivity and the other with high oxygen-ion conductivity [2]. The second approach is the development of cathodes with mixed oxygen ionic and electronic conductivity (MIEC). MIEC cathodes exhibit enhanced activity by allowing the cathode reaction to proceed over a significantly larger surface area of the mixed ionic and electronic cathode rather than being confined to the triple phase boundary (TPB). For example, the MIEC perovskite: $La_{1-x}Sr_xCo_{1-y}Fe_yO_{3-d}$ has demonstrated acceptable cathode performance at 650 °C [3] presumably due to the fast oxygen surface exchange kinetics and bulk oxygen diffusivity resulting in an increased active area of the cathode reaction.

Recently, the perovskite-related $Sr_3YCo_4O_{10.5}$ (314-phase) has been described in the literature [4] (Figure 3b.1). The authors found that the material has a previously unreported type of oxygen vacancy ordering resulting in a tetragonal perovskite-related structure with $a \approx 2 \times a_p$ and $c \approx 4 \times a_p$. In the 314-phase oxygen tetrahedra form tetracyclic units with one additional oxygen atom per layer instead of the infinite chains of tetrahedra observed in the brownmillerite structure.

Molecular dynamics (MD) calculations of oxygen diffusion in $Sr_3YCo_4O_{10.5}$ predicted that the oxygen transport in $Sr_3YCo_4O_{10.5}$ is isotropic with an activation energy of 1.56(7) eV in the temperature range 727 – 1127 °C [5].

In the current work the parameters of oxygen transport in $Sr_3YCo_4O_{10.5}$, namely the oxygen tracer diffusion coefficient, D^*, and the oxygen surface exchange coefficient, k^*, were determined by ion exchange depth profile technique (IEDP) followed by the analysis of the induced ^{18}O diffusion profiles by secondary ion mass spectrometry (SIMS).

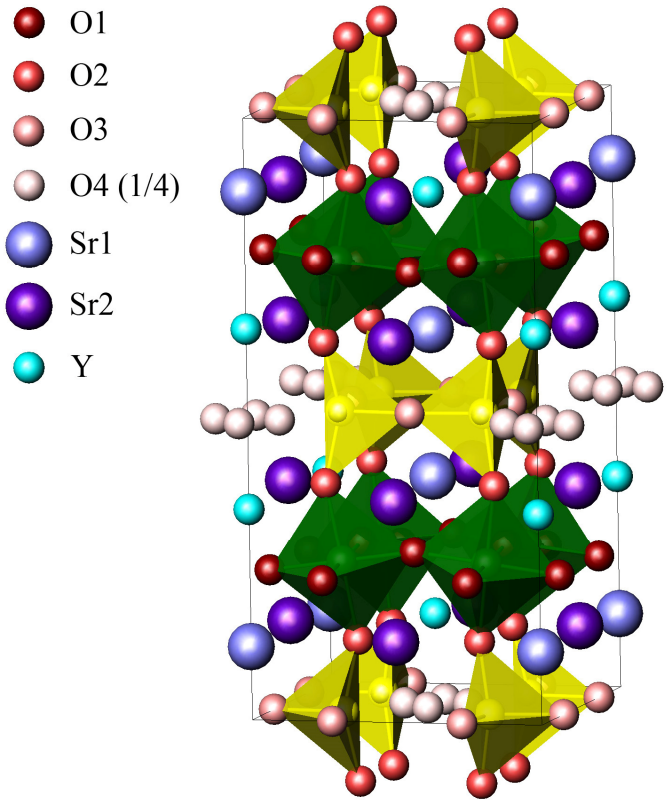

Figure 3b.1. The crystal structure of $Sr_3YCo_4O_{10.5}$ showing alternating octahedral CoO_6 and tetragonal CoO_4 layers. The O4 site has a partial occupancy of 0.25.

3b.3. Experimental

$Sr_3YCo_4O_{10.5}$ powder was synthesized by the citrate method. Stoichiometric amounts of $SrCO_3$ (Aldrich, 99.9%), Y_2O_3 (Aldrich, 99.99%), and $Co(NO_3)_2 \cdot 6H_2O$ (Aldrich, 99%) were dissolved in nitric acid under intensive stirring. The citric acid was added to the solution in a molar ratio 1.15:1 for citric acid:total metal ions. The solution was evaporated on a hot plate and the organic residue was decomposed at 500 ºC overnight followed by regrinding. The resulting powder was annealed 1150 ºC for 48 hours to obtain a single phase compound.

The crystal structure and phase purity of the $Sr_3YCo_4O_{10.5}$ powder were analyzed by XRD (Philips, 1710 type diffractometer) using Cu-Kα radiation (Figure 3b.2). The structural parameters were refined by the Rietveld method [6] using the FullProf computer program and the structural model provided by Istomin *et al.* [4]. The unit cell parameters were in good agreement with the ones previously reported in the literature [4].

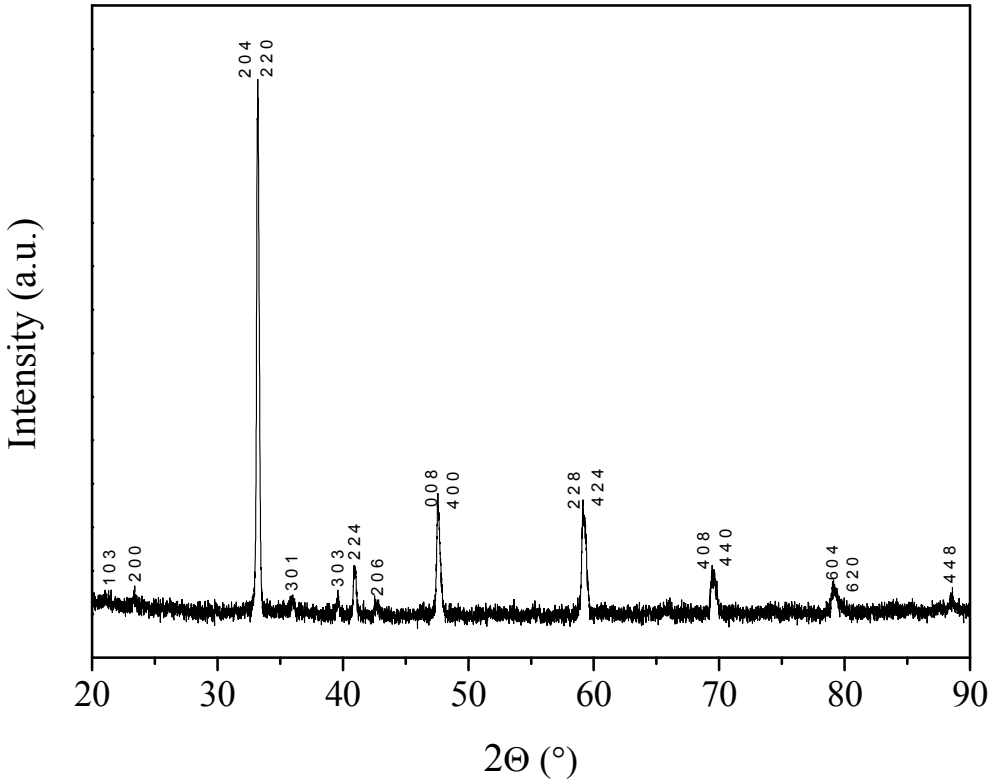

Figure 3b.2. XRD pattern of $Sr_3YCo_4O_{10.5}$ powder annealed in air at 1150 ºC for 48 hours.

The powder was milled with zirconia balls in ethanol for 2 days. The powder was isostatically pressed at 300 MPa into 13 mm diameter pellets and subsequently sintered at 1150 ºC for 4 hours in air. The density of the pellets, as measured by the Archimedes

technique, was greater than 95%. The average grain size, as measured by the linear intercept method, was 5 μm. The pellets were polished down to 0.25 μm finish using diamond compounds and each pellet was cut into four pieces with a surface area of around 20 mm^2 and a thickness of around 2.6 mm.

Before the ^{18}O exchange anneals, the $Sr_3YCo_4O_{10.5}$ specimens were pre-annealed in research grade oxygen (99.9995%) of normal isotopic abundance at $p(O_2) = 0.21$ bar for at least 10 times longer than the consequent isotope exchanges and quenched to room temperature. This step was necessary to ensure that the specimens were at equilibrium at the exchange temperature and oxygen partial pressure. The isotopic fraction of ^{18}O in the gas phase (c_g = 0.2936) during the exchange was determined by the oxidation of silicon at 1100 °C followed by SIMS analysis. The samples were rapidly heated to the annealing temperature and quenched to room temperature after the exchange. The temperature was monitored by Pt-Pt/Rh thermocouple positioned near the sample and the recorded temperature profiles were used to correct the annealing times by taking into account oxygen diffusion during sample heating and cooling [7, 8]. Two different analysis techniques were used depending upon the diffusion depth. Depth profiling (Figure 3b.3(a)) was used for the samples with a diffusion depth of up to 15 microns (annealing temperatures of 500 – 600 ºC) whereas, line scanning (Figure 3b.3(b)) was employed for the samples with diffusion depths greater than 50 micron (annealing temperatures of 700 – 900 ºC).

Depth profiling was performed using a focused ion beam instrument (FIB-200, FEI [9]) equipped with a quadrupole SIMS attachment using a 30 keV Ga^+ primary beam at normal incidence across a 10 x 10 μm^2 area and recording the intensities of secondary

negative ions with m/z ratios of 16 ($^{16}O^-$), 18 ($^{18}O^-$) as a function of sputtering time. Several depth profiles were performed using an Atomika 6500 UHV-SIMS instrument by rastering a 5 keV N_2^+ primary beam at normal incidence across 150 x 150 μm^2 area and recording the intensities of secondary negative ions with m/z ratios of 16 ($^{16}O^-$), 18 ($^{18}O^-$) as a function of sputtering time. The depths of the sputtered craters were measured by a surface profilometer (New View 200, Zygo) using optical interferometry. The intensity of secondary ions ($^{16}O^-$ and $^{18}O^-$) as a function of sputtering time was converted into the intensity of secondary ions as a function of depth assuming a constant sputtering rate.

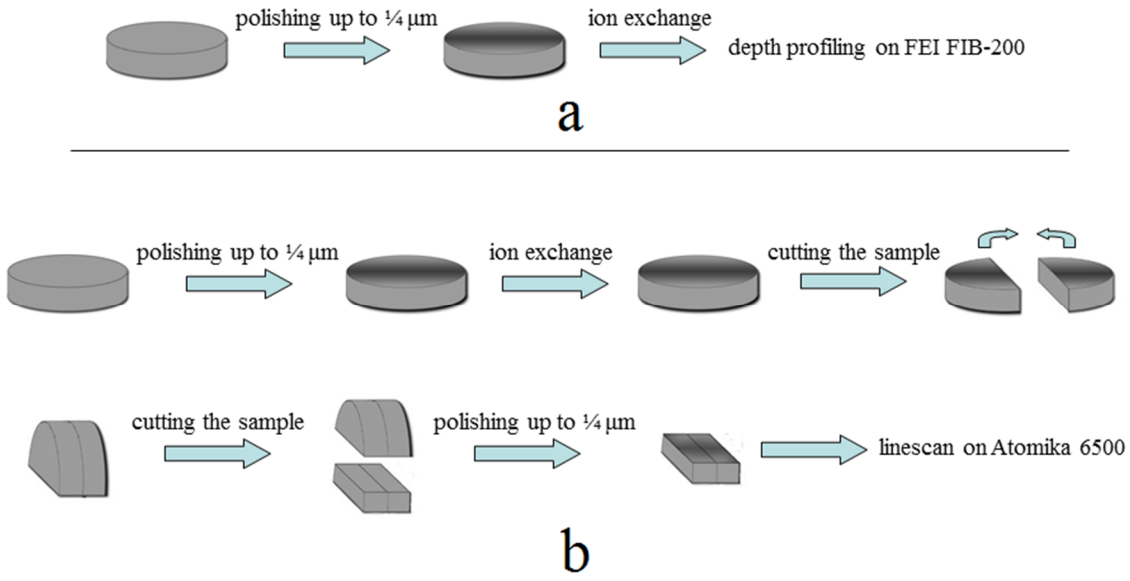

Figure 3b.3. Sample preparation for depth profiling (a) and line scanning (b) measurements.

In the line scanning technique, the ^{18}O annealed sample was cut perpendicular to the original surface of the ^{18}O exchange, polished and analyzed by SIMS along the cut

surface. The intensity of secondary negative ions with m/z ratios of 16 ($^{16}O^-$) and 18 ($^{18}O^-$) were measured by an Atomika 6500 UHV-SIMS instrument. A 5 keV Ar^+ primary beam with diameter of 18 μm was used for the line scanning.

The observed diffusion lengths were significantly smaller than the sample dimensions, therefore 1D diffusion perpendicular to the sample surface into a semi-infinite medium was considered. The solution to the Fick's diffusion equation under the conditions of our experiments: first order surface exchange reaction and constant ^{18}O concentration during the exchanges, is given by the following equation [10]:

$$c'(x,t) = \frac{c(x,t)-c_{bg}}{c_g-c_{bg}} = erfc\left[\frac{x}{2\sqrt{D^*t}}\right] -$$

$$-\left[exp\left(\frac{k^*x}{D^*}+\frac{k^{*2}t}{D^*}\right)\times erfc\left(\frac{x}{2\sqrt{D^*t}}+k^*\sqrt{\frac{t}{D^*}}\right)\right] \qquad \text{(Equation 3b.1)}$$

where $c(x, t)$ is the ratio of intensity of ^{18}O signal to the total intensity of (^{18}O+^{16}O) in the material as measured by SIMS, x is the distance from the surface of the specimen and t is the time of the isotope exchange, c_{bg} is the natural isotopic background of ^{18}O (0.21 %), c_g is the isotope fraction of ^{18}O in the gas during the ^{18}O exchange, D^* is the bulk oxygen tracer diffusion coefficient, and k^* is the surface exchange coefficient. Values of D^* and k^* were obtained by fitting the experimental data to the Eq. (3b.1) using a non-linear least square regression (Matlab 7.0, MathWorks).

The reactivity of $Sr_3YCo_4O_{10.5}$ with $Ce_{0.9}Gd_{0.1}O_{1.95}$ was investigated by mixing and grinding two powders in a 50/50 weight ratio and annealing at 900 °C for 140 hrs and 1120 °C for 2 hrs.

The cathode performance of $Sr_3YCo_4O_{10.5}$ was studied on symmetrical cells ($Sr_3YCo_4O_{10.5}$ / $Ce_{0.9}Gd_{0.1}O_{1.95}$ / $Sr_3YCo_4O_{10.5}$). 13 mm diameter and 1.5 mm thick $Ce_{0.9}Gd_{0.1}O_{1.95}$ (GDC) pellets were made by isostatically pressing commercial $Ce_{0.9}Gd_{0.1}O_{1.95}$ powder (Aldrich) at 300 MPa and sintering at 1450 ºC for 2 hours. The relative density of the GDC pellets was greater than 95%. Two techniques were used for the deposition of the $Sr_3YCo_4O_{10.5}$ cathode layers. The original $Sr_3YCo_4O_{10.5}$ powder was ball milled in ethanol for several days, this suspension was sprayed on both surfaces of the $Ce_{0.9}Gd_{0.1}O_{1.95}$ pellets and sintered within the temperature range 900 – 1120 ºC for 2 – 4 hours. In another technique, the mixture of $Sr_3YCo_4O_{10.5}$ powder and an organic vehicle (Fuel Cell Materials) was ball milled for several days and screen printed on both sides of $Ce_{0.9}Gd_{0.1}O_{1.95}$ pellets. The thickness of the prepared cathode layers was 10 – 20 μm as observed by scanning electron microscopy (SEM).

Pt grids (8 mm diameter) were used during 2-probe symmetrical AC Impedance measurements to ensure good quality contacts. The electrical measurements were carried out in stagnant air under open circuit voltage condition using a Solartron 1260 frequency response analyzer (10 mHz – 10 MHz, ac applied signal 50mV). Only the impedance data obtained at frequencies below than 100 kHz were used in the analysis because of large errors quoted for low resistance samples measured at frequencies higher than 1 MHz [11]. Origin program (OriginLab, Northampton, USA) was used for the non-linear fitting of complex impedances.

3b.4. Results and discussion

Typical ^{18}O isotopic diffusion profiles measured by depth profiling and line scanning techniques are shown in Figure 3b.4(a) and Figure 3b.4(b), respectively. Reproducible values of ^{18}O fraction were measured by both the FIB-200 and the Atomika 6500 instruments on the specimen annealed at 550 °C (Figure 3b.4(a)). A good agreement between the experimental data and the fit to the Eq. (3b.1) was observed at all temperatures studied.

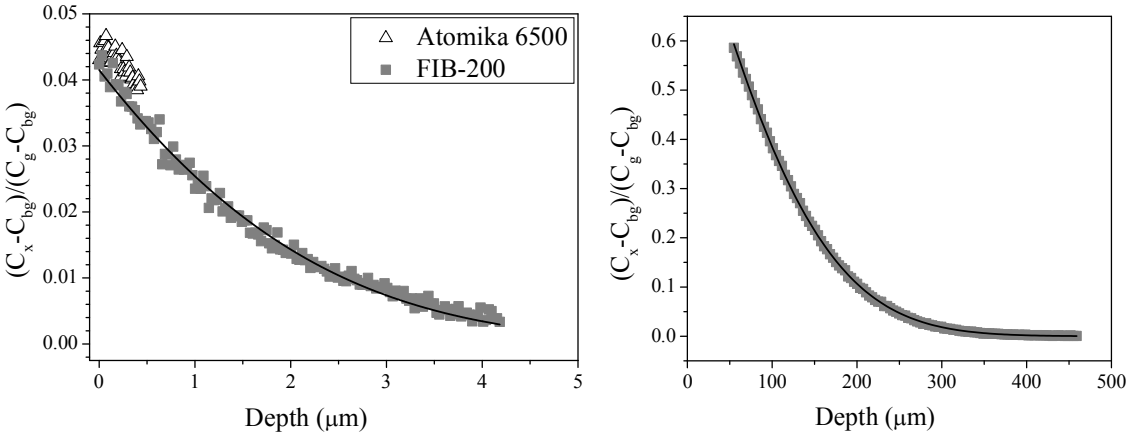

(a) (b)

Figure 3b.4. Normalized ^{18}O diffusion profiles as measured by depth profiling (a) on a sample annealed at 550 ºC for 20 min and line scanning (b) on a sample annealed at 800 ºC for 150 min. Solid lines represent the fit to the diffusion Eq. (3b.1).

The surface fraction of ^{18}O was more than one order of magnitude greater than the natural background abundance in all samples studied thus confirming that reliable values of D^* and k^* were obtained. Figure 3b.5 shows the typical dimensions of the craters sputtered by the FIB instrument. The parameters of oxygen diffusion, the tracer diffusion

coefficient D^* and surface exchange coefficient k^*, for $Sr_3YCo_4O_{10.5}$ are given in Table 3b.1.

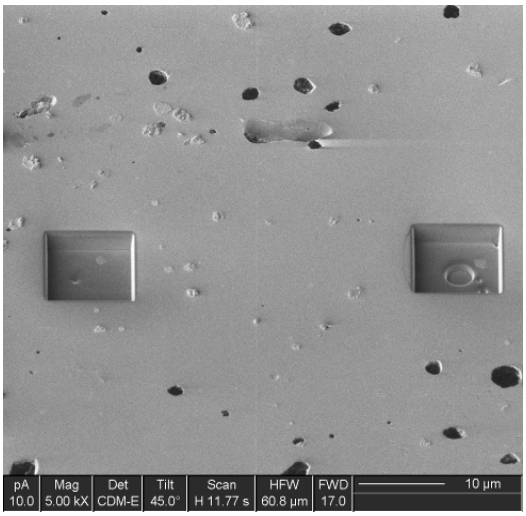

Figure 3b.5. Surface morphology of the $Sr_3YCo_4O_{10.5}$ pellet after isotope exchange at 600 ºC and depth profiling. The rectangles were formed during sputtering in the FIB instrument; the black spots are defects of the surface.

Table 3b.1. Parameters of oxygen diffusion in $Sr_3YCo_4O_{10.5}$.

Temperature and duration of ^{18}O exchange	D^* ($cm^2\ s^{-1}$)	k^* ($cm\ s^{-1}$)	$2(D^*t)^{½}$ (µm)	*Analysis mode*
500 ºC, 35 min	$(1.20 \pm 0.20) \times 10^{-11}$	$(3.45 \pm 0.27) \times 10^{-8}$	3.17	Depth profiling by FIB-200
550 ºC, 34 min	$(5.57 \pm 0.47) \times 10^{-11}$	$(8.44 \pm 0.59) \times 10^{-9}$	6.77	Depth profiling by FIB-200 and Atomika 6500
600 ºC, 10 min	$(1.38 \pm 0.11) \times 10^{-10}$	$(1.85 \pm 0.54) \times 10^{-7}$	5.99	Depth profiling by FIB-200
700 ºC, 450 min	$(1.89 \pm 0.52) \times 10^{-9}$	$(6.06 \pm 0.12) \times 10^{-6}$	142.87	Line scanning by Atomika 6500
800 ºC, 135 min	$(1.03 \pm 0.01) \times 10^{-8}$	$(1.62 \pm 1.00) \times 10^{-5}$	182.43	Line scanning by Atomika 6500
900 ºC, 12 min	$(3.27 \pm 0.07) \times 10^{-8}$	$(8.55 \pm 1.28) \times 10^{-5}$	95.68	Line scanning by Atomika 6500

The oxygen diffusion coefficients D^* and surface exchange coefficients k^* are plotted as a function of reciprocal temperature in Figure 3b.6. Both of them show Arrhenius-type behavior, $A = A_0 \exp(-\frac{E_A}{kT})$, with activation energies of E_A^D = 1.58 ± 0.05 eV and E_A^k = 1.79 ± 0.27 eV for D^* and k^*, respectively. A higher degree of scatter of k^* values from the straight line fit can be explained by the presence of small pores and/or surface defects as seen in Figure 3b.5.

The observed values of the oxygen tracer diffusion coefficient agree reasonably well (Figure 3b.6(a)) with the values obtained in our previous molecular dynamic (MD) modeling study of oxygen diffusion in $Sr_3YCo_4O_{10.5}$ [5].

The activation energy for oxygen diffusion, as calculated by MD, was 1.56(7) eV [5], which is very close to the value obtained experimentally in this work by IEDP/SIMS technique. The polycrystalline nature of the specimens precluded us from studying the possible effect of the anisotropy on the oxygen diffusion in $Sr_3YCo_4O_{10.5}$ as has been previously suggested [5].

The observed values of D^* in $Sr_3YCo_4O_{10.5}$ are comparable with those reported for $La_{0.6}Sr_{0.4}Fe_{0.8}Co_{0.2}O_{3-x}$ [3] and about two orders of magnitude lower than those reported for $Sm_{0.5}Sr_{0.5}CoO_{3-x}$ [12]. Interestingly, the values of surface exchange coefficient and the corresponding activation energy are comparable to those reported for $La_{0.6}Sr_{0.4}Fe_{0.8}Co_{0.2}O_{3-x}$ [3], $Sm_{0.5}Sr_{0.5}CoO_{3-x}$ [12] and $La_{0.3}Sr_{0.7}CoO_{3-x}$ [13] suggesting a similar mechanism of surface exchange in Co containing perovskites.

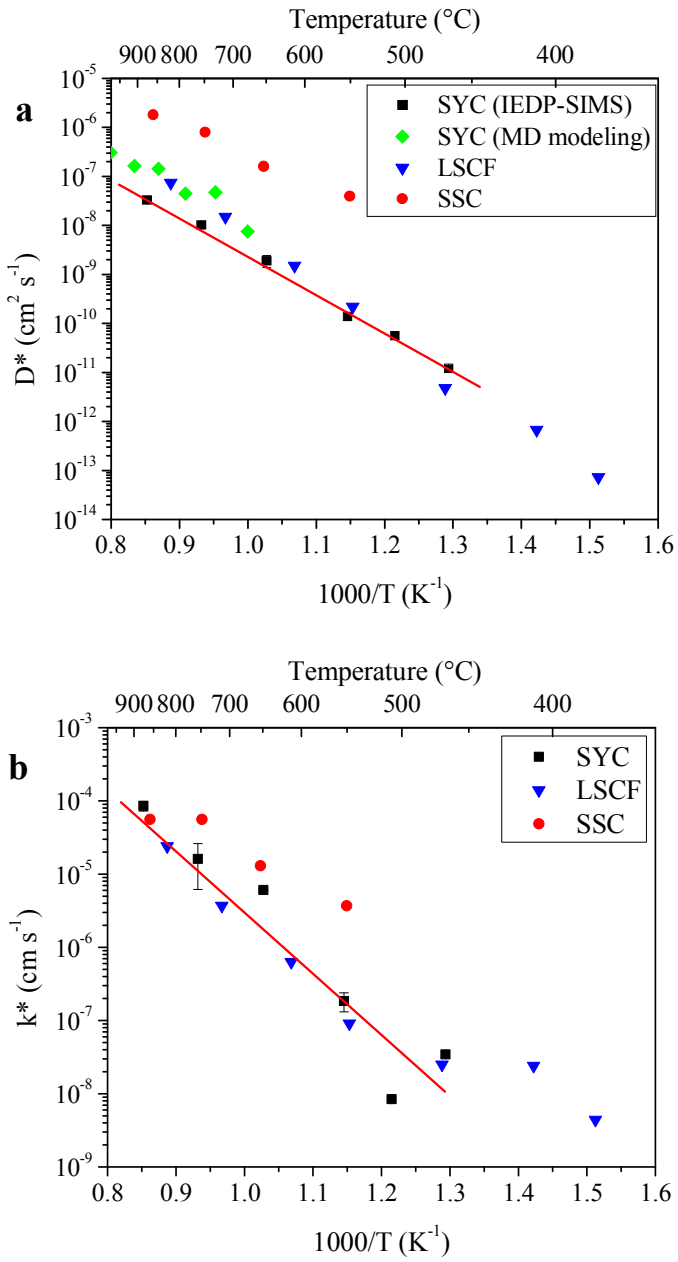

Figure 3b.6. Arrhenius plots of the oxygen diffusion coefficients (a) and surface exchange coefficients (b) obtained by IEDP-SIMS and calculated by MD modeling [5] for $Sr_3YCo_4O_{10.5}$. Literature data for $La_{0.6}Sr_{0.4}Fe_{0.8}Co_{0.2}O_{3-x}$ (LSCF, [3]) and $Sm_{0.5}Sr_{0.5}CoO_{3-x}$ (SSC, [12]) are shown for comparison.

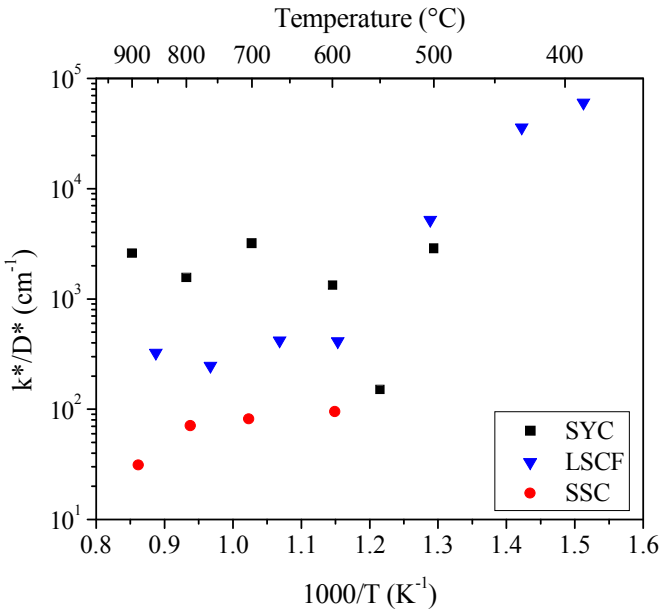

Figure 3b.7. k^*/D^* as a function of the reciprocal temperature for $Sr_3YCo_4O_{10.5}$ (this work), $La_{0.6}Sr_{0.4}Fe_{0.8}Co_{0.2}O_{3-x}$ [3] and $Sm_{0.5}Sr_{0.5}CoO_{3-x}$ [12].

Fast oxygen diffusion in a MIEC material results in the migration of oxygen ions through the bulk of the cathode in addition to TPB thus significantly increasing the active area of the cathode and lowering the polarization resistance. In the present work, k^*/D^* values similar to other cobaltites, ~10^3, were obtained (Figure 3b.7). Steele [14] suggested another criterion for the selection of good cathode material – a substantial value of the product D^*k^*. The values of D^*k^* must be greater than ~10^{-14} cm^3s^{-2} in order to achieve low values of area-specific resistance (ASR) at the cathode (e.g., 0.1 Ω cm^2 at 500 °C). The values of the D^*k^* product as a function of temperature in comparison with other cathode materials are presented on Figure 3b.8. However, Fleig and Maier [15] recently pointed out that the ionic conductivity itself does not determine the extension of the active zone in the TPB. The level of this extension additionally depends on the surface exchange

coefficient and the particle size. The reduction of the particle size resulted in the increase of the active area of the cathode that participates in the oxygen reduction. Fleig and Maier showed that the ionic conductivity becomes less important as the particle size decreases. The high values of k^* and D^* observed in $Sr_3YCo_4O_{10.5}$ suggest that low values of polarization resistance for a $Sr_3YCo_4O_{10.5}$ cathode could be achieved upon the optimization of cathode microstructure.

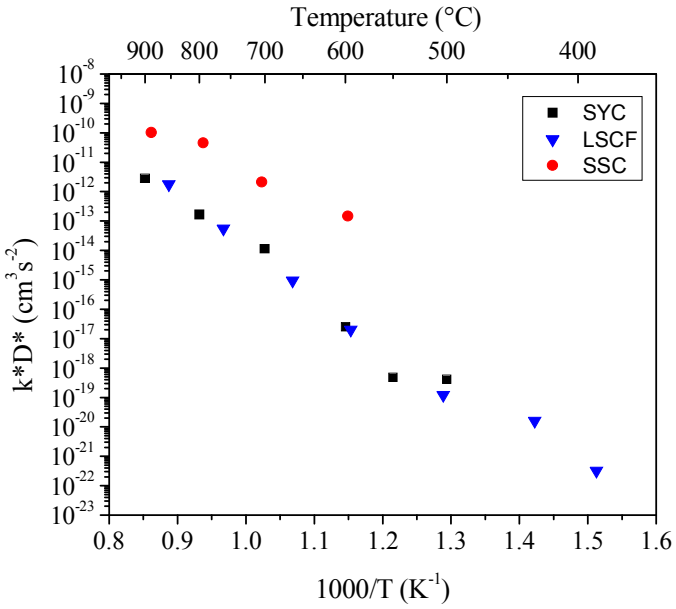

Figure 3b.8. Comparison of the k^*D^* product as a function of reciprocal temperature for $Sr_3YCo_4O_{10.5}$ (this work), $La_{0.6}Sr_{0.4}Fe_{0.8}Co_{0.2}O_{3-x}$ [3] and $Sm_{0.5}Sr_{0.5}CoO_{3-x}$ [12].

To evaluate the electrochemical performance of $Sr_3YCo_4O_{10.5}$ as a cathode material for IT-SOFC's symmetrical cells $Sr_3YCo_4O_{10.5}$ / $Ce_{0.9}Gd_{0.1}O_{1.95}$ / $Sr_3YCo_4O_{10.5}$ were prepared by spraying or screen-printing $Sr_3YCo_4O_{10.5}$ suspension on $Ce_{0.9}Gd_{0.1}O_{1.95}$ pellets and annealing in the temperature range 900 – 1120 ºC. No interaction between

$Sr_3YCo_4O_{10.5}$ and $Ce_{0.9}Gd_{0.1}O_{1.95}$ powders after annealing at 900 °C for 140 hours and at 1120 °C for 2 hours was observed within the detection limit of the XRD technique.

Different morphologies of the cathode layer, resulting from the differences in the layer deposition technique (spraying and screen printing) and sintering temperatures, were observed. The samples sintered at temperatures 900 – 1100 ºC showed poor contact between the cathode and the electrolyte layers, regardless of the deposition method, and consequently very high values of ASR as measured by AC Impedance. Cross-sectional scanning electron microscopy (SEM) images of the sample prepared at 1120 ºC for 2 hours by screen printing showed good contact between the electrode and the electrolyte (Figure 3b.9). The thickness of the cathode layer prepared by the screen printing technique was about 10 µm. The degree of porosity observed in the vicinity of the GDC/SYC interface was slightly higher than in the bulk. This could be caused by a chemical interaction between GDC and SYC which was not detectable by XRD on the powdered samples.

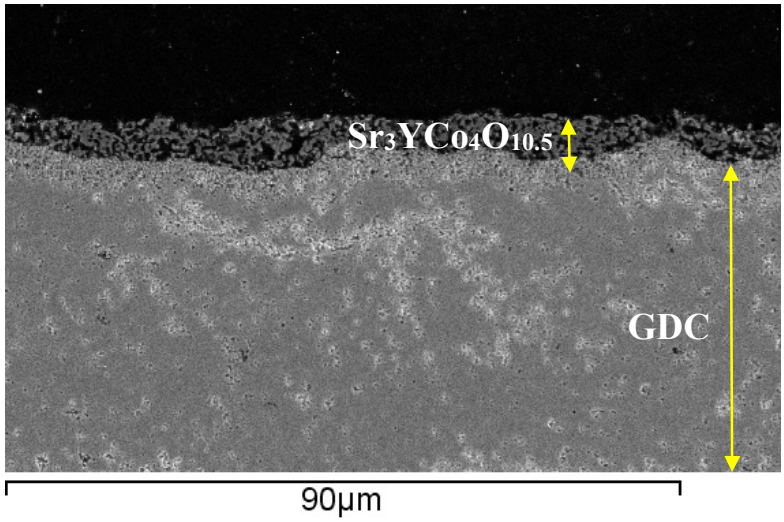

Figure 3b.9. Cross-section of a symmetrical cell SYC/GDC/SYC sintered at 1120 ºC for 2 hours.

Nyquist plots (normalized by the area) of the $Sr_3YCo_4O_{10.5}$ / $Ce_{0.9}Gd_{0.1}O_{1.95}$ / $Sr_3YCo_4O_{10.5}$ cell (sintered at 1120 ºC) in air at different temperatures (620 – 770 ºC) are presented in Figure 3b.10. The impedance spectra consist of a high frequency induction tail caused by the equipment and the measuring leads, a resistance originating from the electrolyte and the measuring leads and a Gerischer type element. The inductance is equipment specific and is not discussed further. The electrolyte resistance, R_e, was calculated by subtraction of the leads contribution determined during a blank measurement. The Gerischer type element of the impedance data was fitted to the ALS continuum model [16] as shown in Figure 3b.10 according to the equation:

$$Z_{chem} = R_{chem}\sqrt{\frac{1}{1+j\omega t_{chem}}} \qquad \text{(Equation 3b.2)}$$

where R_{chem} and t_{chem} are characteristic resistance and time constant, respectively, related to oxygen transport and surface exchange in the mixed ionic and electronic conducting cathode, ω is the frequency of applied a.c. signal. The fit of the experimental data to Eq. (3b.2) is shown in Figure 3b.10 and the calculated parameters are given in Table 3b.2.

The ASR values were calculated by dividing the values of R_{chem} by two in order to reflect the contribution of two electrodes. A good agreement between the fitted and experimental data suggests that the solid state diffusion and oxygen surface exchange dominate the electrochemical performance. At temperatures higher than 720 °C additional semi-circles appeared at high and low frequencies. The semi-circle observed at low frequencies is thought to be caused by gas phase diffusion limitation in the pores of cathode [17]. The origin of the semi-circle at high frequencies is currently unclear. The observed

values of R_{chem} and t_{chem} calculated in this work are within the range of the values measured on the cathode materials with similar values of D^* and k^* [16].

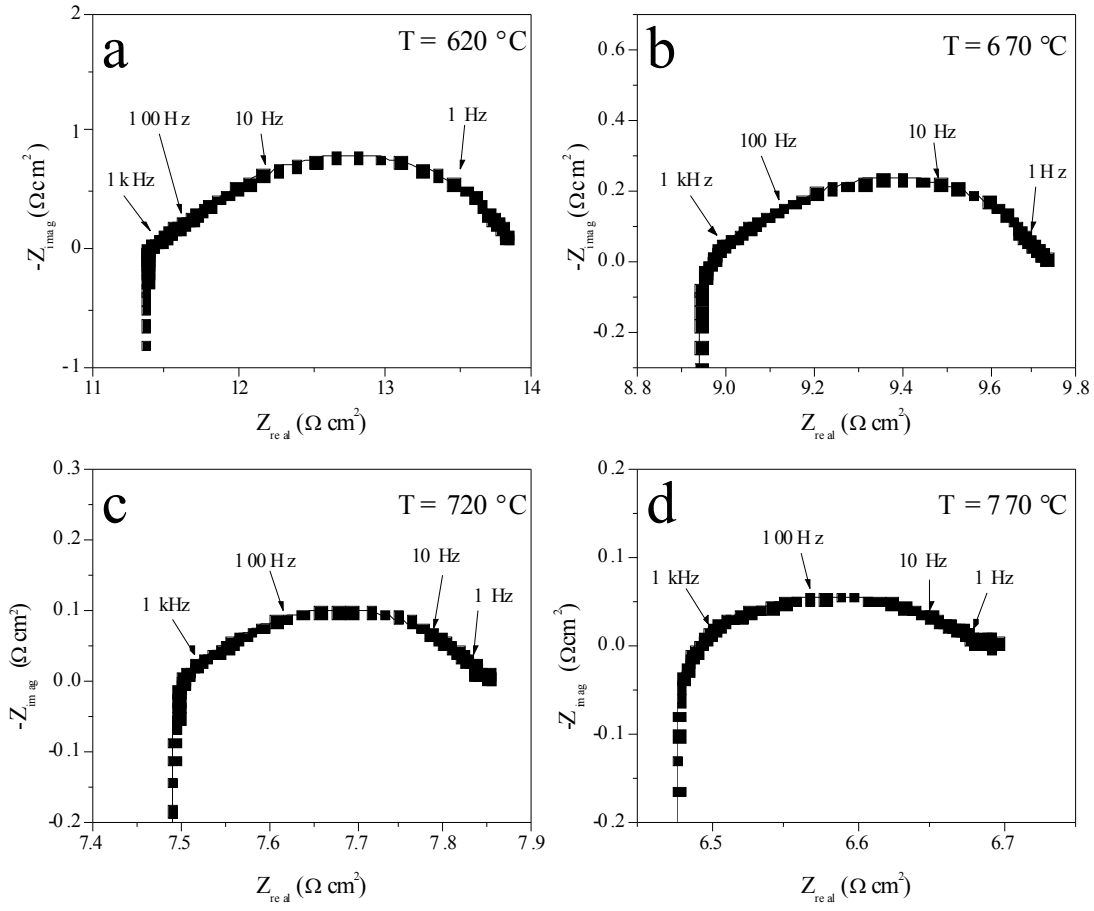

Figure 3b.10. Complex impedance plots for the symmetrical SYC/GDC/SYC cell in air at different temperatures (620, 670, 720, 770 ºC). Frequencies are indicated in Hz. Solid lines are the fits of the experimental data to a Gerischer response according to the Eq. (3b.2).

Table 3b.2. The fitting parameters for the AC impedance data of SYC/GDC/SYC symmetrical cells as a function of temperature.

Parameter	620 °C	670 °C	720 °C	770 °C
R_e (Ω cm^2)	10.36	7.86	6.34	5.25
R_{chem} (Ω cm^2)	2.38 ± 0.01	0.73 ± 0.01	0.33 ± 0.01	0.18 ± 0.01
t_{chem} (s)	0.47 ± 0.01	0.11 ± 0.01	0.05 ± 0.01	0.04 ± 0.01
ASR (Ω cm^2)	1.19 ± 0.01	0.37 ± 0.01	0.17 ± 0.01	0.09 ± 0.01

The observed value of ASR of symmetrical cell at 700 – 720 °C was around 0.2 Ω cm^2. This value is larger than the reported ASR values for other promising Co containing perovskites (e.g. 0.1 Ω cm^2 at 700 °C for $GdBaCo_2O_{5+x}$ [18]), however an improvement of the electrochemical performance can be achieved upon further optimization of the cathode microstructure. For example, Peters et al. [17] reported a very low ASR value of 0.13 Ω cm^2 at 600 °C for nanostructured $La_{0.5}Sr_{0.5}CoO_{3-\delta}$ cathode on GDC electrolyte. The temperature dependences of the conductivity (expressed as 1/ASR) follows the Arrhenius-type law within the 620 – 770 °C range (Figure 3b.11) with the activation energy, E_A^{ASR}, of 1.37 ± 0.11 eV. The activation energy of conductivity in $Sr_3YCo_4O_{10.5}$ determined in this work is lower than the reported values for GDC symmetrical cells with $GdBaCo_2O_{5+x}$ (E_A = 1.43 eV), $La_{0.8}Sr_{0.2}CoO_{3-x}$ (E_A = 1.7 eV) and $La_{0.8}Sr_{0.2}FeO_{3-x}$ (E_A = 1.9 eV) cathodes [18, 19].

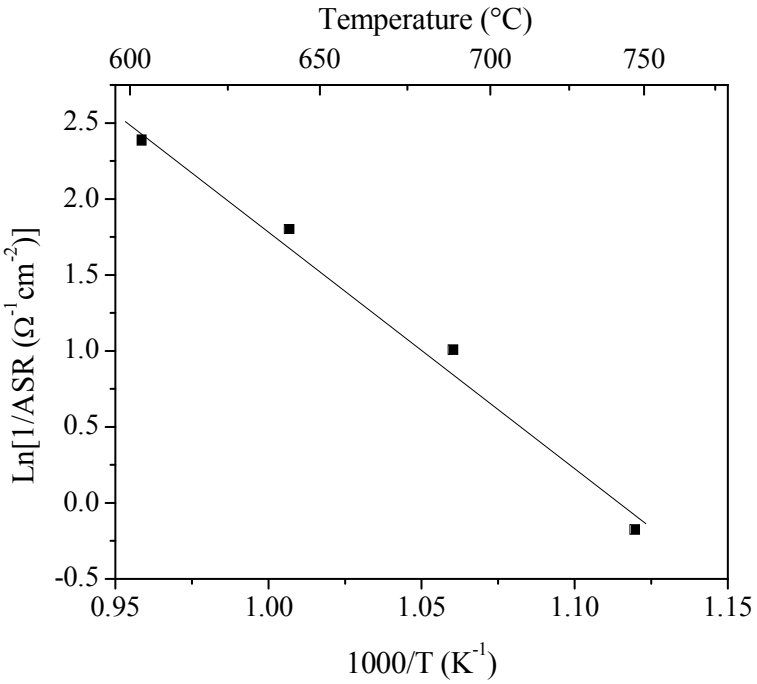

Figure 3b.11. Arrhenius plot of 1/ASR in SYC/GDC/SYC symmetrical cells determined by AC impedance. Solid line is a guide to eye.

The observed high oxygen transport and low ASR values together with previously reported high electronic conductivity [20], makes $Sr_3YCo_4O_{10.5}$ a good candidate for cathodes in IT-SOFC applications. However, further research is required to determine the influence of the cathode microstructure on the SOFC performance. Moreover, additional studies of oxygen diffusion and surface exchange in analogous cobalt-based perovskite-related 314-phases with different A-site cations and/or with partial substitution of cobalt are required.

3b.5. Conclusions

High values of oxygen diffusion coefficients and surface exchange coefficients were obtained for $Sr_3YCo_4O_{10.5}$ by IEDP/SIMS analysis in the temperature range 500 – 900 °C. The experimental data were in a good agreement with the recent data for the oxygen diffusion coefficients obtained by molecular dynamic modeling. The polarization resistance of the symmetrical $Sr_3YCo_4O_{10.5}$ / $Ce_{0.9}Gd_{0.1}O_{1.95}$ / $Sr_3YCo_4O_{10.5}$ cells was dominated by solid state diffusion and surface exchange in the cathode and was adequately described by the ALS model. The low values of ASR were measured within the temperature range 620 – 770 °C in air. The layered perovskites, with the so called 314-phases, showed promising electrochemical performance and could be considered as alternative cathodes in IT-SOFCs.

3b.6. References

1. Perry Murray, E.; Barnett, S. A. (La, Sr)MnO_3–(Ce, Gd)O_{2-x} composite cathodes for solid oxide fuel cells. *Solid State Ionics* **2001**, *143*, 265-273.

2. Kim, J.-D.; Kim, G.-D.; Moon, J.-W.; Park, Y.; Lee, W.-H.; Kobayashi, K.; Nagai, M.; Kim, C.-E. Characterization of LSM–YSZ composite electrode by ac impedance spectroscopy. *Solid State Ionics* **2001**, *143*, 379-389.

3. Benson, S. J.; Chater, R. J.; Kilner, J. A. Oxygen diffusion and surface exchange in the mixed conducting perovskite $La_{0.6}Sr_{0.4}Fe_{0.8}Co_{0.2}O_{3-d}$. In *Proceedings of the 3rd International Symposium on Ionic and Mixed Conducting Ceramics*; The Electrochemical Society: Pennington, NJ, 1997; pp 596-609.

4. Istomin, S. Y.; Grins, J.; Svensson, G.; Drozhzhin, O. A.; Kozhevnikov, V. L.; Antipov, E. V.; Attfield, J. P. Crystal structure of the novel complex cobalt oxide $Sr_{0.7}Y_{0.3}CoO_{2.62}$. *Chem. Mater.* **2003**, *15*, 4012-4020.

5. Rupasov, D.; Chroneos, A.; Parfitt, D.; Kilner, J. A.; Grimes, R. W.; Istomin, S. Ya.; Antipov, E. V. Oxygen diffusion in $Sr_3YCo_4O_{10.5}$: A molecular dynamics study. *Phys. Rev. B* **2009**, *79*, 172102/1-172102/4.

6. Rietveld, H. M. A profile refinement method for nuclear and magnetic structures. *Powder Diffr.* **1969**, *2*, 65-71.

7. Killoran, D. R. The effective duration of a linear slow-cool. *J. Electrochem. Soc.* **1962**, *109*, 170-171.

8. De Souza, R. A. Ionic transport in acceptor doped perovskites. PhD. Dissertation, University of London, 1996.

9. *FEI FIB 200 Workstation user's guide*, FEI Co., Hillsboro, OR, USA, **1994**.

10. Crank, J. *The mathematics of diffusion*. Clarendon Press: Oxford, 1975; p 12.

11. *1260 Impedance/Gain-Phaze analyzer operating manual*, Solartron Analytical, **1996**.

12. Fullarton, I. C.; Kilner, J. A.; Steele, B. C. H.; Middleton, P. H. Characterization of oxygen ion transport in selected perovskite structured oxides by O^{18}/O^{16} isotopic exchange and dynamic secondary ion mass spectrometry. In *Proceedings of the 2rd International Symposium on Ionic and Mixed Conducting Ceramics*; The Electrochemical Society: Pennington, NJ, 1994; pp 9-24.

13. Doorn, R. H. E.; Fullarton, I. C.; De Souza, R. A.; Kilner, J. A.; Bouwmeester, H. J. M.; Burggraaf, A. J. Surface oxygen exchange of $La_{0.3}Sr_{0.7}CoO_{3-\delta}$. *Solid State Ionics* **1997**, *96*, 1-7.

14. Steele, B. C. H. Materials for IT-SOFC stacks: 35 years R&D: the inevitability of gradualness? *Solid State Ionics* **2000**, *134*, 3-20.

15. Fleig, J.; Maier, J. The polarization of mixed conducting SOFC cathodes: Effects of surface reaction coefficient, ionic conductivity and geometry. *J. Eur. Ceram. Soc.* **2004**, *24*, 1343-1347.

16. Adler, S. B.; Lane, J. A.; Steele, B. C. H. Electrode kinetics of porous mixed-conducting oxygen electrodes. *J. Electrochem. Soc.* **1996**, *143*, 3554-3564.

17. Peters, C.; Weber, A.; Ivers-Tiffée, E. Nanoscaled $La_{0.5}Sr_{0.5}CoO_{3-\delta}$ thin film cathodes for SOFC application at 500 °C<T<700 °C. *J. Electrochem. Soc.* **2008**, *155*, B730-B737.

18. Tarancón, A.; Skinner, S.J.; Chater, R.J.; Hernández-Ramírez, F.; Kilner, J. A. Layered perovskites as promising cathodes for intermediate temperature solid oxide fuel cells. *J. Mater. Chem.* **2007**, *17*, 3175-3181.

19. Ralph, J. M.; Schoeler, A. C.; Krumpelt, M. Materials for lower temperature solid oxide fuel cells. *J. Mater. Sci.* **2001**, *36*, 1161-1172.

20. Istomin, S. Ya.; Drozhzhin, O. A.; Napolsky, Ph. S.; Putilin, S. N.; Gippius, A. A.; Antipov, E. V. Thermal expansion behavior and high-temperature transport properties of $Sr_3YCo_{4-x}Fe_xO_{10.5+y}$, x = 0.0, 1.0, 2.0 and 3.0. *Solid State Ionics* **2008**, *179*, 1054-1057.

Chapter 3c. Oxygen diffusion in $Sr_3YCo_4O_{10.5}$: An electrical conductivity relaxation and thermogravimetric analysis approach

3c.1. Abstract

Chemical oxygen diffusion coefficients and chemical surface exchange rates along with oxygen self-diffusion coefficients in dense samples of $Sr_3YCo_4O_{10.5+\delta}$ were studied by using a combination of electrical conductivity relaxation measurements (ECR) and thermogravimetric analysis data (TGA) in the temperature range of 650 – 900 °C. Arrhenius behavior, $A = A_0 \exp(\frac{-E_A}{kT})$, was observed with activation energies of $E_A^{D_{chem}} = 1.16 \pm 0.01$ eV, $E_A^{D_O} = 1.56 \pm 0.01$ eV and $E_A^{k_{chem}} = 0.76 \pm 0.05$ eV for the chemical oxygen diffusion coefficient, the oxygen self-diffusion coefficient, and the chemical surface exchange rate, respectively. The thermodynamic factor changes with temperature from 611 at 650 °C to 177 at 900 °C.

3c.2. Introduction

In order to make solid oxide fuel cells (SOFCs) more commercially viable, it is desirable to decrease their operating temperature as much as possible [1]. Lower operating temperature also decreases the reactivity of all SOFC components thereby improving stability and reliability. However, the requirement of high values of electronic and ionic conductivity can become a limitation on the performance at lower temperature. The rate of the oxygen reduction reaction is a particular problem and consequently, it is necessary to

determine oxygen diffusion and electrical conductivity in a wide range of temperatures (500 – 1000 °C) for all novel and prospective cathode materials for SOFC applications.

Several different techniques have been used to determine oxygen diffusion coefficients in ceramic materials. The most developed method is isotope exchange and depth profiling in combination with secondary ion mass spectrometry (IEDP/SIMS) [2]. This technique allows measurements of oxygen diffusion coefficients in both electron-conducting and dielectric materials [3, 4] over a wide range of temperature, and in case of single crystals, along different crystallographic directions [5]. But, at the same time IEDP/SIMS requires the use of expensive ^{18}O and SIMS damages the sample. Another technique for the determination of oxygen diffusion, namely molecular dynamic simulations (MD), became available with increase in computational power. MD provides detailed information about oxygen diffusion pathways and rates, and requires information only about the crystal structure of the particular compound studied [6]. Due to the assumption of ideal conditions in MD simulations, the results may deviate from IEDP/SIMS experimental measurements [3].

Relaxation techniques are commonly used for studying kinetics. The change in a specific property of the system to a new equilibrium state is observed after the system has experienced a rapid change in its physical or chemical environment. To study oxygen transport, any property that reflects the oxygen concentration, such as weight, volume, conductivity, optical properties, can be investigated [7]. Given the relationship between oxygen concentration and oxygen partial pressure, relaxation experiments on mixed ionic and electronic compounds (MIECs) can be performed by rapid changing the oxygen partial pressure in the ambient environment at a constant temperature.

Compared with other relaxation techniques, electrical conductivity measurements are much less affected by gas fluctuations or other minor physical changes that occur during the relaxation experiment. Moreover, conductivity is extremely sensitive to the defect concentration [8, 9]. Therefore, the electrical conductivity relaxation (ECR) experiment is the most commonly employed relaxation technique for determining oxygen transport kinetics [9-13].

In the present work, we used the ECR technique to determine oxygen diffusion in $Sr_3YCo_4O_{10.5+\delta}$, which was studied previously with both IEDP/SIMS and Molecular Dynamic simulations [3, 6]. The relative oxygen stoichiometry was determined by thermogravimetric analysis at different partial pressures of oxygen (2% - 75%), while absolute values were determined by iodometric titration.

3c.3. Experimental

The perovskite-related compound $Sr_3YCo_4O_{10.5}$ (314-phase) was synthesized by solid-state reaction of stoichiometric amounts of $SrCO_3$, Co_3O_4 and Y_2O_3 with intermediate grindings and sinterings in the range of temperatures 900 – 1200 °C [14]. The temperature of the final sintering (1160 °C) was adjusted to allow formation of a single phase material but at the same time to prevent densification of the powder. A single-phase compound with small particle size was necessary for densification using a cold isostatic press (CIP) and subsequent sintering.

The crystal structure and phase purity of $Sr_3YCo_4O_{10.5}$ powder were analyzed by X-ray powder diffraction using Cu-Kα radiation.

The powder was ball milled in ethanol for 48 h and dried in a vented oven for another 48 h. Dense pellets of the $Sr_3YCo_4O_{10.5}$ were prepared by isostatically pressing at 30,000 psi with subsequent sintering at 1180 °C for 4 h with heating and cooling rates of 1 °C/min. The density of the pellets was measured by the Archimedes technique and was greater than the 95% that is required to prevent oxygen transport through the pores. Due to the fact that during an ECR experiment one dimension of the sample is reserved for the conductivity measurement, the geometry of the sample has special requirements. In theory, the length of the sample in the conductivity measurement direction should be infinite, but good results can be achieved on samples where one dimension is an order of magnitude larger than another two [15]. For ECR measurements a bar with dimensions t = 1.43 mm, w = 1.09 mm and l = 19.72 mm was cut and polished to decrease the effect of surface morphology on oxygen diffusion (Figure 3c.1).

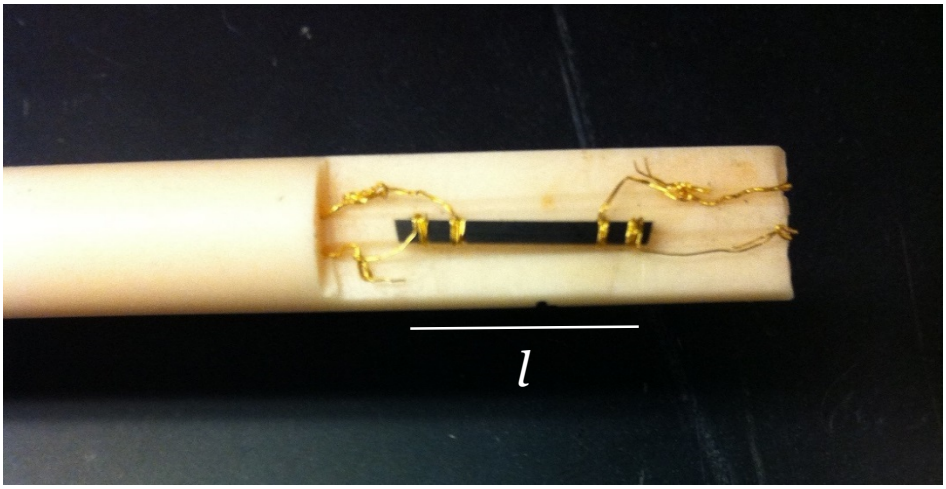

Figure 3c.1. The sample of $Sr_3YCo_4O_{10.5}$ for ECR measurements with dimensions t = 1.43 mm, w = 1.09 mm and l = 19.72 mm.

To equilibrate the sample in the apparatus and improve the contacts with the gold wires, the bar was heated from room temperature to 900 °C and then cooled back to ambient temperature before ECR measurements. The electrical conductivity was measured during the heating and cooling cycle.

Oxygen atom transport in a dense mixed ionic electronic conducting (MIEC) oxide can be generally described by two processes namely surface exchange and bulk diffusion. The mathematical solutions of the mass transport equations under various conditions are well established using a linear surface exchange model [16].

The change in oxygen partial pressure in the surroundings of the MIEC sample leads to oxygen adsorption or rejection and as a result, to a change in electron-hole concentration and change of electrical conductivity (Equation 3c.1), which is measured during an electrical conductivity relaxation experiment (ECR).

$$V_O^{\cdot\cdot} + \frac{1}{2}O_2(g) \leftrightarrow O_O^x + 2h^{\cdot} \qquad \text{(Equation 3c.1)}$$

For a rod sample with a $2l_1$ by $2l_2$ cross-section, if its length is much greater than the sides, according to the Wagner's theory and the mass-conservative law (Equations 3c.2, 3c.3) and boundary conditions (Equations 3c.4, 3c.5, 3c.6) it is possible to describe relative electrical conductivity as a function of time, chemical surface exchange and chemical oxygen diffusion (Equations 3c.7, 3c.8).

$$j_{O^{2-}}(x,t) = -D_{chem}\frac{\partial c_{O^{2-}}(x,t)}{\partial x} \qquad \text{(Equation 3c.2),}$$

$$\frac{\partial c_{O^{2-}}(x,t)}{\partial t} = -\frac{\partial j_{O^{2-}}(x,t)}{\partial x} \qquad \text{(Equation 3c.3),}$$

$$c_{O^{2-}}(x,0) = c_{O^{2-}}^{(1)} \qquad \text{(Equation 3c.4),}$$

$$\left.\frac{\partial c_{O^{2-}}}{\partial x}\right|_{x=0} = 0 \qquad \text{(Equation 3c.5)},$$

$$k_{chem}\left(c_{O^{2-}} - c_{O^{2-}}^{(2)}\right) = -D_{chem}\left.\frac{\partial c_{O^{2-}}}{\partial x}\right|_{x=\pm l} \qquad \text{(Equation 3c.6)},$$

where D_{chem} and k_{chem} are chemical oxygen diffusion and chemical surface exchange coefficients, $c_{O^{2-}}^{(1)}$ and $c_{O^{2-}}^{(2)}$ are oxygen ion concentrations in the solid at equilibrium with the initial and final oxygen partial pressures, $pO_2^{(1)}$ and $pO_2^{(2)}$, respectively.

$$\frac{M_t}{M_\infty} = 1 - \sum_{n=1}^{\infty}\sum_{m=1}^{\infty}\frac{2C_1^2\exp(-\alpha_{1m}^2\tilde{D}_O t/l_1^2)}{\alpha_{1m}^2(\alpha_{1m}^2+C_1^2+C_1)} \times \frac{2C_2^2\exp(-\alpha_{2n}^2\tilde{D}_O t/l_2^2)}{\alpha_{2n}^2(\alpha_{2n}^2+C_2^2+C_2)}$$

(Equation 3c.7),

$$\frac{M_t}{M_\infty} = \frac{c_{O^{2-}}(t) - c_{O^{2-}}^{(1)}}{c_{O^{2-}}^{(2)} - c_{O^{2-}}^{(1)}} = \frac{\sigma(t)-\sigma^{(1)}}{\sigma^{(2)}-\sigma^{(1)}} = g(t) \qquad \text{(Equation 3c.8)},$$

where *g(t)* is the relative conductivity; M_t/M_∞ is the fractional change of the total mass of oxygen; *C* is a measure of the importance of the contribution of the surface exchange reaction, and is defined as the ratio of the half thickness to the characteristic length of the sample, l_d (Equation 3c.9); α_{1m} and α_{2n} are the positive roots of the transcendental equations (Equation 3c.10),

$$C_1 = \frac{l_1}{l_d}, C_2 = \frac{l_2}{l_d}, l_d = \frac{D_{chem}}{k_{chem}} \qquad \text{(Equation 3c.9)},$$

$$\alpha_{1m} tan\, \alpha_{1m} = C_1, \alpha_{2n} tan\, \alpha_{2n} = C_2 \qquad \text{(Equation 3c.10)}.$$

During the ECR experiment, the sample was located in the tube furnace at a certain temperature in a flow of gas with certain oxygen partial pressure (O_2/N_2 mixtures with different concentrations of oxygen) [17]. A rapid switch, less than 2.5 s for the gas switching delay [18], from one oxygen partial pressure to another led to the change of electrical conductivity of the sample, and was measured by AC 4-probe method with

SR830 DSP Lock-In Amplifier at a single frequency of 13333 Hz. As a result, conductivity relaxation profiles (conductivity vs. time) were obtained. Oxygen diffusion kinetics were investigated with ECR in the temperature range 650 – 900 °C by following switches of oxygen partial pressure: 2% ↔ 5%, 10% ↔ 20%, 10% ↔ 75%.

The results of ECR experiments represent chemical oxygen diffusion and chemical surface exchange and are different from those obtained during the isotope exchange depth profiling experiments (IEDP). The switch of the oxygen partial pressure is an external driving force, while during the IEDP the oxygen partial pressure is fixed. To compare results of IEDP and ECR it is necessary to know the thermodynamic factor (Γ_O), which represents the variation of the oxygen concentration in the sample (c_O) with temperature and oxygen partial pressure, pO_2, in the surroundings (Equation 3c.11). We used thermogravimetric analysis (TGA) to study this dependence.

$$\Gamma_O = \frac{1}{2} \cdot \frac{\partial \ln(pO_2)}{\partial \ln(c_O)} \qquad \text{(Equation 3c.11).}$$

TGA was performed at different oxygen partial pressures in the temperature range 25 °C – 900 °C. At each pO_2, three TGA experiments were made to be sure that the heating and cooling profiles were identical. The final measurements at 2%, 20% and 75% of pO_2 were normalized to the initial weight and converted to oxygen content (c_O) vs. temperature. Absolute oxygen contents were determined by iodometric titration [19]. Oxygen self-diffusion coefficients were calculated in the temperature range 650 – 900°C using Equation 3c.12.

$$D_O = D_{chem}/\Gamma_O \qquad \text{(Equation 3c.12),}$$

where D_O is oxygen self-diffusion coefficient.

3c.4. Results and discussion

The lattice parameters of the synthesized compound were refined by the Rietveld method [20] using the structural model provided by Istomin *et al.* [14]. The unit cell parameters were in good agreement with the ones previously reported in the literature [14], a = 7.62389(1) Å and c = 15.32701(5) Å and the sample was confirmed to be a single phase.

The measured values for electrical conductivity are in good agreement with literature data [21] with the maximum value of 550 S/cm (Figure 3c.2). The increase in conductivity at lower temperature corresponds to thermal activation, while the decrease above 600 °C can be explained by formation of oxygen vacancies and the resulting decrease in the electron-hole concentration.

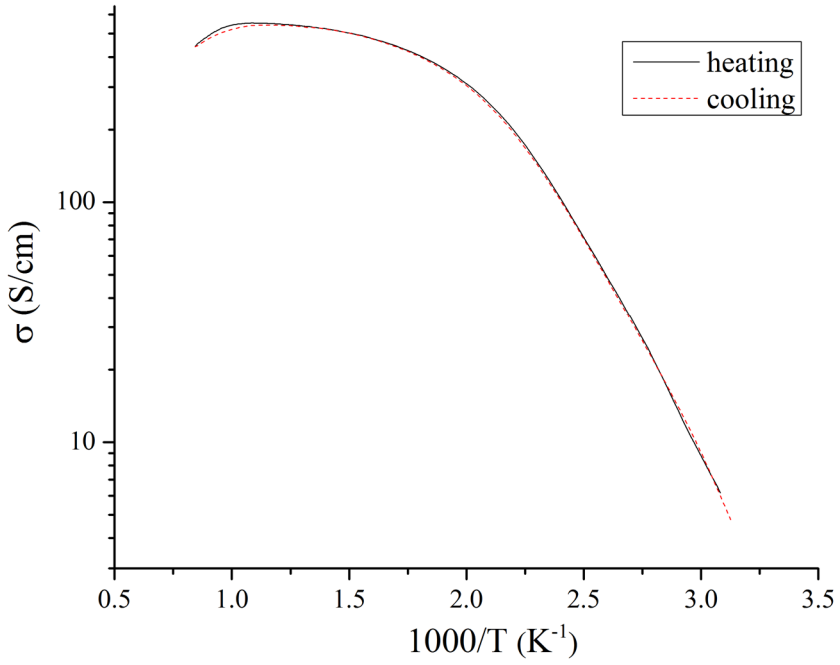

Figure 3c.2. Electrical conductivity of $Sr_3YCo_4O_{10.5}$ in air.

Electrical conductivity relaxation profiles were normalized and fitted to Eq. 3c.7. Typical normalized relative conductivity vs. time profiles are presented in Figure 3c.3. Good agreement between the experimental data and the fits were observed at all temperatures and all oxygen partial pressure switches. Comparison of the profiles obtained during switches of oxygen partial pressure from 10% to 75% at different temperatures showed as expected significantly faster relaxation with increase of temperature (Figure 3c.4).

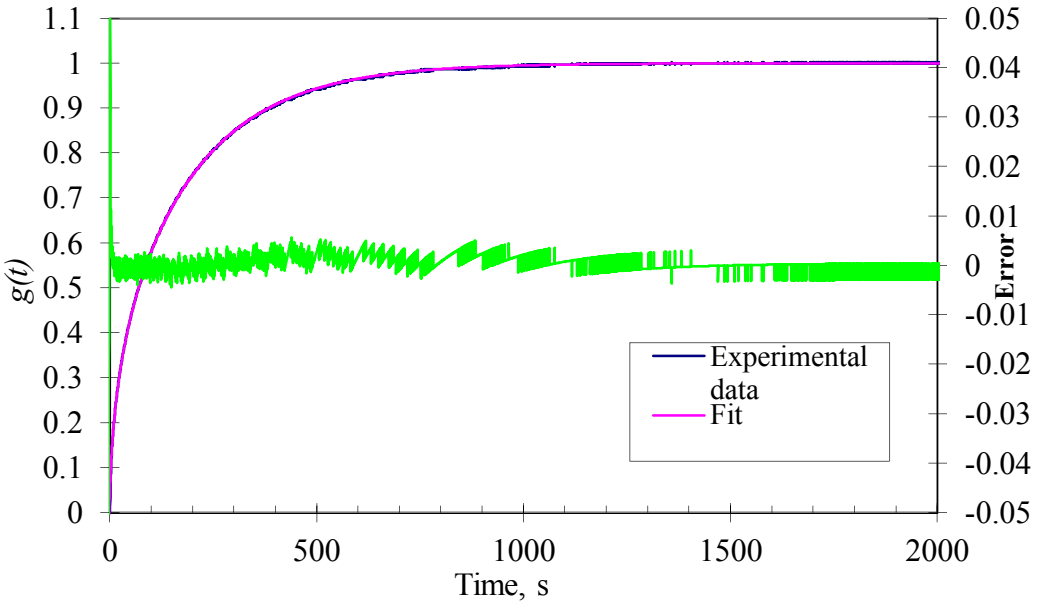

Figure 3c.3. Relative electrical conductivity vs. time profile obtained during an ECR experiment at 850 °C with an oxygen partial pressure switch from 10% to 75% and the corresponding fit.

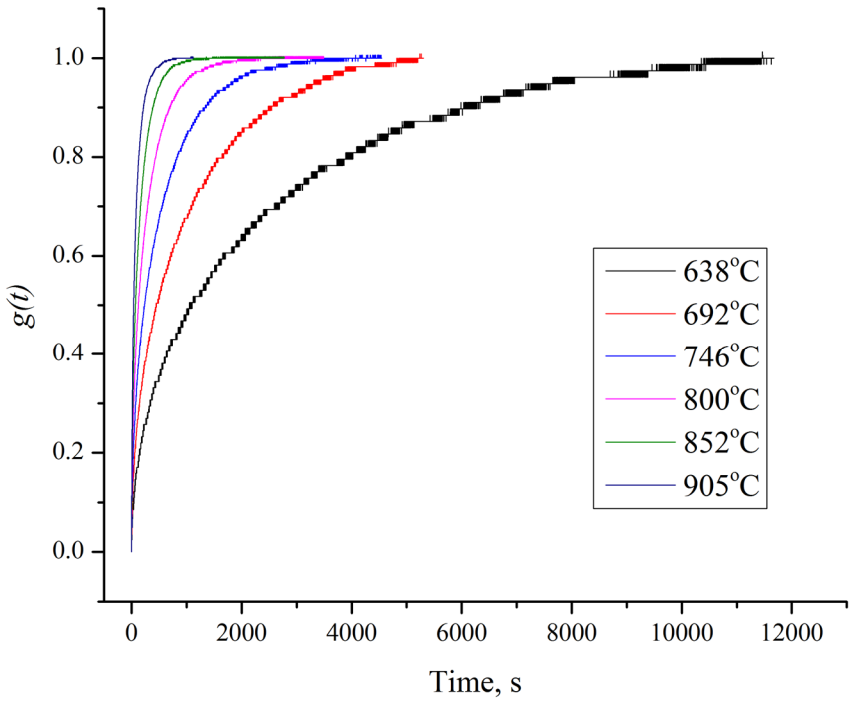

Figure 3c.4. Comparison of profiles of relative conductivity, $g(t)$, of $Sr_3YCo_4O_{10.5}$ vs. time obtained during ECR experiments at different temperatures and for switches of oxygen partial pressure from 10% to 75%.

Values of the chemical oxygen diffusion and chemical surface exchange coefficients were obtained after the fitting of all profiles (Figure 3c.5). Activation energies for D_{chem} and k_{chem} are 1.16 ± 0.01 eV and 0.76 ± 0.05 eV, respectively.

The values of chemical oxygen diffusion coefficient do not depend on the initial and final oxygen partial pressures and depend only on the temperature, in good agreement with the model of oxygen diffusion in the bulk material. Comparison of the pO_2 switches 20% → 10% and 75% → 10% shows that chemical surface exchange rates also do not depend on the initial oxygen partial pressure, but do depend on the final oxygen partial

pressure (Figure 3c.5). Dependence of chemical surface exchange rate on final oxygen partial pressure at different temperatures is presented in the Figure 3c.6 and follows a power law, $k_{chem} \propto [pO_2^{(2)}]^n$, where n was determined from the slopes of $\log(k_{chem})$ vs. $\log(pO_2^{(2)})$ and is in the range 0.56 – 0.62.

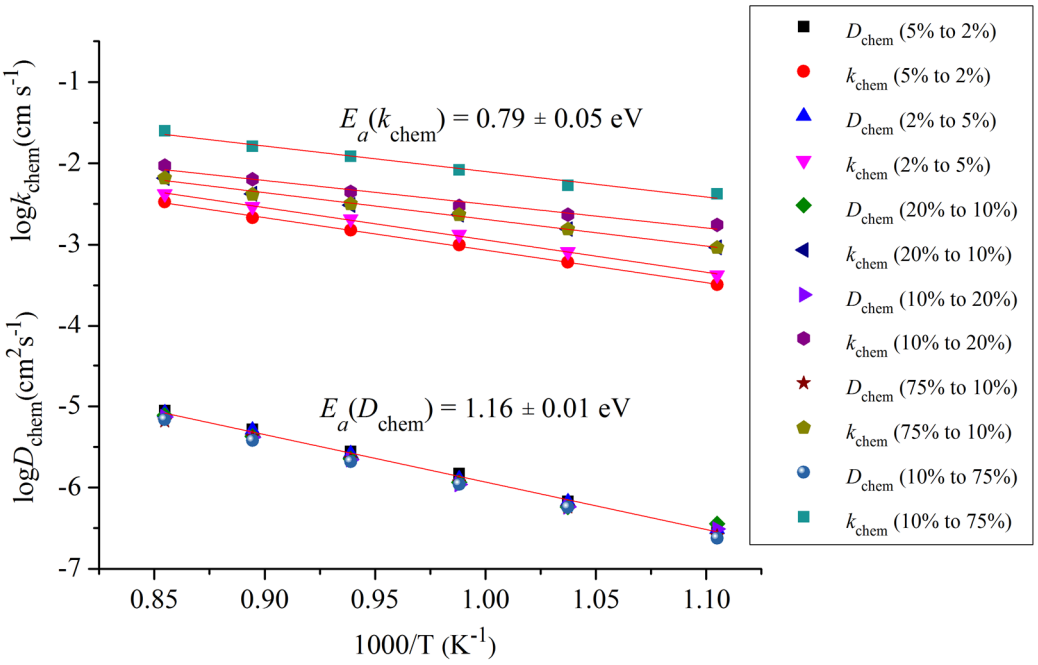

Figure 3c.5. Arrhenius plot of the chemical oxygen diffusion and chemical surface exchange coefficients obtained for $Sr_3YCo_4O_{10.5}$ by ECR experiment.

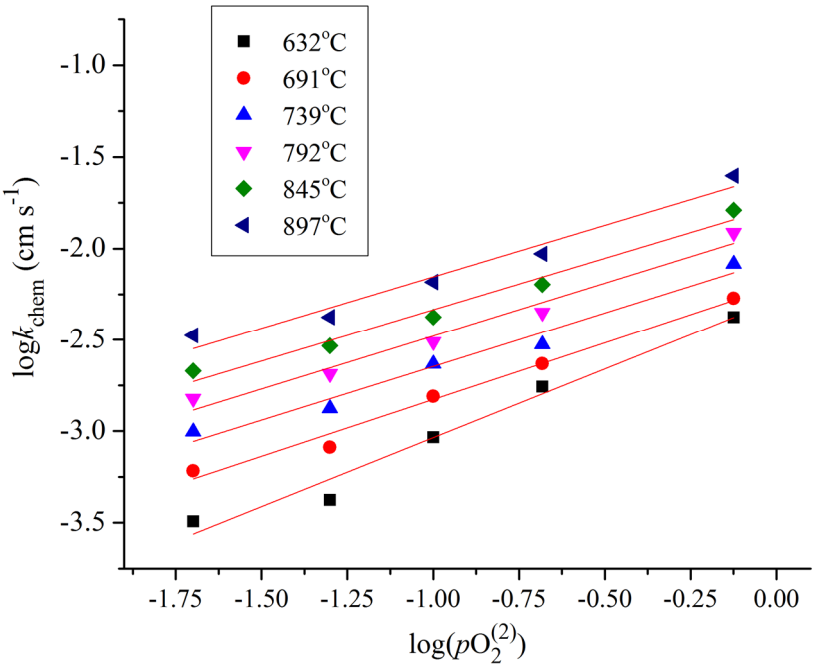

Figure 3c.6. Dependence of chemical surface exchange rate for $Sr_3YCo_4O_{10.5}$ on final oxygen partial pressure during ECR switches.

The dependence of oxygen content (c_O) on temperature and oxygen partial pressure in the surroundings obtained by thermogravimetric analysis is presented in Figure 3c.7 at pO_2 = 0.02 atm, 0.20 atm and 0.75 atm. Profiles are in good agreement with the literature data [14] and show rapid decrease with increasing temperature. Values of the thermodynamic factor calculated with Eq. 3c.11 at different temperatures change from 611 at 650 °C to 177 at 900 °C and are listed in Table 3c.1, along with the values of oxygen self-diffusion calculated with Eq. 3c.12. Significant difference in the thermodynamic factors measured at different oxygen partial pressures is a consequence of the non-linear oxygen atom release from the structure with increasing temperature.

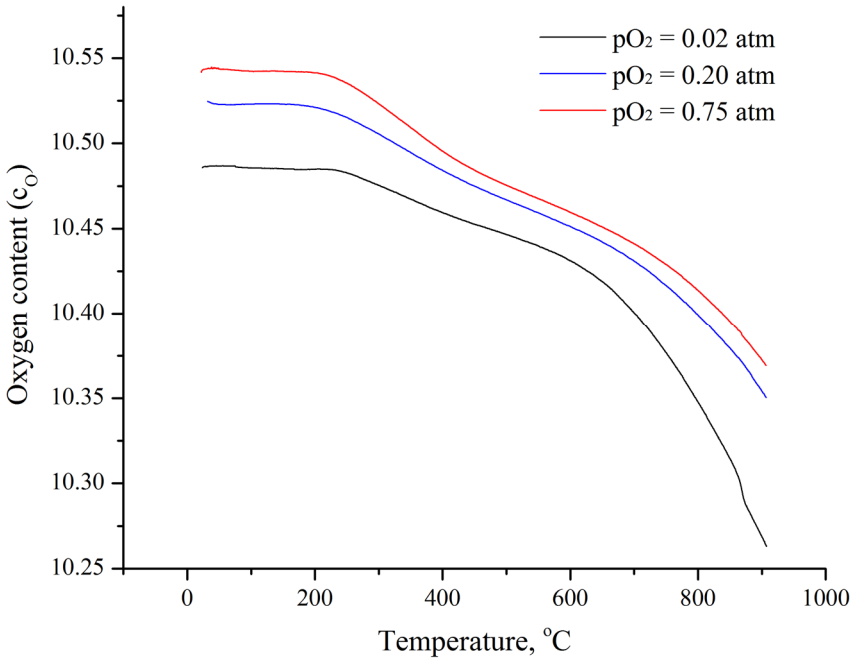

Figure 3c.7. Dependence of oxygen content in $Sr_3YCo_4O_{10.5}$ on oxygen partial pressure in the surroundings and temperature determined by TGA.

Comparison of the oxygen self-diffusion in $Sr_3YCo_4O_{10.5}$ obtained by ECR/TGA with our previous results obtained by IEDP/SIMS and MD is presented in Figure 3c.8 [3, 6]. Very good agreement is observed between oxygen diffusion coefficients obtained in dense samples by ECR/TGA and IEDP/SIMS methods, while results of molecular dynamic simulations show slightly higher values, what can be explained by ideal conditions and some assumptions made in the simulation experiments [6].

Table 3c.1. Thermodynamic factor for $Sr_3YCo_4O_{10.5}$ determined from TGA profiles, and chemical oxygen diffusion and oxygen self-diffusion coefficients in the temperature range 650 – 900 °C.

	650 °C	700 °C	750 °C	800 °C	850 °C	900 °C
Γ_O	611 (± 34)	483 (± 31)	370 (± 30)	290 (± 22)	230 (± 23)	176 (± 18)
$\log(D_{chem})$	-6.54	-6.22	-5.92	-5.63	-5.35	-5.12
$\log(D_O)$	-9.32 (± 0.03)	-8.90 (± 0.03)	-8.48 (± 0.04)	-8.09 (± 0.04)	-7.72 (± 0.05)	-7.37 (± 0.05)

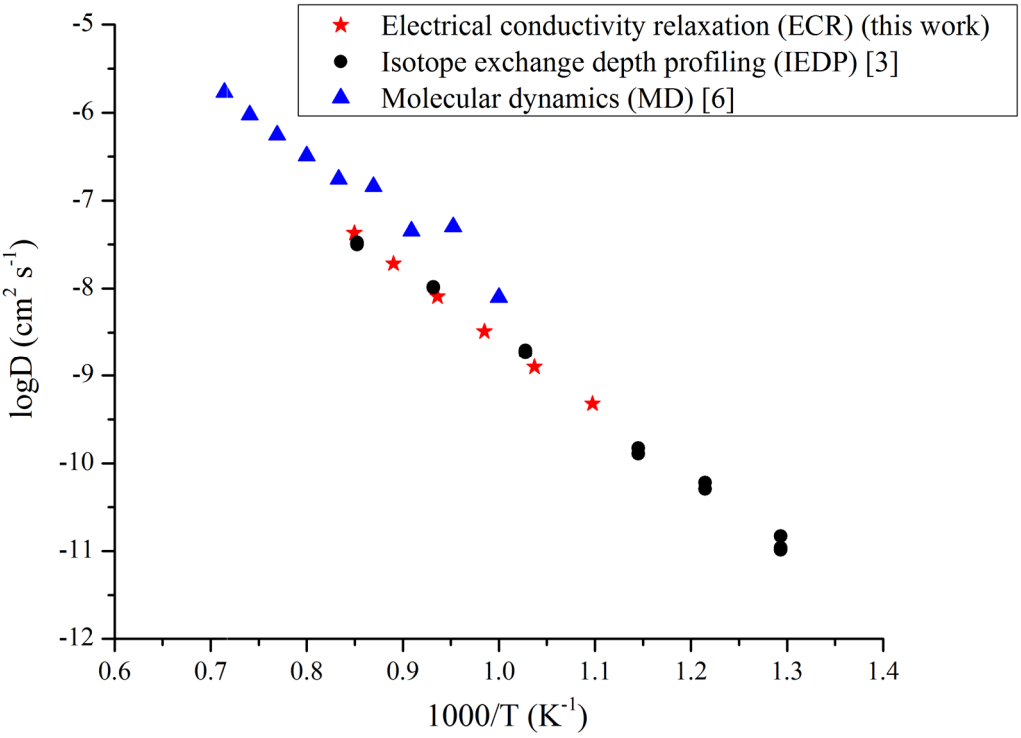

Figure 3c.8. Comparison of oxygen self-diffusion coefficients in $Sr_3YCo_4O_{10.5}$ determined by ECR (this work), IEDP/SIMS [3] and molecular dynamics [6].

It was shown that the ECR/TGA approach to the oxygen diffusion study provides the same values of oxygen self-diffusion as IEDP/SIMS experiments, but at the same time provides additional information about chemical oxygen diffusion and chemical surface exchange along with dependence of oxygen content in the structure on temperature and oxygen partial pressure in the surroundings.

3c.5. Conclusions

Values of chemical surface exchange and chemical oxygen diffusion coefficients in $Sr_3YCo_4O_{10.5}$ were obtained with electrical conductivity relaxation technique in the temperature range 650 – 900 °C. The thermodynamic factor calculated from the oxygen stoichiometry measured by thermogravimetric analysis, was used to determine values of the oxygen self-diffusion coefficient. Results are in excellent agreement with the oxygen-tracer diffusion coefficients determined previously by isotope exchange depth profiling and molecular dynamic simulations. Activation energies for chemical oxygen diffusion and oxygen self-diffusion are 1.16 ± 0.01 eV and 1.56 ± 0.01 eV, respectively.

3c.6. Acknowledgement

The work was supported by the Robert A Welch Foundation (Grant No. E-0024, TM; TGA measurements) and the U.S. Department of Energy (U.S. DOE), Office of Basic Energy Sciences, Division of Materials Sciences and Engineering (under Award No. DE-SC0001284, DR, AJJ; experiments and analysis).

3c.7. References

1. Charpentier, P.; Fragnaud, P.; Schleich, D. M.; Denos, Y.; Gehain, E. Preparation of thin film SOFCs working at reduced temperature. *Ionics* **1998**, *4*, 118-123.

2. Tannhauser, D. S.; Kilner, J. A.; Steele, B. C. H. The determination of the oxygen self-diffusion and gas-solid exchange coefficients for stabilized zirconia by SIMS. *Nuclear Instruments and Methods in Physics Research* **1983**, *218*, 504-508.

3. Rupasov, D. P.; Berenov, A. V.; Kilner, J. A.; Istomin, S. Y.; Antipov, E. V. Oxygen diffusion in $Sr_{0.75}Y_{0.25}CoO_{2.62}$. *Solid State Ionics* **2011**, *197*, 18-24.

4. Manning, P.; Sirman, J.; Kilner, J. Oxygen self-diffusion and surface exchange studies of oxide electrolytes having the fluorite structure. *Solid State Ionics* **1996**, *125*, 125-132.

5. Bredikhin, S. I.; Emel'chenko, G. A.; Shechtman, V. Sh.; Zhokhov, A. A.; Carter, S.; Chater, R. J.; Kilner J. A.; Steele, B. C. H. Anisotropy of oxygen self-diffusion in $YBa_2Cu_3O_{7-\delta}$ single crystals. *Physica C* **1991**, *179*, 286-290.

6. Rupasov, D.; Chroneos, A.; Parfitt, D.; Kilner, J. A.; Grimes, R. W.; Istomin, S. Ya.; Antipov, E. V. Oxygen diffusion in $Sr_{0.75}Y_{0.25}CoO_{2.625}$: A molecular dynamics study. *Phys. Rev. B* **2009**, *79*, 172102/1-172102/4.

7. Riess, L. *The CRC handbook of solid state electrochemistry*. Gellings, P. J.; Bouwmeester, H. J. M., Eds.; CRC press: Boca Raton, 1997, p 223.

8. Elshof, J. E. ten; Lankhorst, M. H. R.; Bouwmeester, H. J. M. Oxygen exchange and diffusion coefficients of strontium-doped lanthanum ferrites by electrical conductivity relaxation. *J. Electrochem. Soc.* **1997**, *144*, 1060-1067.

9. Yasuda, I.; Hikita, T. Precise determination of the chemical diffusion coefficient of calcium-doped lanthanum chromites by means of electrical conductivity relaxation. *J. Electrochem. Soc.* **1994**, *141*, 1268-1273.

10. Song, C.-R.; Yoo, H.-I. Chemical diffusivity of $BaTiO_{3-\delta}$ I. Experimental determination. *Solid State Ionics* **1999**, *120*, 141-153.

11. Kim, G.; Wang, S.; Jacobson, A. J.; Reimus, L.; Brodersen, P.; Mims, C. A. Rapid oxygen ion diffusion and surface exchange kinetics in $PrBaCo_2O_{5+x}$ with a perovskite related structure and ordered A-cations. *J. Mater. Chem.* **2007**, *17*, 2500-2505.

12. Yu, C. J.; Sparlin, D. M.; Anderson, H. U. Oxidation kinetics of polycrystalline $LaCrO_3$. *J. Amer. Ceramic Soc.* **1987**, *70*, C-189-C-192.

13. Yasuda, I.; Hishinuma, M. Electrical conductivity and chemical diffusion coefficient of strontium-doped lanthanum manganites. *J. Solid State Chem.* **1996**, *123*, 382-390.

14. Istomin, S. Y.; Grins, J.; Svensson, G.; Drozhzhin, O. A.; Kozhevnikov, V. L.; Antipov, E. V.; Attfield, J. P. Crystal structure of the novel complex cobalt oxide $Sr_{0.7}Y_{0.3}CoO_{2.62}$. *Chem. Mater.* **2003**, *15*, 4012-4020.

15. Wang, S. Oxygen transport in mixed conducting perovskite oxides. PhD. Dissertation. University of Houston, 2000.

16. Franke, P.; Dieckmann, R. Nonstoichiometric compounds. In *Advances in ceramics*; Catlow, C. R. A.; Mackrodt, W. C., Eds.; American Ceramic Society: Weaterville, OH, 1987; Vol. 23; p 27.

17. Chen. L.; Chen, C.; Jacobson, A. J. Electrical conductivity relaxation studies of oxygen transport in epitaxial $YBa_2Cu_3O_{7-d}$ thin films. *IEEE Transactions on Applied Superconductivity* **2003**, *13*, 2882-2885.

18. Wang, S.; Verma, A.; Yang, Y. L.; Jacobson, A. J.; Abeles, B. The effect of the magnitude of the oxygen partial pressure change in electrical conductivity relaxation measurements: oxygen transport kinetics in $La_{0.5}Sr_{0.5}CoO_{3-\delta}$. *Solid State Ionics* **2001**, *140*, 125-133.

19. Karppinen, M.; Matvejeff, M.; Salomaki, K.; Yamauchi, H. Oxygen content analysis of functional perovskite-derived cobalt oxides, *J. Mater. Chem.* **2002**, *12*, 1761-1764.

20. Rietveld, H. M. A profile refinement method for nuclear and magnetic structures. *J. Applied Cryst.* **1969**, *2*, 65-71.

21. Drozhzhin, O. A. New complex perovskite-related Co-based compounds. PhD. Dissertation. Moscow State University, 2009.

Chapter 4. Oxygen transport in $LnBaCoFeO_{5+x}$

Mixed ionic electronic oxides with the double-perovskite structure have been studied extensively in the last few years due to their high values of electronic and ionic conductivity and the possibility of their application as cathodes in solid oxide fuel cells [1-4]. The structure of double perovskites, $AA'B_2O_{5+\delta}$ (A = rare earth element, A' = alkaline earth metal, B = first row transition metal), undergoes ordering due to the difference in ionic radii of A and A' metals and can be described by the stacking sequence …|A'O|BO_2|AO_δ|BO_2|… (Figure 4.1). The oxygen vacancies are mostly formed in the AO_δ layers, the so-called oxygen vacancy layers.

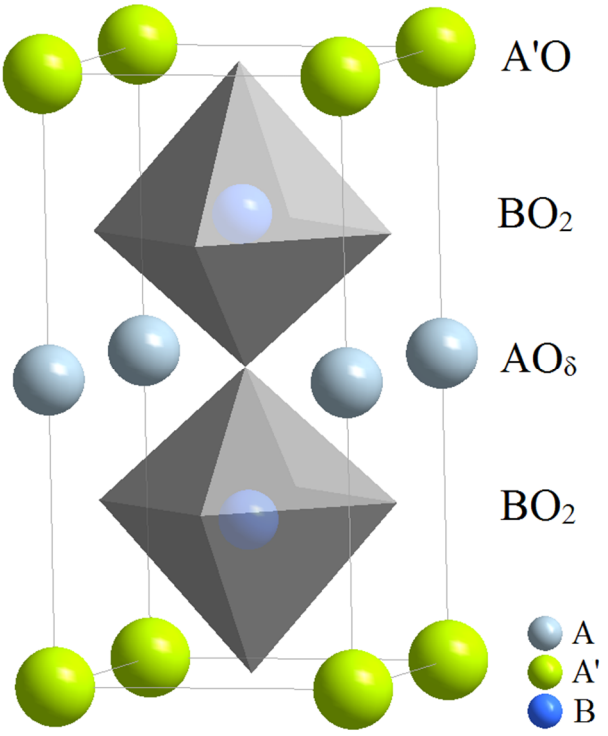

Figure 4.1. The structure of the double perovskites, $AA'B_2O_{5+\delta}$ (A = rare earth element, A' = alkaline earth metal, B = first row transition metal).

Oxygen transport properties in cobalt-based double perovskites, $LnA'Co_2O_{5+\delta}$ (Ln = rare earth elements, A' = alkaline earth metals), were studied with isotope depth profiling, electrical conductivity relaxation and molecular dynamics simulations. High values of oxygen uptake were measured in $GdBaCo_2O_{5+\delta}$ by TGA and the importance of the oxygen-vacancy layers to this process was clearly indicated [1]. Isotope exchange depth profiling measurements of oxygen transport in this compound were performed by Kilner *et al.* [2]. The compounds $LnBaCo_2O_{5+\delta}$ (Ln = Pr, Nd) were studied by IEDP/SIMS and electrical conductivity relaxation techniques, and significantly faster oxygen kinetics in comparison with disordered perovskites were observed [3]. The effect of cation disorder in the A-sublattice of $GdBaCo_2O_{5+\delta}$ was investigated by molecular dynamics simulations [4]. It was predicted that increase in A-cation disorder leads to reduction of oxygen diffusivity and to appearance of the diffusion along the *c*-axis of the structure, while oxygen diffusion in completely ordered $GdBaCo_2O_{5+\delta}$ occurs only in *a*-*b* plane.

Along with high values of electrical and ionic conductivity, Co-based compounds demonstrate high values of thermal expansion (TEC), what makes their application as cathode materials for solid oxide fuel cells impossible. Partial substitution of Co with other transition metals, such as Fe or Mn, may decrease thermal expansion coefficients in perovskites and perovskite-related structures, but, at the same time, may negatively affect the oxygen transport properties.

This chapter is focused on the investigation of oxygen transport in $LnBaCoFeO_{5+\delta}$ (Ln = La, Pr, Sm, Gd) by a combination of electrical conductivity relaxation and TGA methods.

4.1. Synthesis and sample preparation

Double perovskite compounds $LnBaCoFeO_{5+\delta}$ (Ln = La, Pr, Sm, Gd) were synthesized by solid-state reaction of stoichiometric amounts of $BaCO_3$, Co_3O_4, Fe_2O_3 and Ln_2O_3 (Pr_6O_{11}) with intermediate grindings and sintering in the range of temperatures 900 – 1225 °C in air. The temperatures used for the final sintering of powders were adjusted to allow formation of single phase materials but at the same time to prevent densification of the powder. Single-phase compounds with small particle size were necessary for densification using a cold isostatic press (CIP) and subsequent sintering.

Sintering in flows of nitrogen and oxygen at temperatures up to 1200 °C were performed for Pr, Sm and Gd-containing compounds to study the possibility of formation of disordered structures.

In the case of the La-containing compound sintering in a flow of $5\%H_2/N_2 - N_2$ (ratio 1:30) at 1120 °C for 12 h allowed formation of the ordered double perovskite structure.

The powders were ball milled in ethanol for 48 h and dried in a vented oven for another 48 h. Dense pellets of the $LnBaCoFeO_{5+\delta}$ (Ln = La, Pr, Sm, Gd) were prepared by isostatically pressing at 30,000 psi with subsequent sintering in the temperature range 1120 – 1225°C with heating and cooling rates of 1 °C/min. The specific sintering temperature and time used for each sample are given in Table 4.1. The densities of the pellets were measured by the Archimedes technique and were greater than the 95% of theoretical density.

Table 4.1. Sample preparation and dimensions for electrical conductivity measurements and electrical conductivity relaxation experiments.

Sample	Sample preparation	Density	Dimensions	Distance between voltage electrodes
$LaBaCoFeO_{5+\delta}$ disordered (cubic)	1160 °C / 400 min air	95.11 %	1.07×1.68×16.27 mm	10.49 mm
$LaBaCoFeO_{5+\delta}$ ordered (tetragonal)	1120 °C / 12 h 5%H_2/N_2 – N_2 (ratio 1:30)	95.11 %	0.76×1.67×16.93 mm	10.84 mm
$PrBaCoFeO_{5+\delta}$ ordered (tetragonal)	1180 °C / 300 min air	96.20 %	1.08×1.41×15.31 mm	9.34 mm
$SmBaCoFeO_{5+\delta}$ ordered (tetragonal)	1225 °C / 180 min air	99.22 %	0.74×1.15×13.17 mm	7.36 mm
$GdBaCoFeO_{5+\delta}$ ordered (tetragonal)	1160 °C / 400 min air	99.06 %	0.99×1.09×16.97 mm	11.24 mm

For electrical conductivity measurements and electrical conductivity relaxation experiments bar samples were cut from dense pellets with a low speed diamond saw. All surfaces of the samples were polished to decrease surface morphology effects during the measurements. Four gold wires were attached to each sample with the maximum possible distance between inner voltage electrodes. Figure 3c.1 represents the connection of the sample to the sample holder with gold wires. The dimensions of the samples and distances between voltage electrodes are summarized in Table 4.1.

4.2. Sample characterization

The crystal structures and phase purity of synthesized compounds were analyzed by X-ray powder diffraction using Cu-Kα radiation (λ = 1.54178 Å).

All synthesized compounds were determined to be single-phases. All observed peaks of $LnBaCoFeO_{5+\delta}$ (Ln = Pr, Sm and Gd) regardless of sintering atmosphere (air, N_2, O_2) were indexed with a tetragonal *P4/mmm* unit cell. XRD patterns of $LnBaCoFeO_{5+\delta}$ (Ln = Pr, Sm and Gd) synthesized in air are shown in Figures 4.2(b), 4.2(c), 4.2(d).

The formation of ordered double-perovskite structures in case of Pr, Sm and Gd-containing compounds occurs regardless of the sintering atmosphere. The shift of the unit cell parameters for $LnBaCoFeO_{5+\delta}$ (Ln = Pr, Sm and Gd) on sintering in atmospheres with different pO_2s is presented in Figures 4.3(b), 4.3(c), 4.3(d).

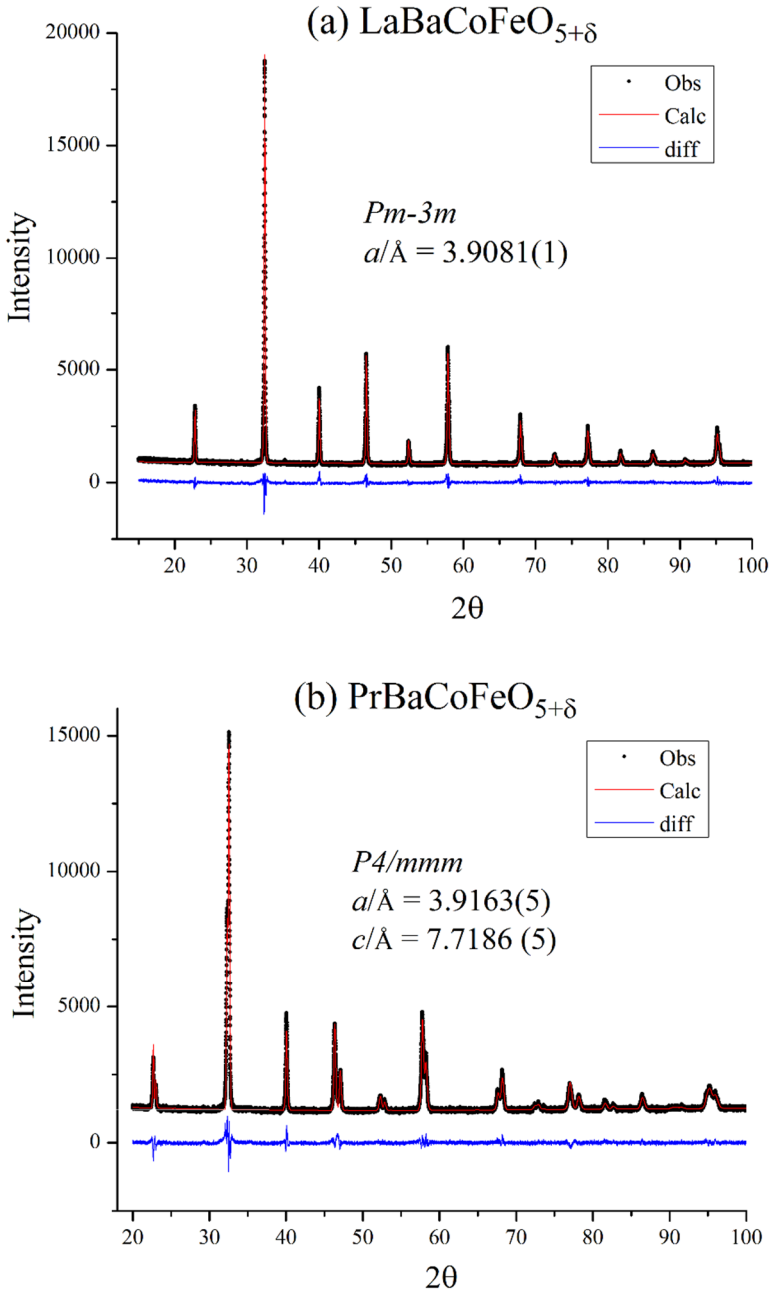

Figure 4.2. XRD patterns of double perovskites synthesized in air: (a) $LaBaCoFeO_{5+\delta}$, (b) $PrBaCoFeO_{5+\delta}$ (continued).

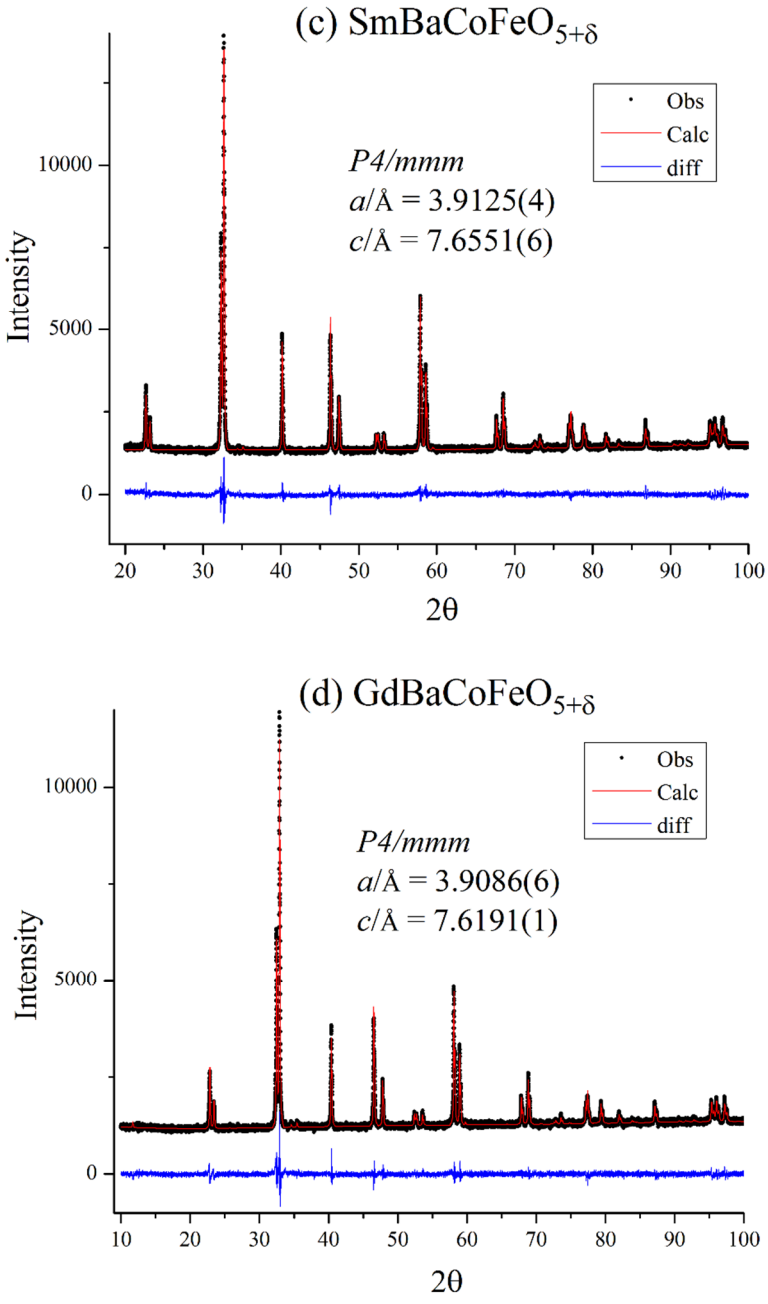

Figure 4.2. (continued) XRD patterns of double perovskites synthesized in air: (c) $SmBaCoFeO_{5+\delta}$, (d) $GdBaCoFeO_{5+\delta}$.

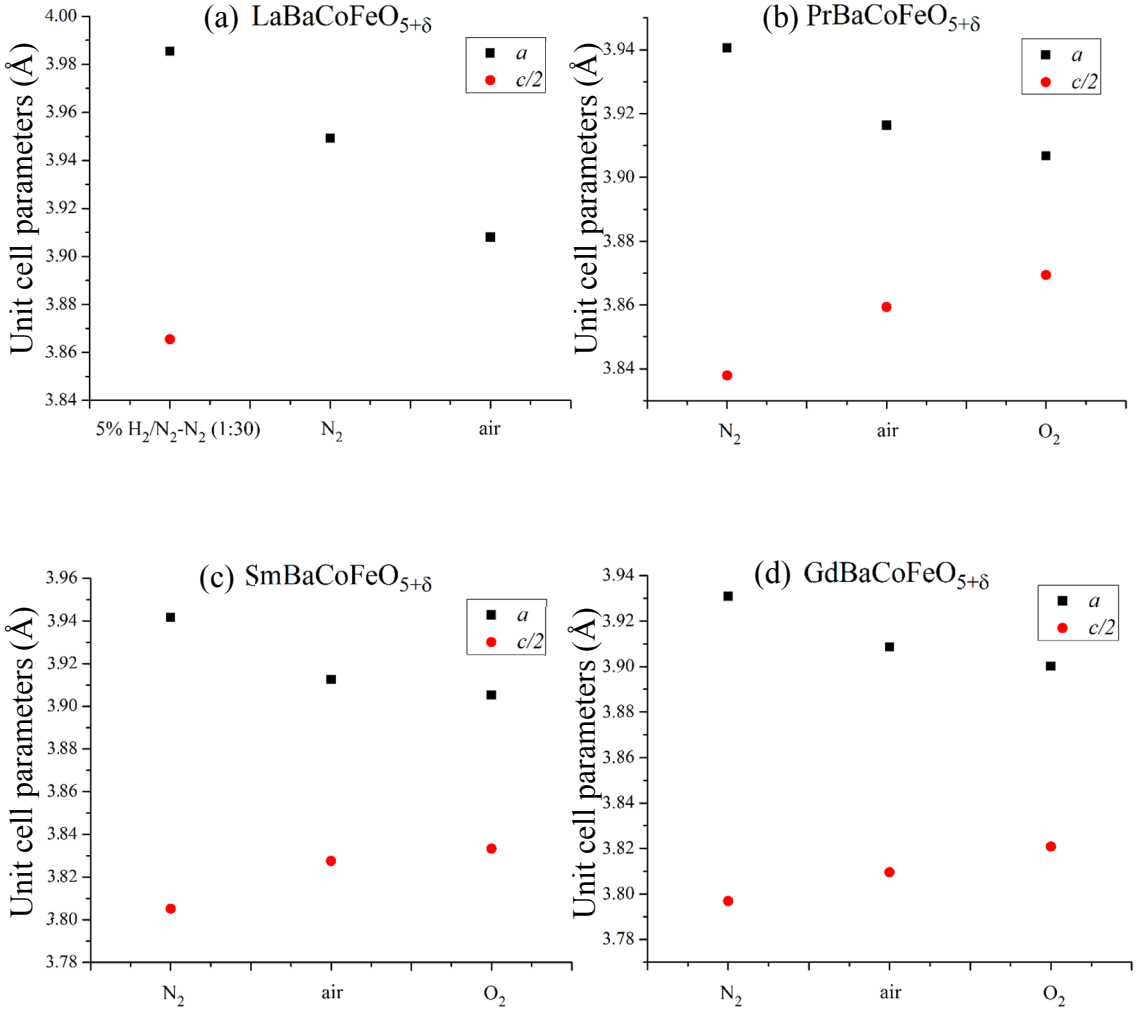

Figure 4.3. Comparison of unit cell parameters of $LnBaCoFeO_{5+\delta}$ sintered in different atmospheres. (a) La, (b) Pr, (c) Sm, (d) Gd.

The decrease of unit cell parameter *a* and increase of *c*/2 with increase of pO_2 can be explained by increase of oxygen content. Additional oxygen in the structure increases the oxidation state of Co and Fe and leads to a small decrease of ionic radii of B-cations and as a result to a decrease of all unit cell parameters. At the same time, the introduction

of oxygen atoms into oxygen vacancy layers, LnO_{δ}, significantly increases the unit cell parameter along the *c*-axis.

Due to the small difference in ionic radii between La and Ba, the formation of only disordered perovskite structure (a cubic *Pm-3m* unit cell) observed for La-containing compounds synthesized in air and nitrogen gas (Figure 4.2(a)).

It was clearly indicated that oxygen content of nitrogen gas is not low enough to permit ordering of the A-cation sublattice of $LaBaCoFeO_{5+\delta}$. The formation of single-phase $LaBaCoFeO_{5+\delta}$ with ordered A-cation sublattice was observed after sintering of cubic phase in the flow of $5\%H_2/N_2 - N_2$ (ratio 1:30) at 1120 °C for 12 hours. All peaks were indexed with a tetragonal *P4/mmm* unit cell (Figure 4.4).

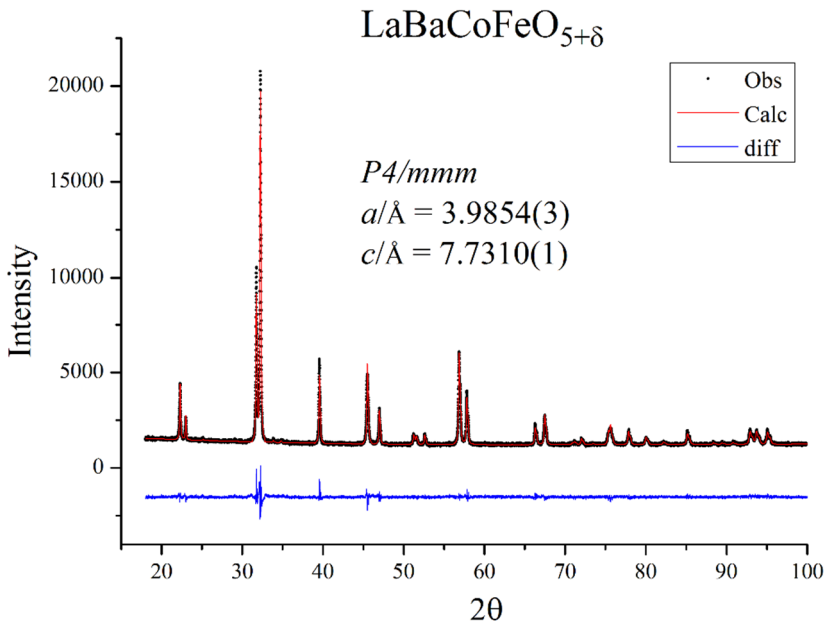

Figure 4.4. XRD pattern of ordered $LaBaCoFeO_{5+\delta}$.

Dependence of the unit call parameters of $LaBaCoFeO_{5+\delta}$ on the oxygen partial pressure in the surroundings during the synthesis is presented in Figure 4.3(a). The stability of the ordered $LaBaCoFeO_{5+\delta}$ in an oxidizing atmosphere was studied by heating at 950 °C for 2, 6 and 16 h in air. Formation of disordered cubic phase was not observed (Figure 4.5). The peak splitting in 46 – 47 ° 2θ region corresponds to tetragonal symmetry.

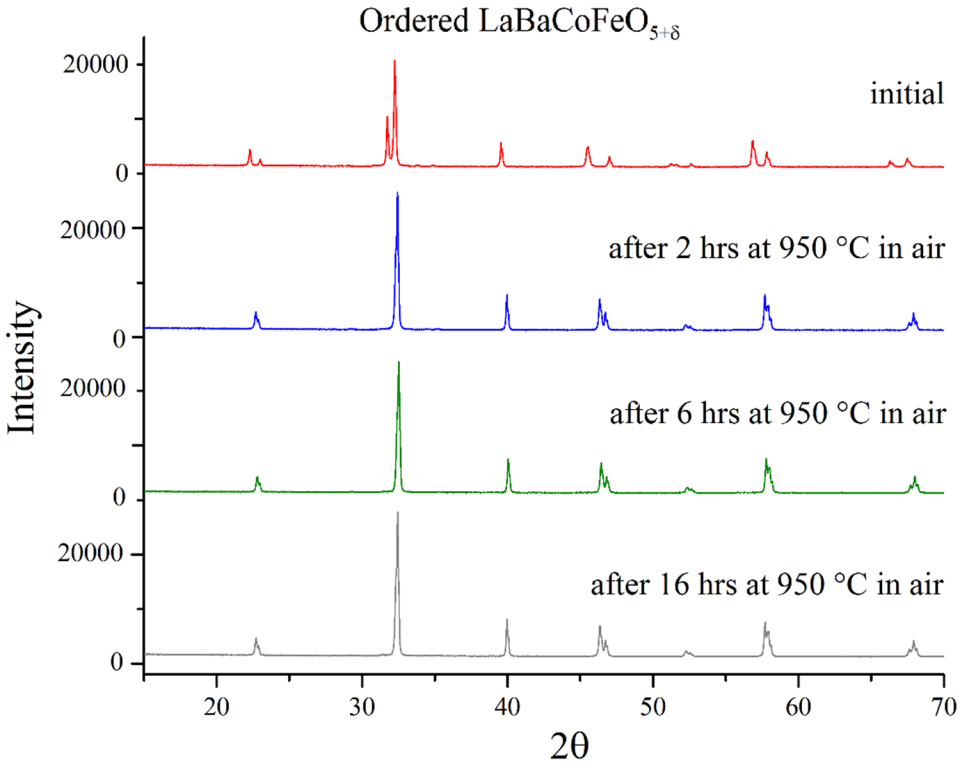

Figure 4.5. Stability of ordered $LaBaCoFeO_{5+\delta}$ in air at 950 °C.

4.3. Electrical conductivity

To equilibrate samples in the apparatus and improve contacts with gold wires before the electrical conductivity relaxation experiments, each bar was heated in air from room temperature to 900 °C and then cooled back to ambient temperature. Electrical conductivity was measured during this process (Figure 4.6). The observed behavior of the electrical conductivity with temperature corresponds to *p*-type semiconductors and is common for Co-containing perovskites and perovskite-related structures [5, 6].

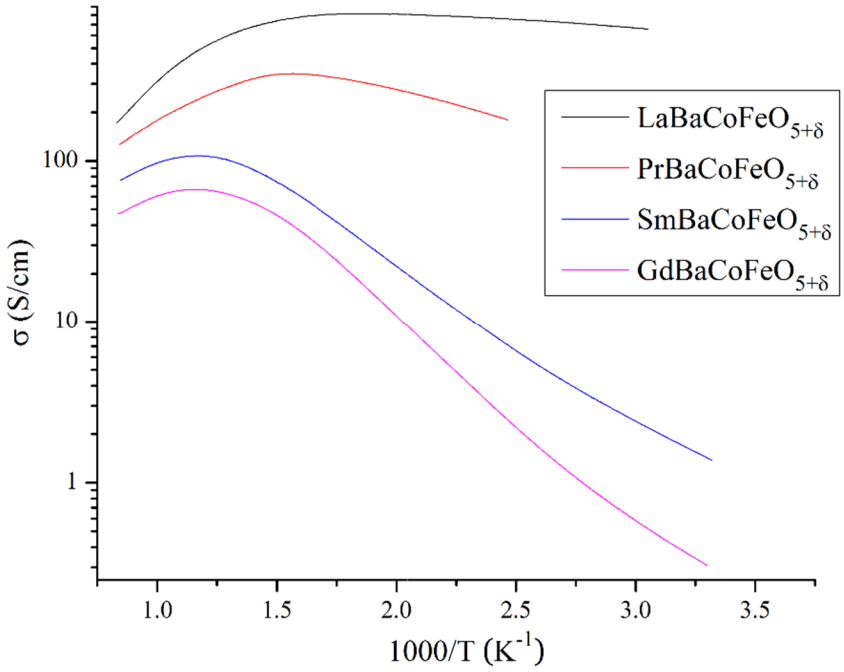

Figure 4.6. Electrical conductivity of $LnBaCoFeO_{5+\delta}$ (Ln = La, Pr, Sm and Gd) in air.

The increase in conductivity in the low temperature region corresponds to thermal activation, while the decrease above 390 – 550 °C, depending on rare earth element, can be explained by formation of oxygen vacancies (release of oxygen from the structure) and

the resulting decrease in the electron-hole concentration (Eq. (4.1)). Thermogravimetric analysis of $LnBaCoFeO_{5+\delta}$ at different oxygen partial pressures, summarized in Chapter 4.6, shows significant release of oxygen from the structures with increase of temperature and correlates with the suggestion above.

$$O_O^x + 2h^{\cdot} \rightarrow V_O^{\cdot\cdot} + \frac{1}{2}O_2(g) \qquad \text{(Equation 4.1)}$$

4.4. Electrical conductivity relaxation

During the ECR experiment, samples were located in the tube furnace at certain temperatures in a flow of gas with a certain oxygen partial pressure (O_2/N_2 mixtures with different oxygen content). A rapid switch, less than 2.5 s for the gas switching delay, from one oxygen partial pressure to another led to the change in the electrical conductivity of the sample, and was measured by the AC 4-probe method with SR830 DSP Lock-In Amplifier at a single frequency of 13333 Hz. As a result, conductivity relaxation profiles (conductivity vs. time) were obtained. Oxygen-diffusion kinetics were investigated with ECR in the temperature range 550 – 900 °C by the following switches of the oxygen partial pressure: 2% ↔ 5%, 10% ↔ 20%, 10% ↔ 75%, 20% ↔ 75%. Additional switches were performed to monitor the stability of the samples by returning periodically to a standard set of conditions established at the beginning of the experiment and comparing the results with the initial data.

Electrical conductivity relaxation profiles were normalized and fitted to Eq. (3c.7). Good agreements between the experimental data and the fits were observed at all temperatures and all oxygen partial pressure switches.

For La and Pr-containing samples, however, we were not able to obtain consistent values of the chemical oxygen diffusion and the chemical surface exchange coefficients at high pO_2 switches 10% ↔ 20% and 10% ↔ 75%. An Arrhenius plot constructed with the measured coefficients did not give a straight line. Analysis of the control switches with pO_2 10% ↔ 20% after the sample had been kept for different times at 75% pO_2, revealed a significant drop in the chemical surface exchange rate (Figure 4.7).

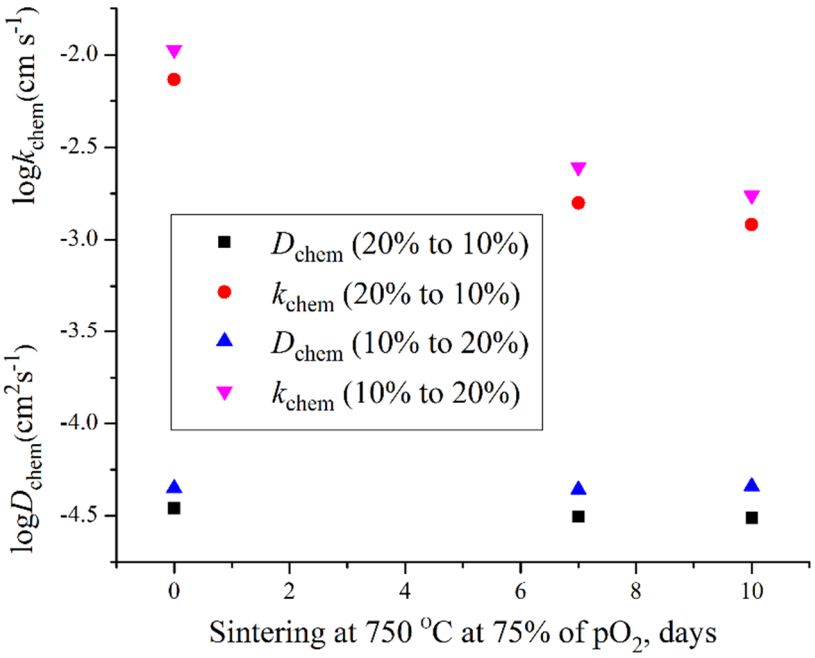

Figure 4.7. Chemical surface exchange degradation in $LaBaCoFeO_{5+\delta}$ at high oxygen partial pressure.

The surfaces of the samples $LnBaCoFeO_{5+\delta}$ (Ln = La and Pr) exposed to high pO_2 switches during electrical conductivity relaxation experiments and of untreated samples were studied using SIMS and XRD (Figures 4.8, 4.9).

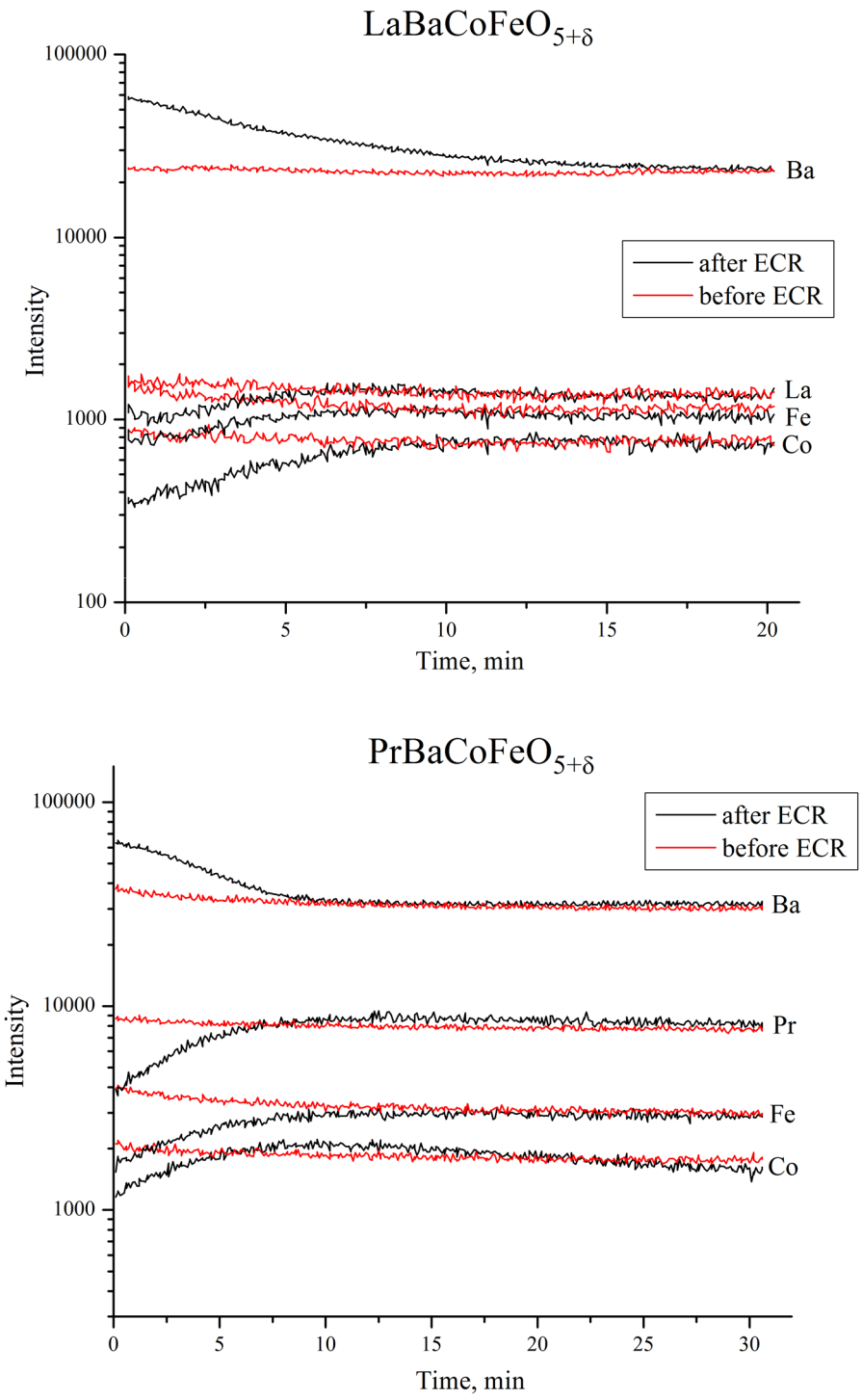

Figure 4.8. SIMS profiles of the surfaces of $LaBaCoFeO_{5+\delta}$ and $PrBaCoFeO_{5+\delta}$ before and after ECR experiments at high pO_2.

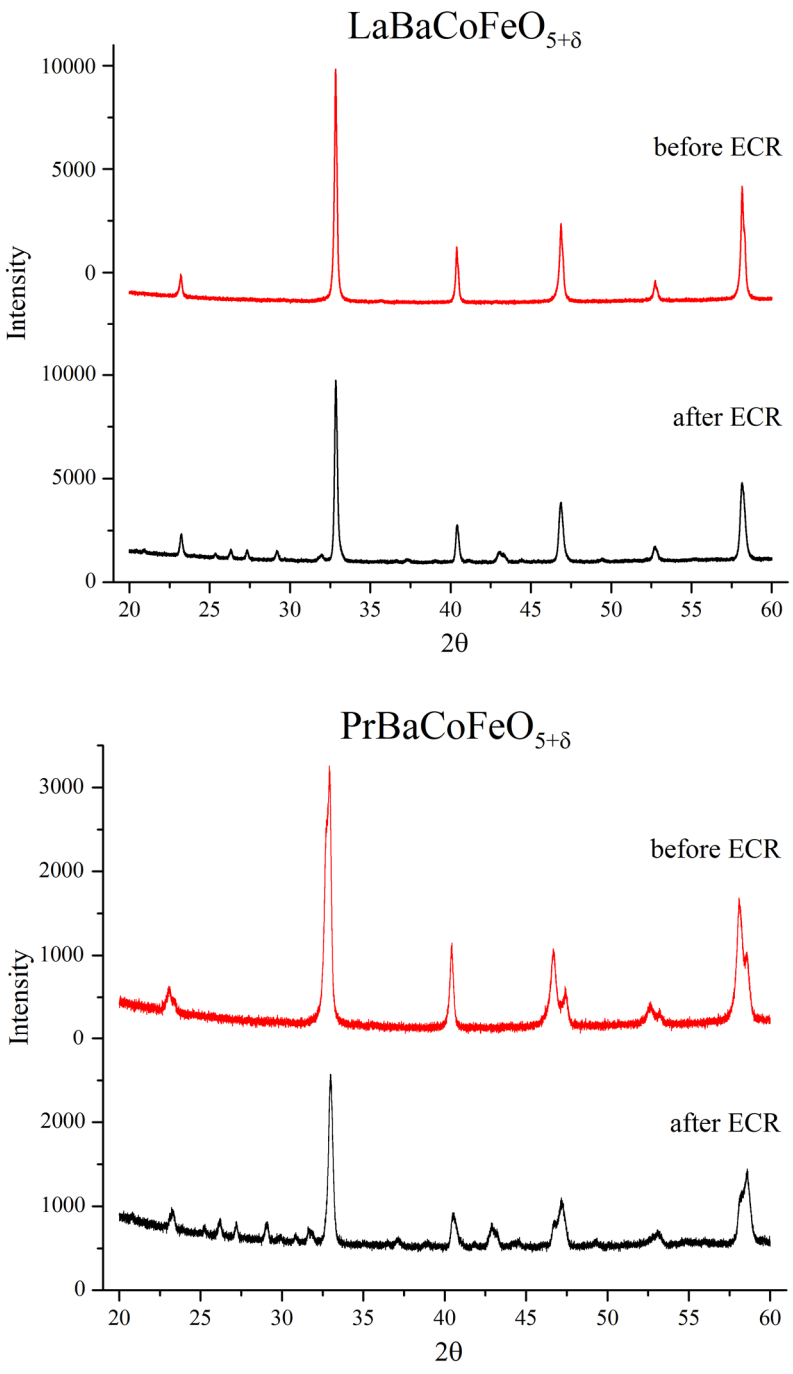

Figure 4.9. Comparison of XRD patterns of the surfaces of $LaBaCoFeO_{5+\delta}$ and $PrBaCoFeO_{5+\delta}$ before and after ECR experiments at high pO_2.

Comparison of the SIMS results revealed excess of Ba atoms and a decrease in concentration of (La, Pr), Fe and Co on the surfaces of the bar samples after ECR experiments. At the same time, XRD measurements indicated the formation of an impurity on the surface of the samples after ECR experiments. While we were not able to determine the composition of the impurity phase, we assume that it is a Ba-rich phase showing little to no oxygen diffusion. The surface phase resulted in a significant decrease of the chemical surface exchange rate during the control ECR switches. Such phase segregation might be a consequence of the close ionic radii of La, Pr and Ba and the conditions of the ECR experiment. Lee *et al.* associated such segregation with a large difference in oxygen vacancy concentration on the surface and in the bulk of the sample [7]. A 10^6 times difference (10^{-3} on surface and 10^{-9} in the bulk), observed for $La_{0.9}Sr_{0.1}MnO_3$ under typical SOFC operating conditions at pO_2 = 1 atm and 1173 K, resulted in formation of narrow space charge layer (~ 1 nm) and in strong Coulombic attraction of dopant cations (Ba, Sr) to segregate on the surface. However, it was shown that lower oxygen partial pressures and smaller rare earth elements in perovskite structures suppress such segregation [7].

ECR experiments at low pO_2 switches (1% ↔ 2%, 2% ↔ 5%) were performed for La and Pr-containing samples in order to reduce the effect of surface segregation and are summarized in Chapter 4.4.2.

4.4.1. ECR measurements: high pO_2 switches

Oxygen diffusion kinetics in Sm and Gd-containing compounds were investigated with ECR in the temperature range 550 – 900 °C by the following switches of the oxygen partial pressure: 2% ↔ 5%, 10% ↔ 20%, 10% ↔ 75%, 20% ↔ 75%.

Values of the chemical oxygen diffusion and chemical surface exchange coefficients for $SmBaCoFeO_{5+\delta}$ were obtained after the fitting of all profiles (Figure 4.10). Activation energies for D_{chem} and k_{chem} are 0.89 ± 0.03 eV and 0.62 ± 0.02 eV, respectively.

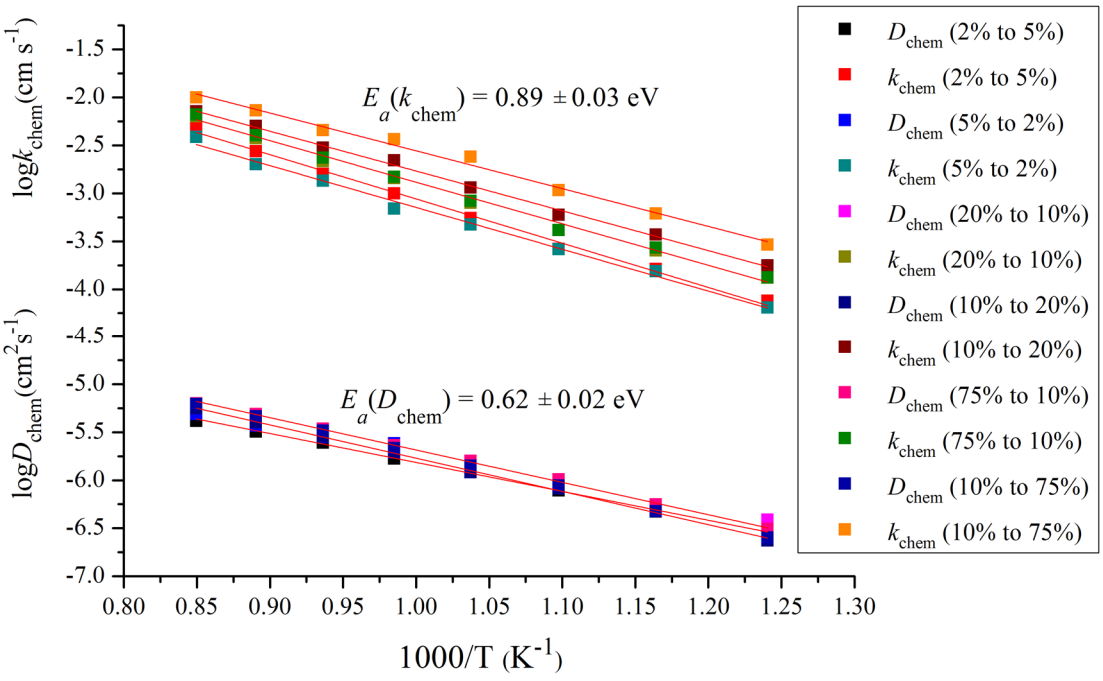

Figure 4.10. Arrhenius plot of the chemical oxygen diffusion and chemical surface exchange coefficients obtained for $SmBaCoFeO_{5+\delta}$ by ECR experiment.

As in the case of $Sr_3YCo_4O_{10.5}$ (Chapter 3c), the values of chemical oxygen diffusion coefficient do not depend on the initial and final oxygen partial pressures and depend only on the temperature. Comparison of the pO_2 switches 20% → 10% and 75% → 10% shows that chemical surface exchange rates also do not depend on the initial oxygen partial pressure, but do depend on the final oxygen partial pressure (Figure 4.11).

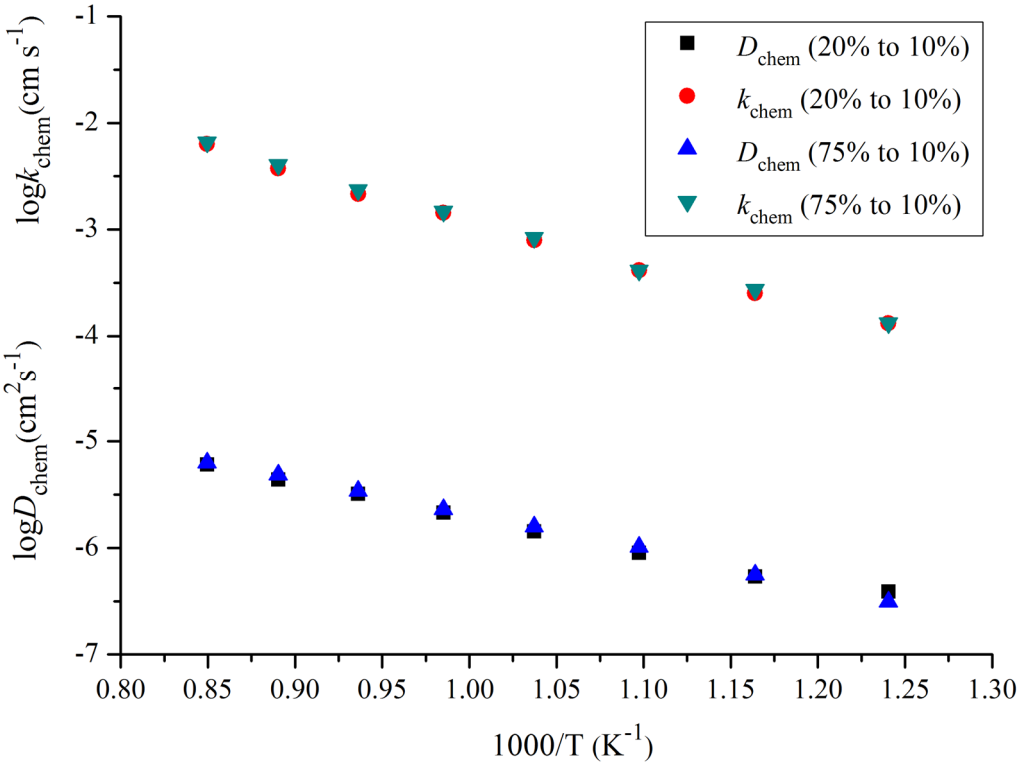

Figure 4.11. Comparison of D_{chem} and k_{chem} for $SmBaCoFeO_{5+\delta}$ calculated from 20% → 10% and 75% → 10% of pO_2 switches.

The dependence of the chemical surface exchange rate on the final oxygen partial pressure at different temperatures is presented in the Figure 4.12 and follows a power law, $k_{chem} \propto [pO_2^{(2)}]^n$, where n was determined from the slopes of $\log(k_{chem})$ vs. $\log(pO_2^{(2)})$ and is in the range 0.29 – 0.44.

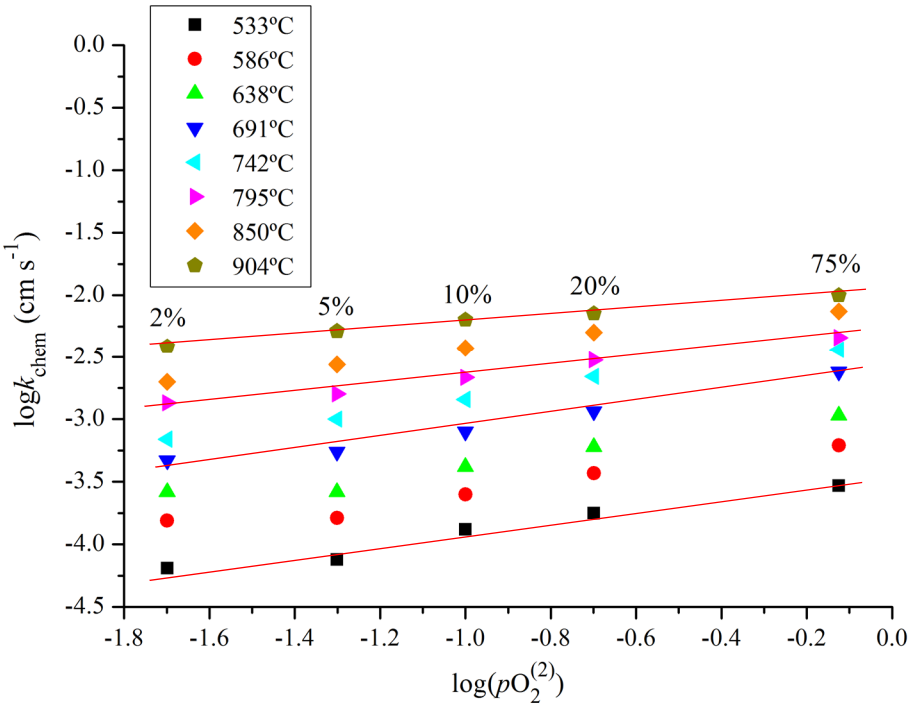

Figure 4.12. Dependence of chemical surface exchange rate for $SmBaCoFeO_{5+\delta}$ on final oxygen partial pressure during ECR switches.

Values of the chemical oxygen diffusion and the chemical surface exchange rate for $GdBaCoFeO_{5+\delta}$ were calculated by fitting of all ECR profiles (Figure 4.13). Activation energies for D_{chem} and k_{chem} are 0.59 ± 0.01 eV and 0.63 ± 0.03 eV, respectively. However, the calculated values of chemical oxygen diffusion showed a small dependence on the

initial and final oxygen partial pressures, which might be associated with a significant deviation from chemical equilibrium during ECR experiments, when the simple linear model for the oxygen kinetics does not work (Chapter 2). To avoid it, additional ECR experiments for $GdBaCoFeO_{5+\delta}$ were performed at low pO_2 switches (1% ↔ 2%, 2% ↔ 5%), and are discussed in 4.4.2.

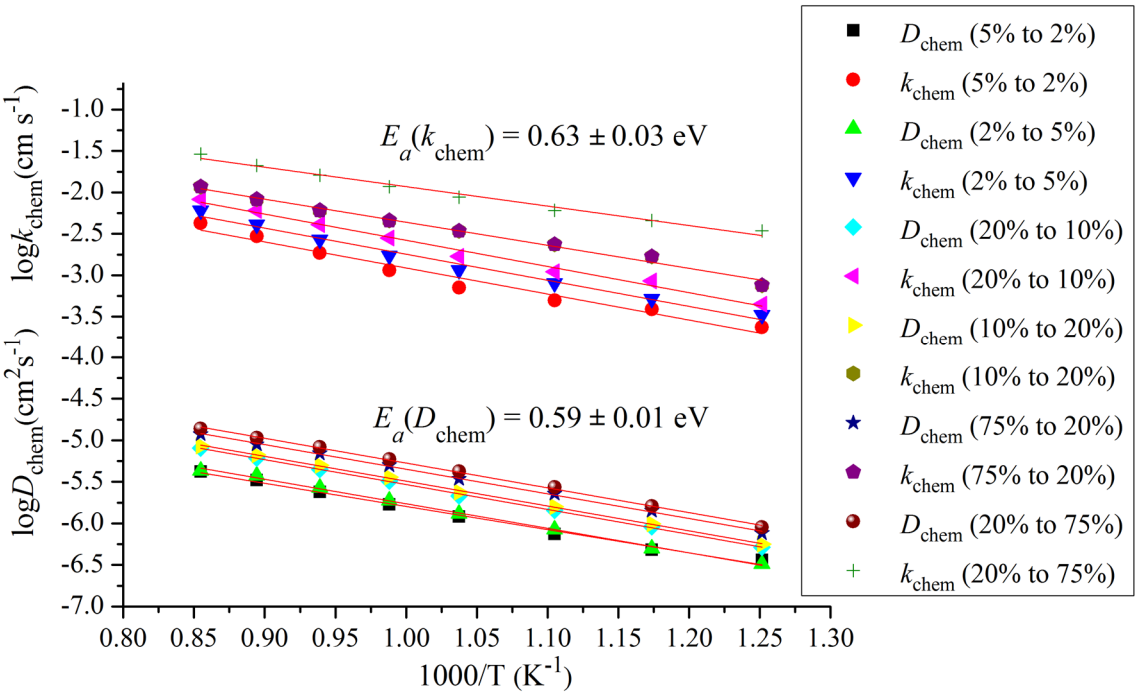

Figure 4.13. Arrhenius plot of the chemical oxygen diffusion and chemical surface exchange coefficients obtained for $GdBaCoFeO_{5+\delta}$ by ECR experiment.

4.4.2. ECR measurements: low pO_2 switches

All electrical conductivity relaxation profiles of $LnBaCoFeO_{5+\delta}$ (Ln = La, Pr and Gd) at low pO_2 switches were fitted to the analytical solution of the mass change (Eq. 2.18). Values of the chemical oxygen diffusion and chemical surface exchange coefficients for La, Pr and Gd-containing compounds are summarized in Figures 4.14, 4.15 and 4.16, respectively. Activation energies for D_{chem} and k_{chem} are 0.77 ± 0.02 eV and 0.48 ± 0.03 eV (La), 0.63 ± 0.01 eV and 0.66 ± 0.05 eV (Pr), 0.60 ± 0.04 eV and 0.68 ± 0.03 eV (Gd), respectively. No dependences of chemical oxygen diffusion coefficients on initial and final oxygen partial pressures were observed.

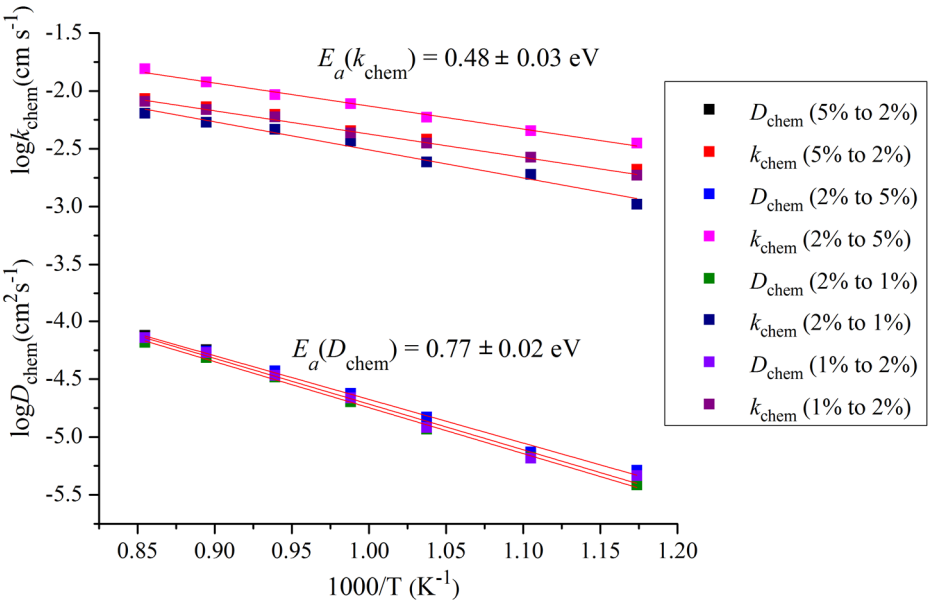

Figure 4.14. Arrhenius plot of the chemical oxygen diffusion and chemical surface exchange coefficients obtained for $LaBaCoFeO_{5+\delta}$ by ECR experiment during low pO_2 switches.

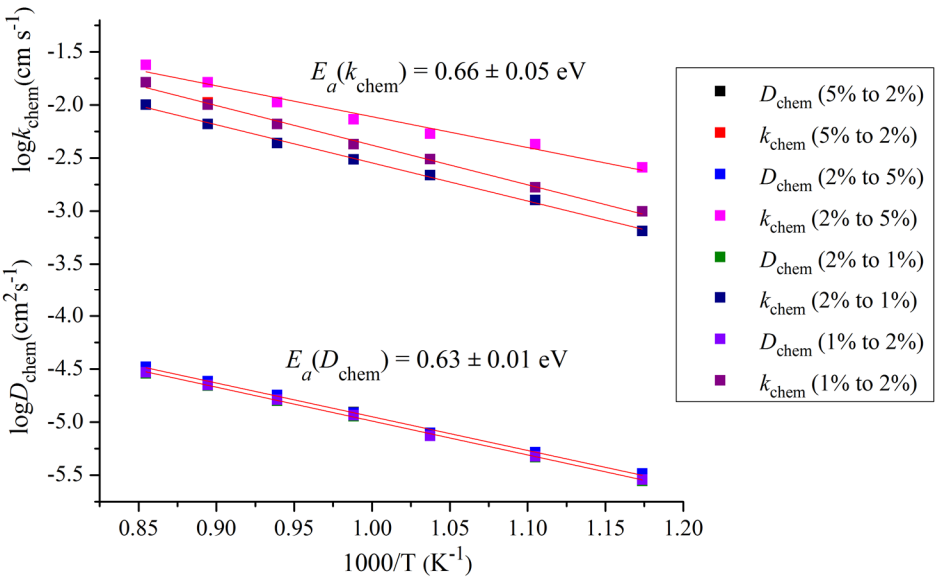

Figure 4.15. Arrhenius plot of the chemical oxygen diffusion and chemical surface exchange coefficients obtained for $PrBaCoFeO_{5+\delta}$ by ECR experiment during low pO_2 switches.

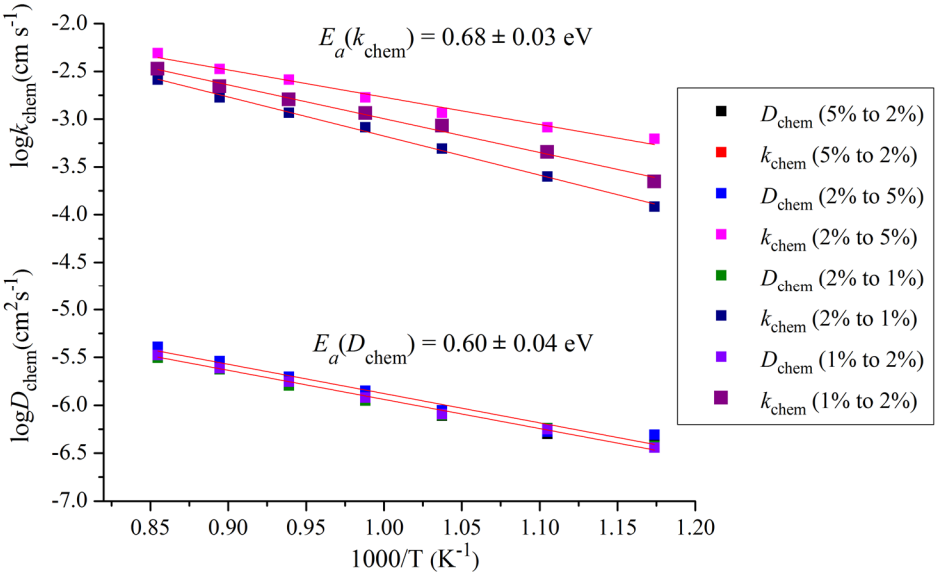

Figure 4.16. Arrhenius plot of the chemical oxygen diffusion and chemical surface exchange coefficients obtained for $GdBaCoFeO_{5+\delta}$ by ECR experiment during low pO_2 switches.

The values of D_{chem} and k_{chem} obtained from ECR experiments for ordered $LaBaCoFeO_{5+\delta}$ during 1% ↔ 2% of pO_2 switches are summarized in Figure 4.17.

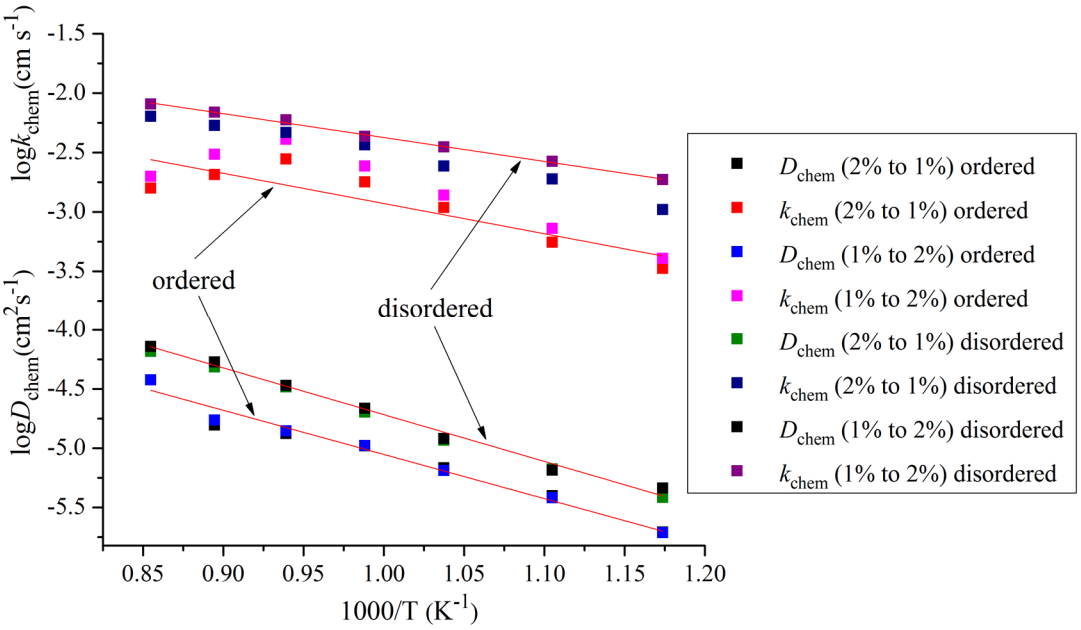

Figure 4.17. Comparison of D_{chem} and k_{chem} for ordered and disordered $LaBaCoFeO_{5+\delta}$ calculated from 1% ↔ 2% of pO_2 switches.

The deviation of chemical surface exchange coefficients from an Arrhenius behavior may be associated with the instability of ordered $LaBaCoFeO_{5+\delta}$ at high temperatures. However, oxygen kinetics in the disordered double perovskite structure were found to be slightly faster than in the ordered structure. That contradicts the recent results for oxygen diffusion in A-cation ordered/disordered $GdBaCoFeO_{5+\delta}$ performed with molecular dynamics simulations [4]. But, as mentioned in Chapter 3, molecular dynamics simulations do not take into account oxygen vacancy formation at elevated temperatures and their effect on oxygen diffusion. Moreover, the oxygen-vacancy concentrations in

ordered and disordered forms may be different at a particular temperature and oxygen partial pressure. Additional study of ordered and disordered $LaBaCoFeO_{5+\delta}$ with isotope exchange depth profiling technique at low oxygen partial pressure is suggested for future work.

4.5. Iodometric titration

Iodometric titration with sodium thiosulfate was used to determine oxygen content in synthesized double perovskites [8, 9].

Each compound were calcined in air at 900 °C overnight to remove adsorbed moisture and carbon dioxide. A small amount of potassium iodide was dissolved in HCl and the synthesized powder was added. Upon complete dissolution (2 – 3 minutes), the solution was titrated with standardized sodium thiosulfate solution under bubbling nitrogen until it became pale yellow in color. Starch solution was added at this point and titration was continued until the solution changed from dark blue to colorless.

Oxygen stoichiometry was calculated with Eq. (4.2).

$$\delta = \frac{CVM_r}{2000m_p - 16CV} - 0.5 \qquad \text{(Equation 4.2)}$$

where m_p is weight of used double perovskite (g), C – concentration of thiosulfate solution (mol/L), V – volume of thiosulfate solution used (ml), M_r – molecular weight of double perovskite, where all B-cations are in oxidation state +2 (g/mol).

For each composition three titrations were performed and average oxygen contents were calculated (Table 4.2).

Table 4.2. Oxygen concentration in $LnBaCoFeO_{5+\delta}$ (Ln = La, Pr, Sm and Gd) synthesized in air determined by iodometric titration.

	$LaBaCoFeO_{5+\delta}$	$PrBaCoFeO_{5+\delta}$	$SmBaCoFeO_{5+\delta}$	$GdBaCoFeO_{5+\delta}$
Oxygen content	5.85 ± 0.01	5.75 ± 0.02	5.54 ± 0.02	5.52 ± 0.03

Moving from the large rare earth element (La) to the smaller ones (Pr, Gd and Sm) leads to increase in the concentration of oxygen vacancies in the structures and, as a result, to decrease of electrical conductivity as summarized in Chapter 4.3.

4.6. Thermogravimetric analysis and thermodynamic factor

The results of ECR experiments represent chemical oxygen diffusion and chemical surface exchange and are different from those obtained during the isotope exchange depth profiling experiments (IEDP). The switch of the oxygen partial pressure is an external driving force, while during the IEDP the oxygen partial pressure is fixed. To obtain oxygen self-diffusion and surface exchange rate coefficients it is necessary to know the thermodynamic factor (Γ_O), which represents the variation of the oxygen concentration in the sample (c_O) with temperature and oxygen partial pressure, pO_2, in the surroundings (Equation 4.3). We used thermogravimetric analysis (TGA) to study this dependence.

$$\Gamma_O = \frac{1}{2} \cdot \frac{\partial \ln(pO_2)}{\partial \ln(c_O)} \qquad \text{(Equation 4.3)}$$

TGA was performed at different oxygen partial pressures in the temperature range 25 – 900 °C. At each pO_2, three TGA experiments were made to be sure that the heating and

cooling profiles were identical. The final measurements were normalized to the initial weight and converted to oxygen content (c_O) vs. temperature (Figure 4.18).

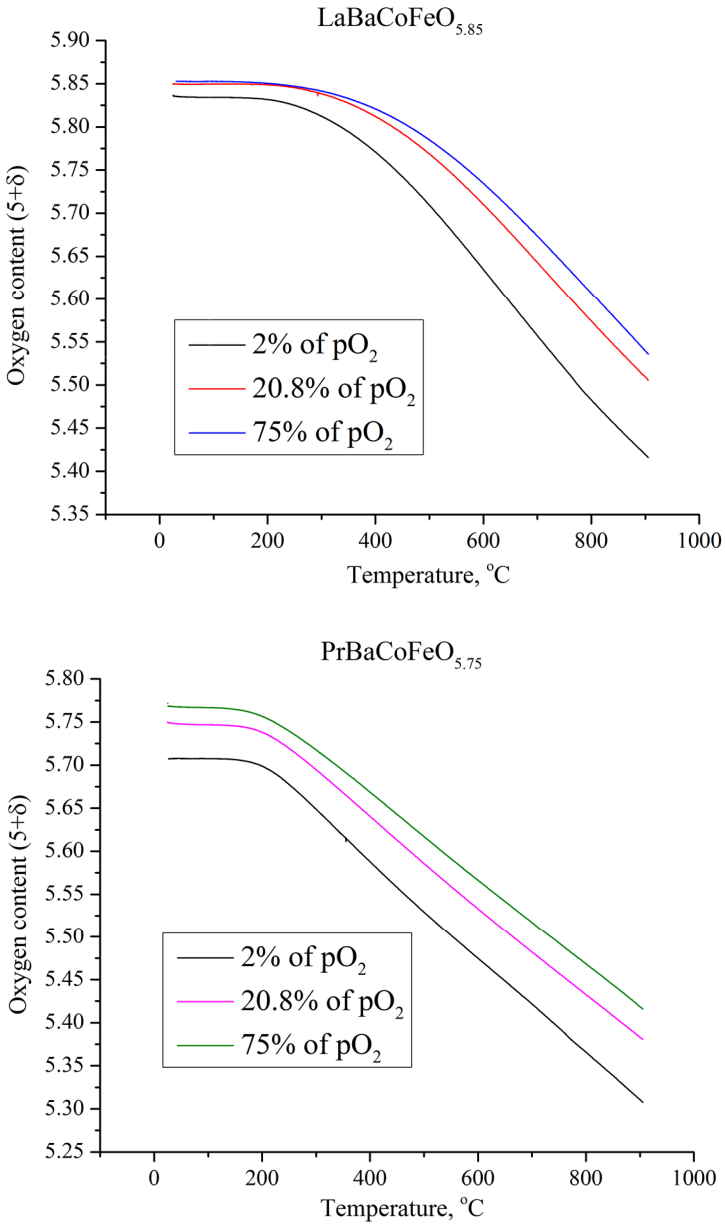

Figure 4.18. Dependences of oxygen concentrations (5+δ) in $LnBaCoFeO_{5+\delta}$ (Ln = La, Pr) synthesized in air on temperature at different pO_2 (continued).

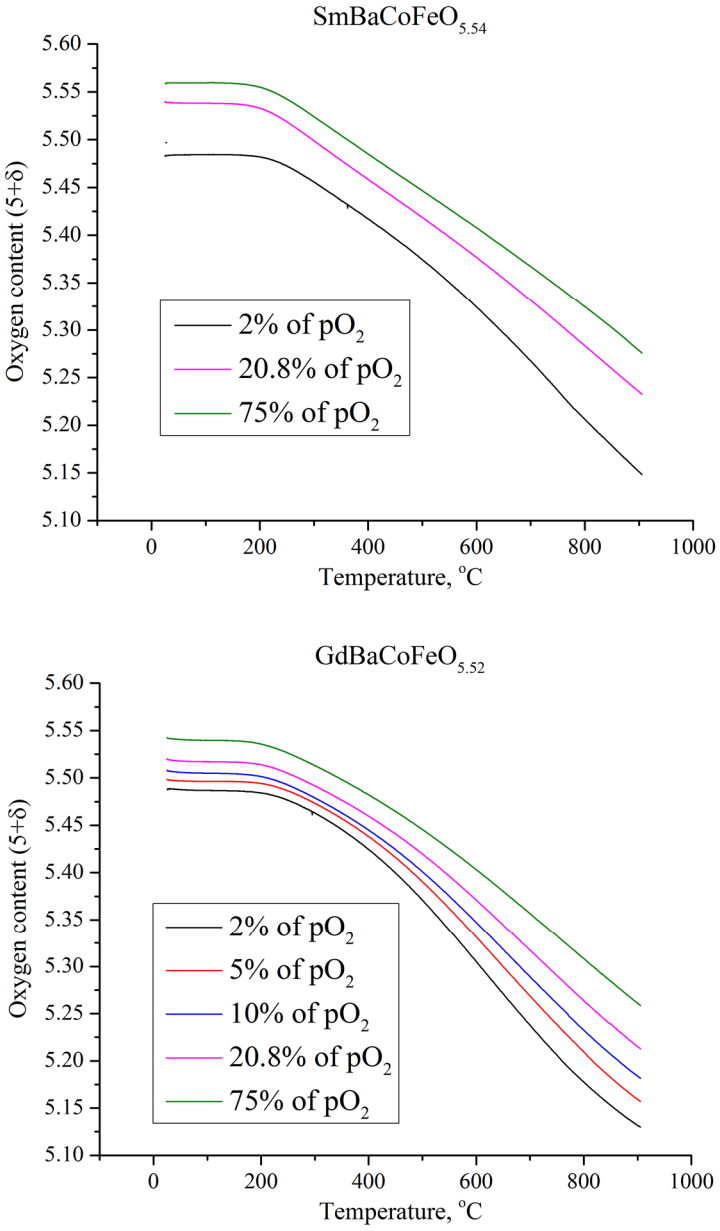

Figure 4.18. (continued) Dependences of oxygen concentrations (5+δ) in $LnBaCoFeO_{5+\delta}$ (Ln = Sm, Gd) synthesized in air on temperature at different pO_2.

The shapes of the profiles are different from those obtained during TGA measurements for $Sr_3YCo_4O_{10.5}$ (Figure 3c.7). In $LnBaCoFeO_{5+\delta}$ release of oxygen atoms occurs preferably from one oxygen position (from the LnO_δ layers). In the case of $Sr_3YCo_4O_{10.5}$, which has the more complicated structure, release of oxygen atoms from different oxygen positions may occur and, as a result, TGA profiles of $Sr_3YCo_4O_{10.5}$ show distinguishable steps.

Oxygen self-diffusion coefficients were calculated in the temperature range 650 – 900 °C using Eq. (4.4):

$$D_O = D_{chem}/\Gamma_O \qquad \text{(Equation 4.4)}$$

where D_O is oxygen self-diffusion coefficient.

Thermodynamic factors in the temperature range 650 – 900 °C for double perovskites $LnBaCoFeO_{5+\delta}$ (Ln = La, Pr, Sm and Gd) are summarized in Table 4.3; the calculated oxygen self-diffusion coefficients are presented in Figure 4.19.

Table 4.3. Thermodynamic factors for $LnBaCoFeO_{5+\delta}$ (Ln = La, Pr, Sm and Gd) determined from TGA profiles.

Temperature, °C	$LaBaCoFeO_{5+\delta}$	$PrBaCoFeO_{5+\delta}$	$SmBaCoFeO_{5+\delta}$	$GdBaCoFeO_{5+\delta}$
528	-	-	131.1(8)	120.6(2)
582	107.1(5)	111.3(9)	120.2(7)	103.4(9)
638	95.8(1)	109.2(5)	108.5(3)	90.3(5)
691	88.4(7)	106.3(4)	98.1(5)	81.7(5)
742	83.7(8)	100.9(6)	88.4(2)	76.0(5)
795	80.6(1)	94.8(4)	80.9(1)	72.8(1)
850	81.1(6)	90.5(5)	76.5(2)	71.8(6)
904	82.7(1)	85.7(2)	74.0(6)	73.0(7)

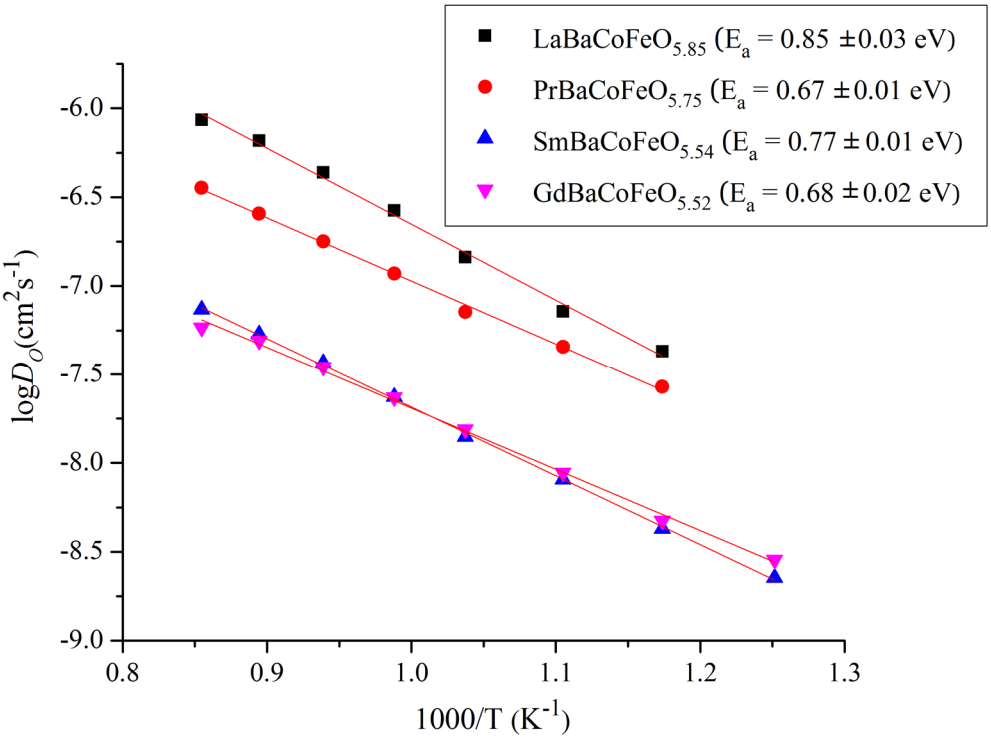

Figure 4.19. Comparison of oxygen self-diffusion coefficients (D_O) for $LnBaCoFeO_{5+\delta}$ (Ln = La, Pr, Sm and Gd), determined by combination of ECR and TGA.

4.7. Conclusions

Oxygen kinetics in double perovskites $LnBaCoFeO_{5+\delta}$ (Ln = La, Pr, Sm and Gd) were studied with the combination of electrical conductivity relaxation technique and thermogravimetric analysis. Both, the electrical conductivity (Figure 4.6) and oxygen self-diffusion coefficients (Figure 4.19), generally speaking, decrease with decrease in the ionic radius of the rare earth element.

The Goldschmidt tolerance factor *t* (Eq. (1.1)), described in Chapter 1, can also be applied to double perovskite structures showing deviation from the ideal cubic symmetry. Due to the decrease in ionic radius from La^{3+} to Gd^{3+}, *t* is predicted to decrease, leading to

lower crystal symmetries and to decrease of O–Co–O bond angles from the ideal 180°. In this case, the overlap between the $Co^{3+/4+}$:3d and O^{2-}:2p orbitals and bandwidth is also decreasing, resulting in decrease of covalency of the Co–O bonds and increase in electron localization (moving from La to Gd), and hence, to decrease in electrical conductivity [10].

While concentration of oxygen vacancies increases from Ln = La to Gd in $LnBaCoFeO_{5+\delta}$, the TGA data show that, upon heating, the formation of oxygen vacancies is larger for the La-containing sample ($\Delta c_O = 0.42$ at $pO_2 = 0.02$), than in Gd-containing sample ($\Delta c_O = 0.35$ at $pO_2 = 0.02$), and is decreasing with decrease of rare earth element size. Additionally, in a study of $Ln_{0.6}Sr_{0.4}CoO_{3-\delta}$ Kharton *et al*. reported that decrease in the size of Ln^{3+} leads to decrease in the size of the anion transfer channel and to increase in the (Ln, Sr)–O bond energy, resulting in decrease of oxygen diffusion [11]. XRD data for $LnBaCoFeO_{5+\delta}$ shows contraction of the unit cell along *c*-axis with decrease of ionic radius of rare earth element that might be a result of reduction of such anion transfer channels.

According to the results, we expect that the electrochemical performance of $LnBaCoFeO_{5+\delta}$ compounds will significantly depend on the size of rare earth element, which controls the possibility of formation of oxygen vacancies at elevated temperatures and the size of anion transfer channels. At the same time, high concentration of oxygen vacancies cannot be considered the only requirement for high values of the oxygen diffusion coefficient.

Comparing chemical oxygen diffusion coefficients in ordered and disordered $LaBaCoFeO_{5+\delta}$ double perovskites, we assume, that lower values of chemical oxygen

diffusion in ordered structures are associated with oxygen migration preferably in the *a-b* plane, $|LnO_{\delta}|$ layers, while in disordered structures the character of oxygen diffusion is isotropic [4].

4.8. References

1. Taskin, A. A.; Lavrov, A. N.; Ando, Y. Achieving fast oxygen diffusion in perovskites by cation ordering. *Appl. Phys. Lett.* **2005**, *86*, 091910/1-091910/3.

2. Chang, A.; Skinner, S. J.; Kilner, J. A. Electrical properties of $GdBaCo_2O_{5+x}$ for ITSOFC applications. *Solid State Ionics* **2006**, *177*, 2009-2011.

3. Kim, G.; Wang, S.; Jacobson, A. J.; Donner, W.; Chen, C. L.; Reimus, L.; Brodersen, P.; Mims, C. A.; Oxygen exchange kinetics of epitaxial $PrBaCo_2O_{5+\delta}$ thin films. *Appl. Phys. Lett.* **2006**, *88*, 024103/1-024103/3.

4. Parfitt, D.; Chroneos, A.; Taranconc, A.; Kilner, J. A. Oxygen ion diffusion in cation ordered/disordered $GdBaCo_2O_{5+d}$. *J. Mater. Chem.* **2011**, *21*, 2183-2186.

5. Pang, S. L.; Jiang, X. N.; Li, X. N.; Wang, Q.; Zhang, Q. Y. Structural stability and high-temperature electrical properties of cation-ordered/disordered perovskite LaBaCoO, *Mater. Chem. and Phys.* **2012**, *131*, 642-646.

6. Burriel, M.; Casas-Cabanas, M.; Zapata, J.; Tan, H.; Verbeeck, J.; Solis, C.; Roqueta, J.; Skinner, S. J.; Kilner, J. A.; Van Tendeloo, G.; Santiso, J. Influence of the Microstructure on the High-Temperature Transport Properties of $GdBaCo_2O_{5.5+\delta}$ Epitaxial Films. *Chem. Mater.* **2010**, *22*, 5512-5520.

7. Lee, W.; Han, J. W.; Chen, Y.; Cai, Z.; Yildiz, B. Cation Size Mismatch and Charge Interactions Drive Dopant Segregation at the Surfaces of Manganite Perovskites. *J. Am. Chem. Soc.* **2013**, *135*, 7909-7925.

8. Karppinen, M.; Matvejeff, M.; Saloma, K; Yamauchib, H. Oxygen content analysis of functional perovskite-derived cobalt oxides. *J. Mater. Chem.* **2002**, *12*, 1761-1764.

9. Jung, J.-I.; Misture, S. T; Edwards, D. D. Oxygen stoichiometry, electrical conductivity, and thermopower measurements of BSCF ($Ba_{0.5}Sr_{0.5}Co_xFe_{1-x}O_{3-\delta}$, $0 \leq x \leq 0.8$) in air. *Solid State Ionics* **2010**, *181*, 1287-1293.

10. Lee, K. T.; Manthiram, A. Comparison of $Ln_{0.6}Sr_{0.4}CoO_{3-\delta}$ (Ln = La, Pr, Nd, Sm, and Gd) as Cathode Materials for Intermediate Temperature Solid Oxide Fuel Cells, *J. Electrochem. Soc.* **2006**, *153*, A794-A798.

11. Kharton, V. V.; Naumovich, E. N.; Vecher, A. A.; Nikolaev, A. V. Oxide Ion Conduction in Solid Solutions $Ln_{1-x}Sr_xCoO_{3-\delta}$ (Ln = La, Pr, Nd). *J. Solid State Chem.* **1995**, *120*, 128-136.

Chapter 5. Thermal expansion studies

As mentioned in Chapter 4, Co-rich compounds demonstrate high thermal expansion coefficients (TEC), restricting their use in high-temperature applications (such as solid oxide fuel cells or oxygen separation systems). Substitution of Co with other transition metals, such as Mn and Fe, is a possible solution of this problem.

To determine thermal expansion coefficients of the double perovskite compounds and $Sr_3YCo_4O_{10.5}$, we conducted high temperature XRD studies (in case of $PrBaCoFeO_{5+\delta}$) and dilatometry experiments.

5.1. Experiment

During high-temperature XRD studies, the powder sample of $PrBaCoFeO_{5+\delta}$ was placed on Pt sample holder in heating stage on the diffractometer. The measurements were performed at 50, 500, 600, 700, 800 and 900 °C in air. Upon achieving each temperature, the sample was kept for 10 minutes before XRD measurements were performed. All XRD patterns were indexed in tetragonal space group *P4/mmm*.

For dilatometry measurements, high-density samples (>95% of theoretical density) of $LnBaCoFeO_{5+\delta}$ (Ln = La, Pr, Sm and Gd) and $Sr_3YCo_4O_{10.5}$ were used.

Measurements were performed using a horizontal pushrod dilatometer Netzsch DIL 402C in the temperature range 25 – 900 °C in static air with the heating rate of 1 °C/min.

5.2. Results and discussion

High-temperature XRD studies of $PrBaCoFeO_{5+\delta}$ are summarized in Table 5.1 and Figure 5.1 ($\Delta L/L_0$ vs. temperature plot). $\Delta L/L_0$ represents relative elongation of the sample upon heating.

According to Figure 5.1, two linear regions of thermal expansion can be isolated: 50 – 500 °C (α = 8.31(1) ppm/K) and 500 – 900 °C (α = 20.54(8) ppm/K). Relatively high values of thermal expansion coefficients in high temperature region are mainly related to the formation of oxygen vacancies upon heating (chemical expansion). As was shown by TGA studies of compounds synthesized at different oxygen partial pressures (Chapters 3 and 4), the concentration of oxygen vacancies significantly increases as the temperature increases. At the same time, formation of oxygen vacancies is associated with reduction of Co^{4+} ions to Co^{3+}, leading to increase of ionic radius of cobalt ions [1-3]. Moreover, transition of Co^{3+} from low spin state ($t_{2g}^6 e_g^0, r = 0.545$ Å) to high spin ($t_{2g}^4 e_g^2, r = 0.61$ Å) is also results in higher TEC values [3, 4]. Similar behaviors were observed for other Co-containing compounds [5, 6].

A comparison of the unit cell parameters *a* and *c* clearly indicates the anisotropic character of the thermal expansion. This is probably associated with the cation ordering in A-sublattice of double perovskites and, as a result, with formation of oxygen vacancies upon heating preferably in $|LnO_\delta|$ layers.

Results of dilatometry measurements are presented on $\Delta L/L_0$ vs. temperature plots (Figure 5.2).

Table 5.1. Dependences of the unit cell parameters and volume of $PrBaCoFeO_{5+\delta}$ on temperature and the corresponding thermal expansion coefficients, determined by high temperature XRD.

Temperature, °C	*a*, Å	*c*, Å	V, Å^3	$\sqrt[3]{V}$, Å
50	3.9593(5)	7.6895(1)	120.5440(8)	4.9398(6)
500	3.9596(5)	7.7750(1)	121.9028(8)	4.9583(5)
600	3.9696(5)	7.7871(1)	122.7100(6)	4.9692(7)
700	3.9790(6)	7.7991(1)	123.4825(1)	4.9796(8)
800	3.9871(7)	7.8131(1)	124.2089(4)	4.9894(3)
900	3.9951(9)	7.8267(2)	124.9262(1)	4.9990(1)
TEC, α (ppm/K)	10.6494(1)	20.9911(9)		14.0867(1)

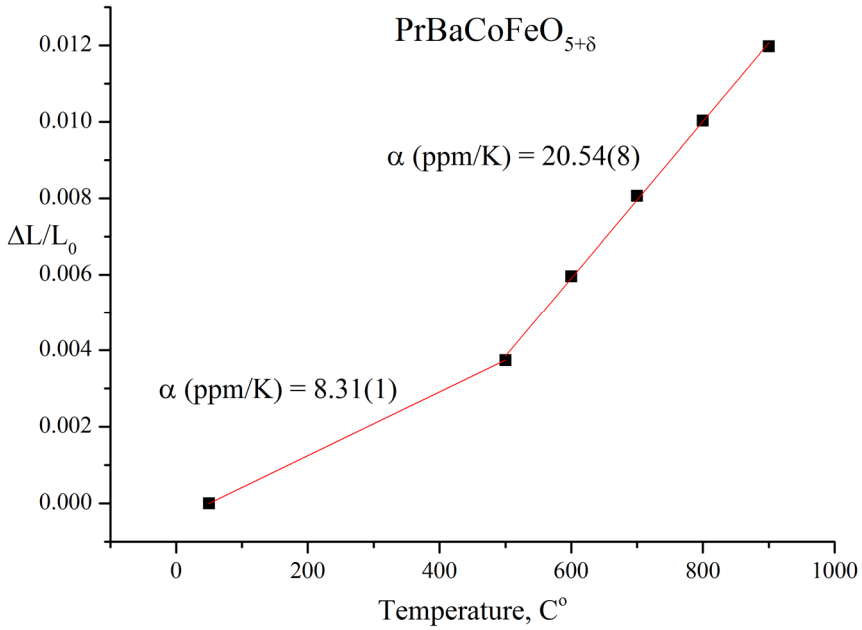

Figure 5.1. Thermal expansion ($\Delta L/L_0$) behavior of $PrBaCoFeO_{5+\delta}$ in temperature range 50 – 900 °C in air, calculated from cubic root of unit cell volume.

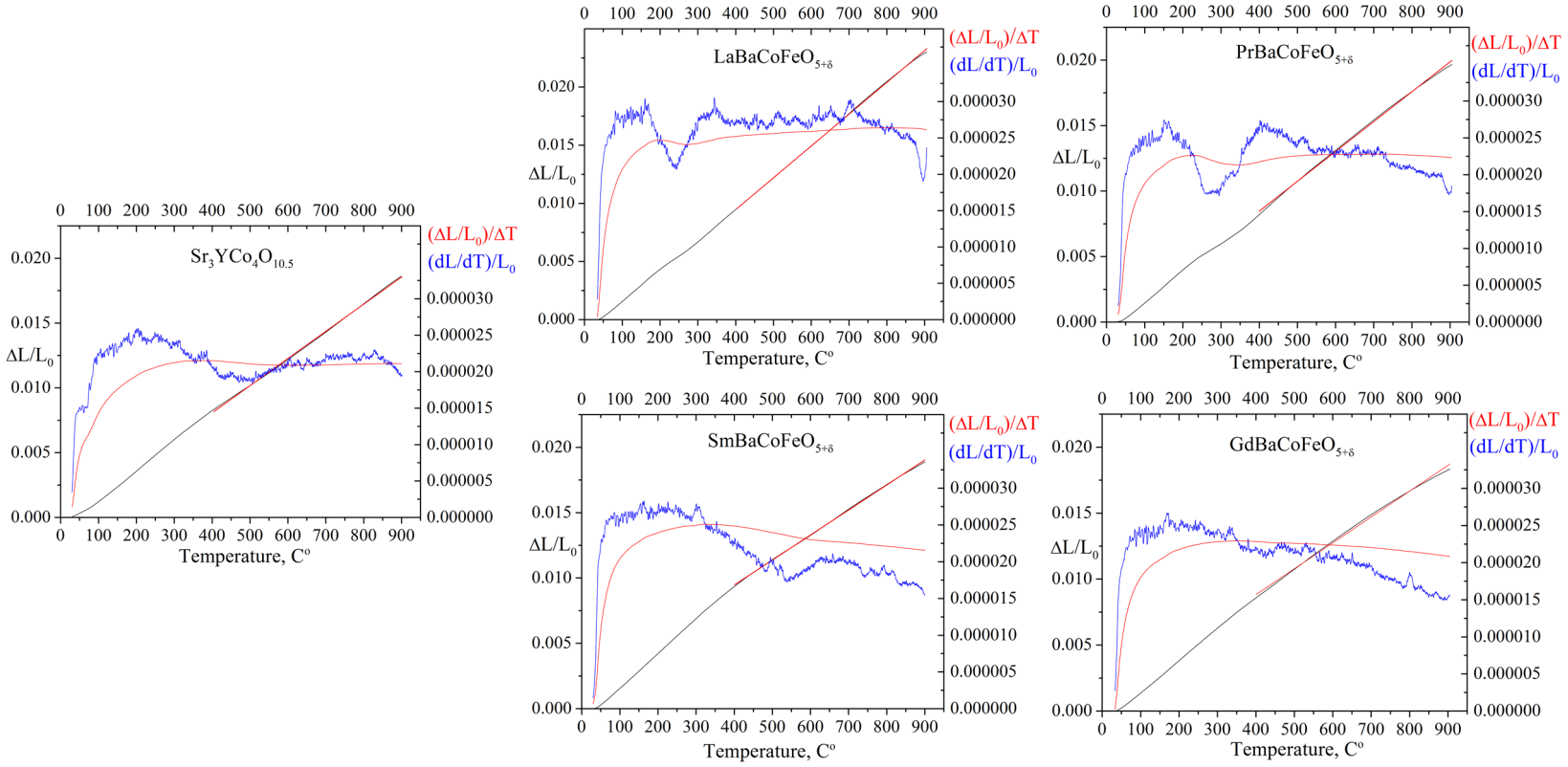

Figure 5.2. Thermal expansion behaviors for $Sr_3YCo_4O_{10.5}$ and $LnBaCoFeO_{5+\delta}$ (Ln = La, Pr, Sm and Gd) in the temperature range of 25 – 900 °C in air obtained by dilatometry experiments.

The thermal expansion in the low-temperature region (25 – 400 °C) shows anomalous behavior most likely due to the dimensions of the samples used for dilatometry experiments. The thickness of each sample along the thermal expansion measurement direction was about 2 mm. For such small dimensions, instrumental errors of the dilatometer are significant. Attempts to prepare larger samples were not successful due to the cracking during sintering. However, comparison of results of high-temperature XRD and results of dilatometry measurements for $PrBaCoFeO_{5+\delta}$ revealed similar values of the thermal expansion coefficients in high temperature region (20.54(8) ppm/K by HT XRD and 22.79(4) ppm/K by dilatometry). Thermal expansion coefficients of $Sr_3YCo_4O_{10.5}$ and $LaBaCoFeO_{5+\delta}$ (Ln = La, Pr, Sm and Gd) in the approximately linear region 400 – 900 °C are summarized in Table 5.2.

Table 5.2. Thermal expansion coefficients in $Sr_3YCo_4O_{10.5}$ and $LnBaCoFeO_{5+\delta}$ (Ln = La, Pr, Sm and Gd) synthesized in air.

Sample	TEC (ppm/K) in 400 – 900 °C region
$Sr_3YCo_4O_{10.5}$	20.94 ± 0.02
$LaBaCoFeO_{5+\delta}$	27.35 ± 0.02
$PrBaCoFeO_{5+\delta}$	22.79 ± 0.04
$SmBaCoFeO_{5+\delta}$	19.14 ± 0.02
$GdBaCoFeO_{5+\delta}$	19.09 ± 0.05

In the double perovskites $LnBaCoFeO_{5+\delta}$ (Ln = La, Pr, Sm and Gd) the thermal expansion coefficient decreases from La to Gd-containing samples. Lee *et al*. explained such behavior by considering the ionic character of Ln–O bonds in $Ln_{0.6}Sr_{0.4}CoO_{3-\delta}$ [3]. The ionic character of the bond between atoms A and B depends on the difference of their electronegativities and follows the Eq. (5.1) [7].

$$\%\ \text{ionic character} = (1 - \exp[-0.25(x_A - x_A)^2]) \times 100$$

(Equation 5.1)

where x_n is electronegativity of atom n.

So, taking into account Pauling electronegativity values [8], the percent of ionic character in Ln–O bonds is decreasing from La to Gd, leading to formation of more covalent bonds, which, in general, have lower thermal expansion.

The double perovskites with smaller rare earth elements, such as Sm and Gd, have smaller TECs and are therefore more suitable for application as cathodes in solid oxide fuel cells. However, additional substitutions of Co with Fe or Mn might be necessary to lower TEC.

Due to the small number of results of dilatometry measurements in presented work, additional studies of thermal expansion of $Sr_3YCo_4O_{10.5}$ and $LaBaCoFeO_{5+\delta}$ by combination of high-temperature XRD and dilatometry studies of larger samples (thickness of ~10 mm) are suggested for future work.

5.3. References

1. Petrov, A. N.; Kononchuk, O. F.; Andreev, A. V.; Cherepanov, V. A.; Kofstad, P. Crystal structure, electrical and magnetic properties of $La_{1-x}Sr_xCoO_{3-y}$. *Solid State Ionics* **1995**, *80*, 189-199.

2. Mori, M.; Sammes, N. M. Sintering and thermal expansion characterization of Al-doped and Co-doped lanthanum strontium chromites synthesized by the Pechini method. *Solid State Ionics* **2002**, *146*, 301-312.

3. Lee, K. T.; Manthiram, A. Comparison of $Ln_{0.6}Sr_{0.4}CoO_{3-\delta}$ (Ln = La, Pr, Nd, Sm, and Gd) as cathode materials for intermediate temperature solid oxide fuel cells. *J. Electrochem. Soc.* **2006**, *153*, A794-A798.

4. Huang, K.; Lee, H. Y.; Goodenough J. B. Sr- and Ni-Doped $LaCoO_3$ and $LaFeO_3$ perovskites new cathode materials for solid-oxide fuel cells. *J. Electrochem. Soc.* **1998**, *145*, 3220-3227.

5. Zhao, L.; Shen, J.; He, B.; Chen, F.; Xia, C. Synthesis, characterization and evaluation of $PrBaCo_{2-x}Fe_xO_{5+d}$ as cathodes for intermediate-temperature solid oxide fuel cells. *Int. J. Hydrogen Energy* **2011**, *36*, 3658-3665.

6. Kim, Y. N.; Kim, J.-H.; Manthiram, A. Effect of Fe substitution on the structure and properties of $LnBaCo_{2-x}Fe_xO_{5+d}$ (Ln =Nd and Gd) cathodes. *Journal of Power Sources* **2010**, *195*, 6411-6419.

7. Callister, W. D., Jr. *Materials Science and Engineering an Introduction*, 5th ed.; John Wiley & Sons: New York, 2000; p 23.

8. Barsoum, M. *Fundamentals of Ceramics*. McGraw-Hill: New York, 1997; p 26.

Chapter 6. Summary and future work

6.1. Summary

The study of oxygen diffusion kinetics in mixed ionic andelectronic conducting compounds (MIECs) remains one of the most important aspects of the development of new cathode materials for solid oxide fuel cells (SOFCs). Requirement of high values of ionic and electronic conductivities makes MIEC oxides with perovskite (ABO_3) and perovskite-related structures favorable systems for study. Cobalt-based systems, in general, show very fast oxygen kinetics, but the presence of Co may lead to low chemical and mechanical (thermal expansion) stabilities of the cathodes. Several possible ways to improve the stability of Co-based cathodes are known: 1) macrostructure improvement of the cathode to compensate the large thermal expansion; or 2) partial substitution of Co with other transition metals, such as Fe and Mn. Regardless of the technique used to improve performance, values of ionic and electronic conductivities should remain high and should be known reliably.

The aim of this work was to combine a theoretical basis and different experimental techniques for better understanding of oxygen kinetics in perovskite-related compounds, which is usually considered as a two-step process: the surface exchange reaction and oxygen diffusion in the bulk of the material.

In the first chapter of the thesis, the general background for oxygen transport in mixed ionic and electronic conducting compounds was described using the example of a binary system together with the defect chemistry and the application of MIEC oxides.

Mathematical equations for different driving forces (such as electric field or chemical gradient) were also introduced.

In Chapter 2, three different techniques for the study of oxygen kinetics were discussed: electrical conductivity relaxation (ECR), isotope exchange depth profiling (IEDP) and molecular dynamic simulations (MD). While ECR and IEDP methods are based on the same mathematical descriptions of oxygen transport, the experiments themselves are different. In ECR experiments, the switch of oxygen partial pressure in the surroundings of the MIEC sample leads to change of its electrical conductivity, which can be measured and associated with the chemical oxygen diffusion and chemical surface exchange coefficients. In the IEDP approach, an oxygen-conducting sample in chemical equilibrium with oxygen in the surroundings is exposed to ^{18}O atmosphere at the same partial pressure, leading to adsorption of ^{18}O and release of ^{16}O. The depth of ^{18}O penetration into the sample, measured with secondary ion mass spectroscopy (SIMS), is associated with oxygen tracer diffusion coefficient, tracer surface exchange rate and exposure time. To compare results of ECR and IEDP methods the thermodynamic factor was introduced. Molecular dynamics simulations are not based on mathematical model of oxygen transport, but on the description of ionic crystal lattice energy. During the simulations values of oxygen self-diffusion coefficient can be obtained from direct observation of ion trajectories.

All three techniques were applied to study oxygen transport in perovskite-related compound $Sr_3YCo_4O_{10.5}$. Molecular dynamics simulations, summarized in Chapter 3A, revealed possible oxygen migration pathways: Co-O1/O2 octahedra (*a*-*b*-plane migration)

and along the O2-O1-O2 pathway (*c*-axis migration). The values of oxygen self-diffusion coefficient were calculated from the slopes of mean square displacement of oxygen ions from their initial positions. The values of oxygen tracer diffusion and tracer surface exchange rate coefficients were determined with IEDP/SIMS technique and described in Chapter 3B. Electrochemical performance of symmetrical cells with $Ce_{0.9}Gd_{0.1}O_{1.95}$ (GDC) as electrolyte ($Sr_3YCo_4O_{10.5}$ / $Ce_{0.9}Gd_{0.1}O_{1.95}$ / $Sr_3YCo_4O_{10.5}$) in the temperature range 620 – 770 °C has been evaluated using AC Impedance. In Chapter 3C, oxygen transport in $Sr_3YCo_4O_{10.5}$ was studied with the ECR approach; chemical oxygen diffusion coefficients and chemical surface exchange rates were calculated. Thermogravimetric analysis and iodometric titration were used to determine thermodynamic factors, which represent the oxygen concentration in the sample as a function of temperature and oxygen partial pressure in the surroundings. Finally, we showed that results obtained by all three techniques are in excellent agreement and the activation energy for oxygen self-diffusion is about 1.6 eV. When reproducibility of the results obtained by different methods was confirmed, the choice of one or another technique to study oxygen transport study depends only on the availability.

Electrical conductivity relaxation along with TGA and iodometric titration were used to study oxygen transport in double perovskites $LnBaCoFeO_{5+\delta}$ (Ln = La, Pr, Sm and Gd), and the results are summarized in Chapter 4. Comparison of the results revealed a strong dependence of the electrochemical properties on the rare earth element (REE) in the structure. Decrease of the ionic radius of REE leads to a drop of both electrical and ionic conductivities, despite the increasing concentration of oxygen vacancies, which are usually

considered as a major criterion for fast ionic conductivity. The size of REE determines anion transfer channel dimensions and Ln–O bond energy [1].

Comparison of chemical oxygen diffusion coefficients and chemical surface exchange rates in ordered and disordered $LaBaCoFeO_{5+\delta}$ showed faster oxygen transport in disordered structure. The results are not consistent with the results of molecular dynamics simulations for ordered/disordered $GdBaCoFeO_{5+\delta}$ [2], which may due to the fact that MD simulations do not take into account formation of oxygen vacancies as the temperature increases. According to our XRD data (Figure 4.3), where we showed that amount of oxygen vacancies in the structure directly effects unit cell dimensions, we assume that this effect is much wider and spreads on to dimensions of anion transfer channels. Slower oxygen diffusion in the ordered structure can be associated with the fact that cation ordering in a varying degree effects the ordering in anion sublattice, decreasing the mobility of oxygen ions.

Dilatometry measurements (Chapter 5) revealed a strong dependence of thermal expansion coefficient on the rare earth element in $LnBaCoFeO_{5+\delta}$. Despite the better conducting properties of $LaBaCoFeO_{5+\delta}$, double perovskites with smaller REE (Sm, Gd) seem more preferable in application as cathode materials in solid oxide fuel cells (SOFCs).

6.2. Future work

Further investigation of Co-containing double perovskites with substitution of Co with other transition metals, such as Fe and Mn, needs to be made due to their excellent potential in SOFC application as shown in this thesis.

Dependence of oxygen kinetic on cation ordering in A-sublattice in $LaBaCoFeO_{5+\delta}$ was shown in this work. Additional studies should be made with isotope exchange depth profiling technique at different oxygen partial pressures along with high temperature x-ray or neutron powder diffraction to determine the influence of the concentration of oxygen vacancies and their location on oxygen diffusion.

While preliminary results of mechanical properties (thermal expansion) of double perovskites were presented in this work, further investigation with combination of high temperature XRD and dilatometry are necessary to determinate the most suitable material in terms of SOFC applications.

For $SmBaCoFeO_{5+\delta}$ and $GdBaCoFeO_{5+\delta}$ compounds, suitable electrolyte materials need to be determined in terms of chemical and mechanical compatibility. Electrochemical performance of these double perovskites needs to be studied with electrochemical impedance spectroscopy (EIS).

6.3. References

1. Kharton, V. V.; Naumovich, E. N.; Vecher, A. A.; Nikolaev, A. V. Oxide ion conduction in solid solutions $Ln_{1-x}Sr_xCoO_{3-\delta}$ (Ln = La, Pr, Nd). *J. Solid State Chem.* **1995**, *120*, 128-136.

2. Parfitt, D.; Chroneos, A.; Taranconc, A.; Kilner, J. A. Oxygen ion diffusion in cation ordered/disordered $GdBaCo_2O_{5+d}$. *J. Mater. Chem.* **2011**, *21*, 2183-2186.